DESIGN AND TESTING OF LOW DIVERGENCE ELLIPTICAL-JET NOZZLES FOR USE IN CREEP-FEED GRINDING

by

Ovey Etienne Rouly

Submitted in partial fulfilment of the requirements
for the degree of Master of Applied Science

at

Dalhousie University
Halifax, Nova Scotia
December 2013

Lillian and Chris; without you, I would not have been possible. This is for you.

Table of Contents

List of Tables vii

List of Figures viii

Abstract xiv

List of Abbreviations and Symbols Used xv

Acknowledgements xvi

CHAPTER 1 INTRODUCTION 1

1.1 Background 1

1.1.1 Research Topic Overview 1

1.1.2 Thesis Outline 3

1.2 Grinding Theory 5

1.2.1 Wheels 6

1.2.2 Cutting Mechanics 7

1.2.3 Types of Grinding 9

1.2.4 Wheel Wear and Dressing 10

1.2.5 Possible Workpiece Damage 13

1.2.6 Cutting Fluid 14

1.3 Summary 15

CHAPTER 2 CUTTING FLUID THEORY 16

2.1 Types of Cutting Fluid 16

2.1.1 Solid and Paste Lubricants 16

2.1.2 Gas and Mist Lubricants 17

2.1.3 Liquid-Based Cutting Fluids 18

2.2 Issues in Application 18
2.2.1 Useful Flow 18
2.2.2 Boiling Limit 20
2.2.3 Air Boundary Layer 21
2.2.4 Wheel Cleaning 23
2.2.5 Profile Grinding 23
2.3 Unconventional Application Methods 24
2.3.1 Shoe Nozzle 24
2.3.2 Floating Nozzle 25
2.3.3 Radial Jets 26
2.3.4 Dual Fluid 26
2.4 Conventional Application Methods 27
2.4.1 Flood Jet 27
2.4.2 Coherent Jet 29
2.4.3 High-Pressure Jet 31
2.5 Coherent Jet Nozzle Design 33
2.5.1 Nozzle Design Parameters 33
2.5.2 Visualization of Flow within the Nozzle 34
2.5.3 Fluid Flow 37
2.5.4 Jet Placement 38
2.6 Summary 39
CHAPTER 3 NOZZLE STUDIES 40
3.1 Nozzle Fabrication 40
3.1.1 Rapid-Prototyping Feasibility 41
3.2 Internal Contour Overview 43

3.3 Generation of Internal Contours 45
3.3.1 Validation of Bezier Curve Use 45
3.3.2 Defining Characteristics of a Bezier Curve 46
3.3.3 Constraints on Design Parameters 49
3.3.4 Curve Generation 52
3.3.5 Extrapolation to Three-Dimensional Solid 54
3.4 Jet Behavior Testing Process 56
3.4.1 Experimental Setup 56
3.4.2 Experimental Procedure 58
3.5 Summary of Jet Characteristics 59
3.5.1 Jet Divergence Angle 60
3.5.1.1 Exit Angle Investigation 60
3.5.1.2 Arc Length Investigation 62
3.5.1.3 Aperture Aspect Ratio Investigation 64
3.5.2 Lowest Divergence of an Elliptical Jet 66
3.5.3 Fluid Distribution 68
3.6 Summary 70
CHAPTER 4 Preliminary Experiments and Testing Procedure 72
4.1 Experimental Apparatus 72
4.1.1 Grinding and Data Acquisition Equipment 72
4.1.2 Grinding and Dressing Parameters 74
4.2 Cutting Fluid Apparatus Preliminary Testing 75
4.2.1 Selection of Nozzle Dimensions 75
4.2.2 Generation of Specific Nozzles 78
4.2.3 Positioning of Nozzle for Grinding 84

4.3 Experimental Procedure 87
4.4 Experimental Preparation Summary 89
CHAPTER 5 EXPERIMENTAL RESULTS AND DISCUSSION 90
5.1 Surface Finish 90
5.1.1 Introduction to Surface Finish Measurements 90
5.1.2 Surface Finish Results 94
5.2 Power Output 102
5.2.1 Power Output Data Manipulation 102
5.2.2 Power Output Results 104
5.3 Grinding Forces 113
5.4 Summary 119
CHAPTER 6 CONCLUSION 121
6.1 Research Summary 121
6.2 Conclusions and Future Research 122
APPENDIX 124
REFERENCES 129

List of Tables

Table 1 – Grinding and Data Acquisition Equipment 74

Table 2 – Dressing and Grinding Parameters 75

Table 3 – Nozzle Design Parameters 78

Table 4 – Vertical Offset Grinding Parameters 85

Table 5 – Surface Measurement Equipment 88

Table 6 – Surface Finish Summary Table 127

Table 7 – Power Summary Table 128

List of Figures

Figure 1.1: Two typical coolant delivery nozzles used in industry: (a) circular and (b) rectangular [Webster *et al.* 1995]....2

Figure 1.2: (b) A typical profiled workpiece, (b) tool wear on a profiled wheel, and (c) workpiece damage. 2

Figure 1.3: Potential fluid coverage across a profiled workpiece using (a) a circular jet, (b) multiple jets, and (c) an elliptical jet. 3

Figure 1.4: Outlined flow of manuscript. 5

Figure 1.5: Detail of grinding wheel cross-section showing various structural components. 6

Figure 1.6: Schematic of idealized cutting model. 7

Figure 1.7: Overview of a grinding setup showing (a) geometric parameters and (b) measurable forces. 7

Figure 1.8: Typical geometry of the cutting process in grinding. 8

Figure 1.9: Schematic views of cutting, plowing, and rubbing phenomena in grinding. 8

Figure 1.10: Detailed view of grain fracture, bond fracture, and wear flats. 10

Figure 1.11: (a) Extreme example of grain and bond fracture on a flat-profiled wheel [Steffen 2004] and (b) typical wheel loading on a profiled wheel. 11

Figure 1.12: Power of the spindle as a result of (a) grain and bond fracture, (b) attritious wear, and (c) wheel loading. Grinding parameters listed in legend. 12

Figure 1.13: (a) Typical rotary dressing setup and (b) single-point dressing setup. 13

Figure 1.14: Observed power spike associated with film boiling of the cutting fluid [Skerlos 1998]. 14

Figure 2.1: Hydrodynamic pressures measured on a workpiece during creep-feed cycle [Webster and Cui 1995]. 21

Figure 2.2: Air boundary layer entrained around a rotating disc. 22

Figure 2.3: Flood nozzle developed with primary jet and secondary air-scraping jet [Banerjee *et al.* 2007]. 23

Figure 2.4: Arbitrary grinding profile cross-section illustrating regions at high-risk for damage. 24

Figure 2.5: Typical shoe nozzle. 25

Figure 2.6: Simplified schematic of a typical floating nozzle. 25

Figure 2.7: Cross-section of grinding wheel showing internal radial coolant jets [Irani *et al.* 2005]. 26

Figure 2.8: Apparatus for the separate application of lubricant and coolant [Irani 2006]. 27

Figure 2.9: Two variations of a traditional rectangular flood-type nozzle [Cui and Webster 1994]. 28

Figure 2.10: Suggested design parameters of coherent circular nozzle, including inlet and exit diameters (D, d). 29

Figure 2.11: Jet velocity profiles for (a) a coherent nozzle and (b) a flood-type nozzle. [Morgan and Baines-Jones 2009] 31

Figure 2.12: Workpiece form error with flood, coherent and high-pressure coolant jets [Hartlen *et al.* 2008]. 32

Figure 2.13: CFD analysis performed within various nozzles [Shen *et al.* 2011]. 36

Figure 2.14: CFD analysis of (a) a typical and (b) improved Webster nozzle [Alberdi *et al.* 2011]. 36

Figure 2.15: Various styles of flow conditioners [Cui and Webster 1994]. 38

Figure 2.16: Geometric nozzle positioning variables. 39

Figure 3.1: Cross-section of circular stock aluminum nozzle used to create an identical RP nozzle. 41

Figure 3.2: Sample of RP nozzle feasibility testing; jets issuing from (a) aluminum nozzle and (b) RP nozzle under the same conditions: flow rate 37.9 LPM. 41

Figure 3.3: Results of RP nozzle durability testing with one standard deviation of uncertainty. 42

Figure 3.4: Internal surface of two RP nozzles (a) before and (b) after extended use. 43

Figure 3.5: Axial vortices induced in (a) radially symmetric and (b) asymmetric nozzle geometries. 44

Figure 3.6: Example of axis switching in a free jet, as seen from simultaneous minor and major axis views [Amini and Dolatabadi 2012]. 44

Figure 3.7: Cross-sections of a sample nozzle revealing the major and minor axis profile curves. 45

Figure 3.8: Various aperture aspect ratios tested, all measurements in millimeters; (a) 1.00, (b) 1.56, (c), 2.45. 47

Figure 3.9: Geometric properties of a sample fourth-order Bezier curve. 48

Figure 3.10: Cutaway of a sample nozzle, showing the profile curves with the shortest and longest arc length. 49

Figure 3.11: Envelope of testable curves when aperture aspect ratio and exit angle are held constant. 51

Figure 3.12: Sample profile curve with control points defined along the imposed constraint lines. 52

Figure 3.13: Flowchart representing the algorithm of the MATLAB code used to generate profile curves based on user-input. 53

Figure 3.14: Orientation of planes in which profile curves are defined. 54

Figure 3.15: Ten equally spaced planes used in Josh Latka's work. 55

Figure 3.16: Sample nozzle as both a CAD model and final rapid-prototyped product. 56

Figure 3.17: (a) Stock and (b) customized setup of coolant delivery system in the Blohm Planomat grinding machine. 57

Figure 3.18: Schematic and photograph of nozzle assembly. 58

Figure 3.19: (a) Major and (b) minor axis views of sample jets 1 and 2, with locations of observed divergence angle and jet width measurements indicated. 59

Figure 3.20: (a) Minor axis and (b) major axis jet divergence values as functions of both the major axis exit angle and minor axis exit angles; multiple flow rates are super-imposed. Constant aperture aspect ratio of 1.56; constant arc length range of 0.0 mm. 61

Figure 3.21: (a) Minor axis and (b) major axis jet divergence as functions of both the arc length range and minor axis exit angle; multiple flow rates are super-imposed. Constant aperture aspect ratio of 1.56; constant major axis exit angle of 50°. 63

Figure 3.22: (a) Minor axis and (b) major axis jet divergence as functions of both aperture aspect ratio and minor axis exit angle; multiple flow rates are super-imposed. Constant arc length range of 0.00 mm; constant major axis exit angle of 50°. 65

Figure 3.23: Digital images of the lowest divergent elliptical jet tested in the (a) minor and (b) major jet axes; testing flow rate of 33.3 LPM. 66

Figure 3.24: Topographical diagram of a nozzle having an aperture aspect ratio of 1.56, arc length range of 0.00 mm, and minor and major axis exit angles of 80° and 40°, respectively. 67

Figure 3.25: Digital image of a jet with a coherency of 0.92 emerging from a circular nozzle. 67

Figure 3.26: Jet showing low fluid homogeneity, (a) minor and (b) major axis views. ... 68

Figure 3.27: Theoretical circular jet cross-sections at the grinding zone for various flow rates. 68

Figure 3.28: Vertical jet orientation; jet expansion at the grinding zone for various flow rates. 69

Figure 3.29: Horizontal jet orientation; jet expansion at the grinding zone for various flow rates. 69

Figure 4.1: Photograph of experimental apparatus immediately prior to start of cutting. 73

Figure 4.2: Pressures and flow rates achievable with equipped coolant system for various pump RPM and various aperture diameters; fluid units converted to SI from source figure [Murphy *et al.* 2007]. 76

Figure 4.3: (a) Profiled workpiece and (b) dimensions. 76

Figure 4.4: Achievable jet velocity at the nozzle for various jet pressures, aperture equivalent in area to a circle 3.5 mm in diameter. 77

Figure 4.5: Circular jet cross-sections 200 mm downstream for various pressures. 79

Figure 4.6: Elliptical jet cross-sections 200 mm downstream for various pressures; “vertical jet orientation”. 80

Figure 4.7: Elliptical jet cross-sections 200 mm downstream for various pressures, “horizontal jet orientation”. 81

Figure 4.8: Width of the three jets at the grinding zone with respect to jet pressure. 82

Figure 4.9: Cross-sectional area of various jets available to the grinding zone. 82

Figure 4.10: Aspect ratio of expanding jet cross-sections. 83

Figure 4.11: Three possible jet vertical offset positions: (a) no overlap, (b) half-width overlap, and (c) full-width overlap. 84

Figure 4.12: Possible elliptical aperture orientations: (a) horizontal nozzle (or "vertical jet") and (b) vertical nozzle (or "horizontal jet"). 84

Figure 4.13: Spindle power readings for jet vertical offsets of no overlap, half-width overlap, and full-width overlap, (a) horizontal and (b) vertical jet orientation. 86

Figure 4.14: Photograph of workpiece mounted in profilometer. 88

Figure 4.15: Combination of "upper" and "lower" profile measurements. 89

Figure 5.1: Parabola involved in horizontally aligning profile curves. 91

Figure 5.2: Desired profile and profile error in comparison to available fluid flow. 92

Figure 5.3: Form error between measured profile and desired profile. 93

Figure 5.4: Measured and desired profiles, available fluid flow, and form error as measured at three positions along the length of a sample workpiece, circular nozzle. 95

Figure 5.5: Wheel breakdown in the corners of the profile, leading to propagation of profile form error, horizontal elliptical jet orientation. 96

Figure 5.6: Summary of form error propagation along the length of the workpiece for all jet pressures, feed rates, and jet orientations; trials with wheel breakdown removed. 97

Figure 5.7: Summary of experimental averaged surface roughness values for all jet pressures, feed rates, and jet orientations, including all trials with wheel breakdown. 98

Figure 5.8: Summary of experimental averaged surface roughness values for all jet pressures, feed rates, and jet orientations, trials with wheel breakdown removed. 99

Figure 5.9: Horizontal elliptical nozzle and resultant vertical jet superimposed over the grinding zone to show approximate coverage area. 101

Figure 5.10: Locations of the grinding wheel with respect to critical points on a power trace. 103

Figure 5.11: Summary of power consumption values for all experiments that used a feed rate of 100 mm/min. 105

Figure 5.12: Summary of power consumption values for all experiments that used a feed rate of 150 mm/min. 106

Figure 5.13: Summary of power consumption values for all experiments that used a feed rate of 200 mm/min. 107

Figure 5.14: Summary of total consumed power values for all jet pressures, feed rates, and jet orientations, including trials where wheel breakdown occurred. 109

Figure 5.15: Summary of total consumed power values for all jet pressures, feed rates, and jet orientations, trials where wheel breakdown occurred removed. 110

Figure 5.16: Summary of average cutting power values with 1.5 kW burn limit, includes trials where wheel breakdown occurred. 111

Figure 5.17: Summary of average cutting power with 1.5 kW burn limit, trials where wheel breakdown occurred removed. 112

Figure 5.18: Cutting, plowing, and rubbing regions of chip formation. 113

Figure 5.19: Summary of average normal force values in trials without wheel breakdown. 114

Figure 5.20: Summary of average tangential force values in trials without wheel breakdown. 115

Figure 5.21: Tangential and normal forces overlaid with the force ratio for a sample workpiece; 150 mm/min feed at 3.21 MPa jet pressure. 116

Figure 5.22: Attritious wearing of an abrasive grain. 117

Figure 5.23: Summary of averaged force ratio, trials with wheel breakdown removed. 118

Abstract

A novel method was developed to design and fabricate nozzles capable of producing low-divergence jets of fluid. An array of unique fourth order Bezier curves was used to define the internal surface geometry. Rapid prototyping was used for fabrication. Myriad experiments were conducted to investigate effects of nozzle geometry on the emerging jet. Nozzle apertures were elliptical in shape, and the jets exhibited elliptical cross-sections with divergence varying predictably. Image analysis was performed to determine trends in jet behavior; thus leading to general design parameters from which nozzles capable of creating jets of specific shape and size can be created. Jet divergence angles were found between 0 and 13°. Nozzle aperture aspect ratios were varied from 1.00 to 2.45.

An elliptical jet was developed with 0.4° and 0.9° divergence in the major and minor axes, respectively. Nozzle geometry consisted of uniform arc lengths around the internal contouring, major and minor axis exit angles of 40° and 80°, respectively, and an aperture aspect ratio of 1.56. Performance of this elliptical nozzle was compared to that of a circular nozzle via profiled creep feed grinding trials of varying feed rate, jet pressure, and jet alignment. Results indicate that the circular nozzle performs similarly to the horizontally aligned elliptical nozzle for jet pressures in excess of 1.72 MPa. The vertically aligned elliptical nozzle caused wheel breakdown more consistently than any other nozzle. For the grinding apparatus used, the ideal cutting parameters found were: wheel speed 23 m/s, depth of cut 1.78 mm, feed rate 200 mm/min, jet pressure in excess of 3.21 MPa. All jet study and grinding experiments were performed with a customized cooling system on a Blohm Planomat 408 computer numerically controlled grinding machine using CimCool CimTech 310 cutting fluid. Jet study experiments used cutting fluid at a Brix concentration of 6.1, while grinding experiments used a more standard 3.1%. Ambient temperature of the coolant was held at 19°C.

List of Abbreviations and Symbols Used

A	Area of aperture
a	Semi-major axis of the elliptical aperture
B	Bezier curve equation
b	Semi-minor axis of the elliptical aperture
d	Depth of cut
D	Grinding wheel diameter
i	Iteration variable in Bezier curve equation
l_c	Length of contact
MRR	Material removal rate
n	Degree of Bezier curve, number of data samples (given context)
η_{cut}	Cutting efficiency
P	Bezier curve control point
P_{total}	Total power consumed during grinding process
Q	Coolant flow rate in GPM
R_a	Surface roughness
$R_{a,avg}$	Average of surface roughness along the length of a workpiece
r	Radius of elliptical aperture in the specified profile plane
S	Arc length of Bezier curve, denoted by a *desired* or *calculated* subscript
t	Uncut chip thickness or Bezier curve step parameter (given context)
v	Grinding wheel peripheral surface speed
v_w	Workpiece velocity, “feed”
v_j	Jet velocity at the aperture
x	x-value of point on Bezier curve
y	y-value of Bezier curve, y value of datum profile curve (given context)
y_i	y-value of surface data point, y value of profile curve (given context)
α	Nozzle exit angle

Acknowledgements

I would like to thank my supervisors Dr. Andrew Warkentin and Dr. Robert Bauer of the Mechanical Engineering Department at Dalhousie University for their invaluable guidance and wisdom throughout this project. Their styles of council are completely complementary, and without both of them this research would not have continued. Also, thank you to my committee members Dr. Dominic Groulx and Dr. Uday Venkatadri, and also to Dr. Willie Quinn from St.Francis Xavier University, for their advice, support, and timely input into this work. Also, the work of a more tech-savvy student than I, Josh Latka, stream-lined my work and made completion of my research much easier; thank you.

I would also like to thank my parents for their perpetual encouragement, support, and blatant prodding—help that I hope to never take for granted. Also, without the unwavering assistance of an impressively dedicated—perhaps reluctant at times—grinding machine guru and close friend Mokhtar Mohamed, none of this work would have been achievable.

Financial resources for this research were provided by the Natural Sciences and Engineering Research Council of Canada (NSERC) and the Canadian Foundation for Innovation (CFI).

And finally, my editor-in-chief, sanity-checker, sage, recess buddy, all-around partner, and love of my life, Niki Siabanis, has made life not only possible, but great during this research. I cannot thank her enough but will continue to try.

CHAPTER 1 INTRODUCTION

This introductory chapter will begin by providing an overview of the research topic, followed by a description of grinding theory that will involve cutting mechanics, necessary equipment and tool maintenance, preparatory procedures, and waste disposal. In combination, Chapter 1 and Chapter 2 form a comprehensive review of the appropriate literature.

1.1 Background

Grinding—and machining in general—is a process wherein a specifically shaped tool is pressed into a workpiece with some relative velocity to effect a shape change. In the case of grinding, this tool consists of many individual microscopic cutting surfaces embedded in a porous rotating disc; a grinding wheel. The grinding wheel is pressed circumferentially against a laterally translating workpiece to remove some specified depth of material across the surface region as uniformly as possible. Material removal through the grinding process is an inefficient cutting process at best, and therefore generates a large amount of excess energy in the form of heat that must be controlled. To this end, the effective use of lubricant, coolant, and debris removal are key requirements for a high-tolerance end-product surface finish. In practice, the typical method of lubricating, cooling, and removing debris involves the calculated use of application-specific cutting fluid; this issue is the central focus of the following research.

1.1.1 Research Topic Overview

This manuscript accounts for experiments conducted in cutting fluid nozzle development and subsequent experimental validation. Nozzles used to apply cutting fluid to an active cutting zone, generally, are circular or rectangular in cross-section, as illustrated schematically by two typical nozzles in Figure 1.1. Ideally, they are smooth-walled and continuous internally, but occasionally space constraints make this geometric ideal impossible. In addition, the internal geometry tends to taper inward at some arbitrary angle towards the final aperture.

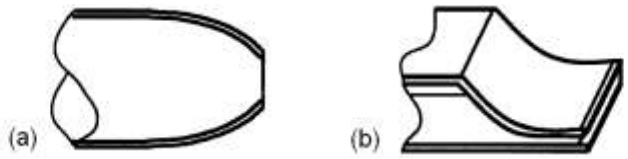

Figure 1.1: Two typical coolant delivery nozzles used in industry: (a) circular and (b) rectangular [Webster *et al.* 1995].

Thus far in machining literature, little attention has been paid to the details of this internal contouring, rather, a "by-eye" approach has generally proven satisfactory. In profiled grinding, where the depth of cut can vary dramatically across the width of the workpiece and the possibility of both workpiece and tool damage is high, as shown in Figure 1.2, it is critical to apply cutting fluid such that lubricant and coolant reach the entire cutting zone.

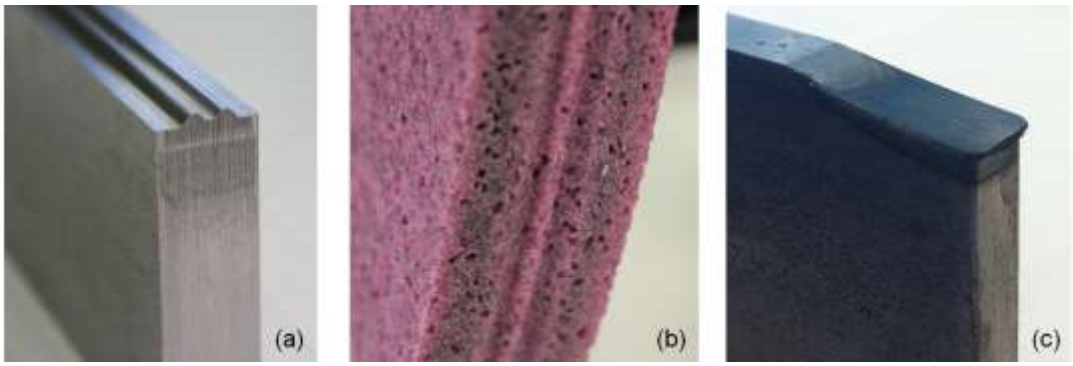

Figure 1.2: (b) A typical profiled workpiece, (b) tool wear on a profiled wheel, and (c) workpiece damage.

For this purpose, research has been conducted to generate an oval-shaped low divergence jet of cutting fluid through the manipulation of the internal geometry of nozzles. This research will then be used to investigate the differences aperture shape has on the resultant grinding process with respect to typical grinding parameters such as jet pressure and workpiece feed rate. Ideally, an elliptical nozzle would result in a more effective distribution of the coolant flow across a profiled cut as compared to a single circular jet, which only applies coolant to the central region of the workpiece. An alternative method of using multiple closely-spaced circular jets has been implemented in various cutting scenarios and has proven effective, but where space, budget, and tooling limitations are

present, a single, simple nozzle may be the only feasible coolant option. As will be discussed in more detail in Chapter 2, there is a maximum limit to the amount of fluid that can enter an active cutting zone, and as a result, the use of an excessively large single jet or extraneous smaller jets risks wasting cutting fluid; an unnecessary environmental and health hazard. These regions of coolant application are illustrated schematically in Figure 1.3. Using a low divergence oval jet, therefore, has the potential to optimize the amount of coolant required, improve workpiece surface finish, decrease wheel wear, and reduce surface error on the workpiece. Within a range of various experimental parameters—namely, jet pressure and workpiece feed rates—the effects of nozzle aperture shape will be studied.

Figure 1.3: Potential fluid coverage across a profiled workpiece using (a) a circular jet, (b) multiple jets, and (c) an elliptical jet.

In summary, the objectives of this research include:

- Develop a cost-effective fabrication method to create complex reproducible nozzles.
- Determine the effects on jet behavior of a variety of internal nozzle geometric parameters.
- Compare the performance of a low divergence elliptical jet to that of a circular jet in terms of the results of a creep-feed grinding process.

1.1.2 Thesis Outline

The remainder of this thesis is broken into five chapters, as shown in the flowchart of Figure 1.4. Following this introduction, the rest of Chapter 1 will move on to outline the general procedures involved in grinding, such as the cutting mechanics, wheel and fluid

types, fluid hazards and disposal, and the various forms of possible workpiece damage. Chapter 2 will discuss in detail the process of cutting fluid application, including an overview of available application methods, difficulties that must be overcome to achieve coolant penetration, and existing research conducted into theories behind the design of coolant nozzles. Next, Chapter 3 will begin to describe the research carried out for this thesis by detailing the design, fabrication, and testing stages of the newly developed nozzles. Chapter 4 will then outline the procedure through which several new nozzles will be compared to an industry standard nozzle by evaluating the performance during profiled creep-feed grinding scenarios. Chapter 5 will summarize the results and highlight conclusions to be drawn from the research. Finally, Chapter 6 will summarize the conclusions and propose avenues of further research in the area of specialized nozzle design.

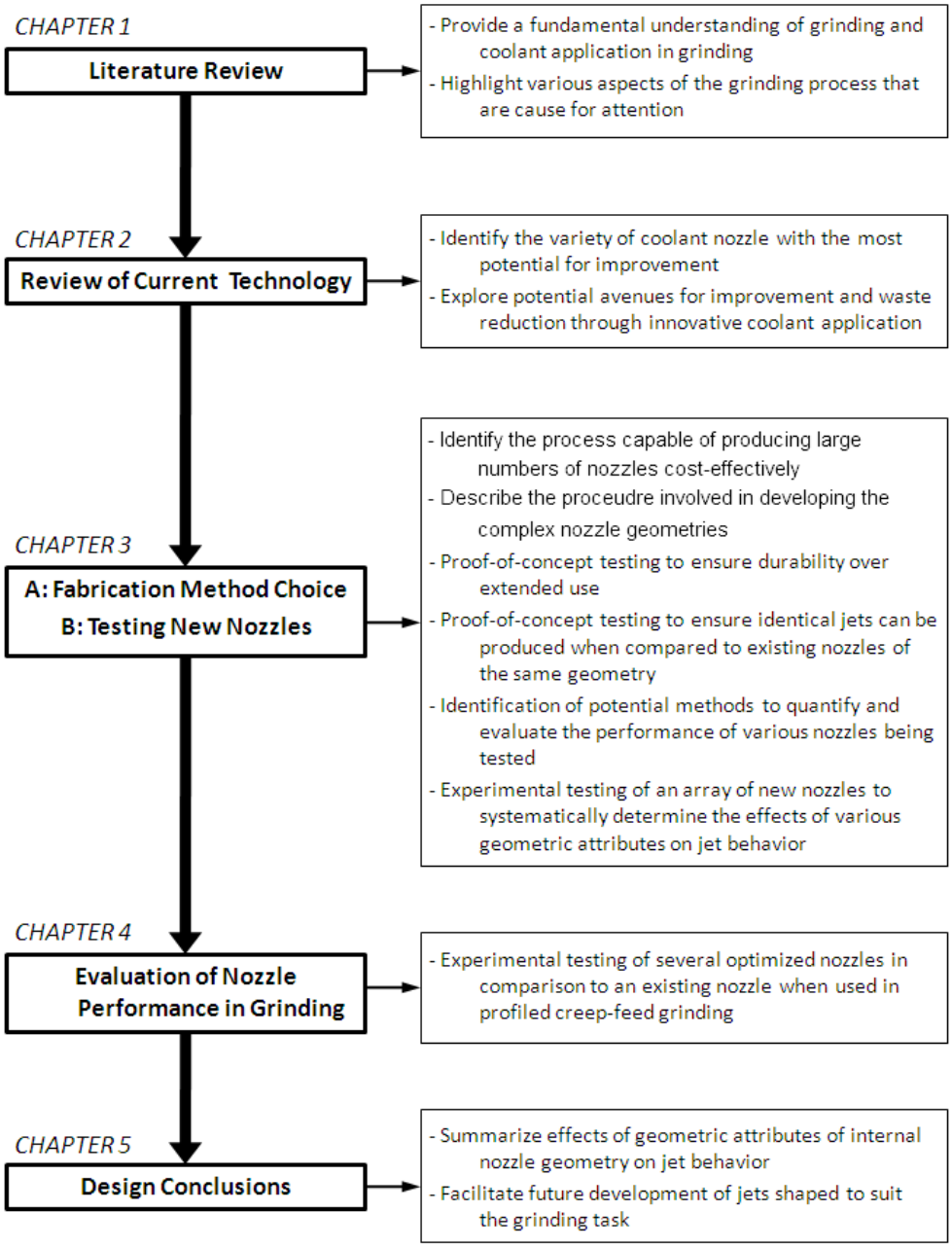

Figure 1.4: Outlined flow of manuscript.

1.2 Grinding Theory

This section will highlight the basics of the grinding process, such as the necessary equipment, general cutting mechanics, tool and workpiece preparation, wear, and damage, and the hazards and disposal of waste materials.

1.2.1 Wheels

A grinding wheel consists essentially of abrasive grains—or grits—bonded together in the shape of a disc, as shown in Figure 1.5. Despite this apparent simplicity, five characteristics are used to determine the composition and behavior of a standard grinding wheel: grain material, grain size, porosity structure, bonding material, and wheel grade.

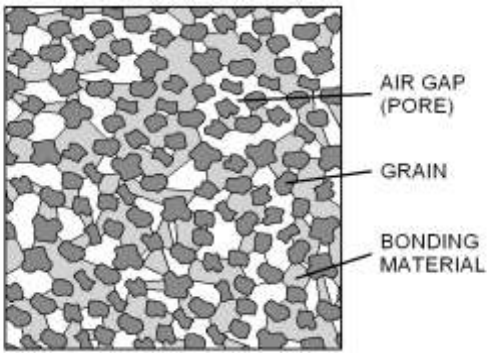

Figure 1.5: Detail of grinding wheel cross-section showing various structural components.

Abrasive grain material—chosen with respect to the hardness of the material to be ground—is typically one of four common materials, ranked here from softest to hardest: aluminum oxide (Al_2O_3), silicon carbide (SiC), cubic boron nitride (CBN), or diamond. Grain size is chosen with respect to the smoothness of the desired surface finish on the ground workpiece, with smaller grains yielding a smoother finish and coarse grains yielding higher material removal rates (MRR). Similarly, the porosity of the wheel is chosen based on the desired surface finish. A wheel with a larger proportion of air gaps to grains is termed "open", whereas a "dense" wheel contains smaller and fewer air gaps. Open wheels are used for high MRRs, whereas dense wheels are used for fine surface finishes. The bonding material that maintains the structure and rigidity of the grinding wheel is chosen based on the workpiece material properties; common bonding agents include silicate, rubber, resin, shellac, metal, and most commonly, a ceramic-based—or "vitrified"—bond. Finally, the grade of the wheel is marked by the strength of the bonding material in retaining individual grains. Choosing a wheel grade depends on the desired MRR and surface finish, with a softer grade more suited to low MRRs and hard workpiece materials and a harder grade suited to high MRRs and soft materials.

1.2.2 Cutting Mechanics

The primary force involved in a typical cutting process is shear: a tool is pressed into and then along a surface, thus forcing a small fragment, or chip, to shear off and reveal a new surface beneath. Forces that occur in the workpiece and tool point are dependent on a variety of geometric relations between the tool cutting edge and face of the workpiece, but an ideal cutting scenario will result in a shallow-slanted shear plane that allows chips to form and break off freely, as seen in Figure 1.6.

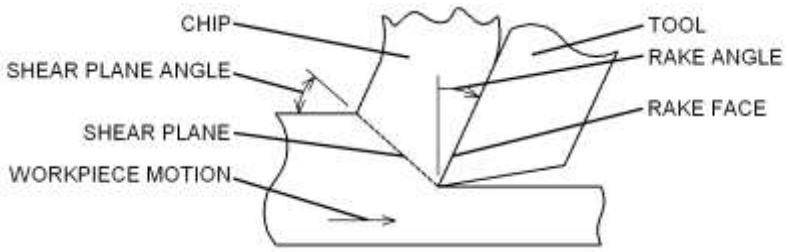

Figure 1.6: Schematic of idealized cutting model.

The axially directed normal and tangential forces are informative as to the efficiency of the process and can be measured through the use of a dynamometer affixed to the workpiece. The power output at the spindle can also be used in determining the efficiency of the grinding process. The geometric parameters and forces that can be measured or determined analytically in a typical grinding setup are illustrated schematically in Figure 1.7. The variables shown include: diameter D, wheel surface speed v, length of contact l_c, workpiece velocity v_w, and depth of cut d.

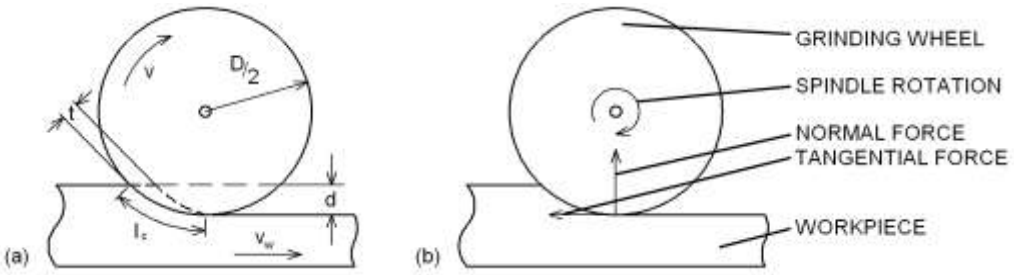

Figure 1.7: Overview of a grinding setup showing (a) geometric parameters and (b) measurable forces.

In grinding, an ideal cutting scenario does not occur due to the random nature of cutting surfaces present in a typical grinding wheel. Instead of a positive rake angle that can yield high material removal rates with low shear stress, grinding wheel cutting surfaces generally present large negative rake angles and, therefore, generate large amounts of shear force and friction in the workpiece when removing material. This typical grinding geometry is shown in Figure 1.8, along with several variables: workpiece velocity, or "feed", v_w, and depth of cut d.

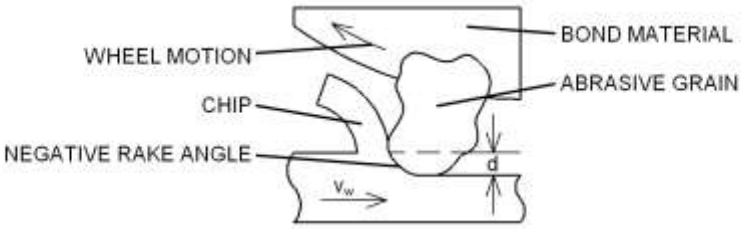

Figure 1.8: Typical geometry of the cutting process in grinding.

Not only are the forces higher in grinding than with other cutting operations, but the cutting parameters are also more sensitive; that is, with an improper depth of cut or a worn wheel surface, cutting will be replaced by highly inefficient rubbing or plowing. Rubbing is caused by an insufficient cutting depth wherein the wheel drags along the surface of the workpiece, effectively only generating heat. Plowing, similarly, is caused by an insufficient depth of cut, but instead results in plastic deformation of the workpiece surface. Both rubbing and plowing are troublesome in that they generate heat without removing material, which can lead to thermal damage and result in unacceptable material property changes. These three processes—cutting, plowing and rubbing—are shown schematically for grinding in Figure 1.9.

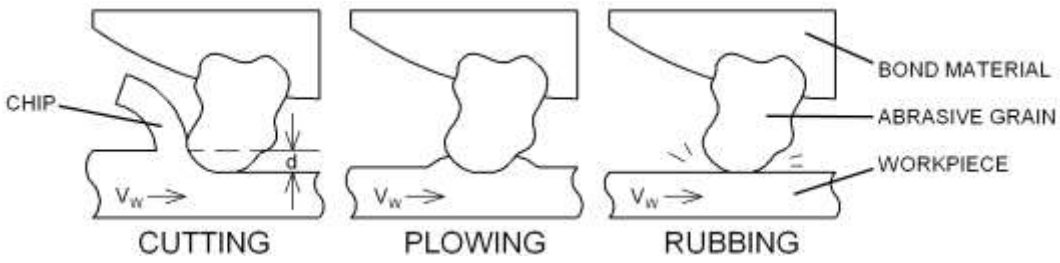

Figure 1.9: Schematic views of cutting, plowing, and rubbing phenomena in grinding.

The dangers of plowing and rubbing—or indeed any cutting inefficiencies—lie in the realm of heat generation and transfer. As friction generated within the grinding zone is transformed into heat, the thermal energy begins to move to the four immediately adjacent heat sinks, namely: chips and debris, coolant—including the surrounding medium to a minor degree—the grinding wheel, and most importantly, the workpiece. With an ideal grinding setup, the largest portion of the generated heat will be carried away by the chips and coolant. A small amount of heat will radiate into the surrounding environment, but this portion is negligible compared to the potential heat sink of the workpiece. The wheel will also absorb a portion of the heat, but again, is not significant in comparison to the thermal energy transferred to the workpiece. If any grinding parameter such as feed rate, depth of cut, or wheel surface speed is too aggressive, the excessive grinding forces will generate enough heat to cause thermal damage. Similarly, an increase in plowing or rubbing—likely brought about by wearing of the wheel—will cause thermal damage [Malkin 1989]. Effective application of coolant can reduce the grinding forces and allow for more aggressive grinding parameters; therefore, choice of coolant application is of utmost importance in ensuring a satisfactory end product.

1.2.3 Types of Grinding

Several cutting scenarios are possible in a grinding operation. Spinning the grinding wheel such that the peripheral velocity of the wheel opposes the infeed of the workpiece, "up-grinding", is commonly used in creep-feed grinding where large depths of cut are required. Spinning the wheel such that the peripheral velocity matches the direction of the workpiece infeed, or "down-grinding", is used for surface grinding where small depths of cut are used to bring a piece within tolerance or improve the surface finish. In fact, surface grinding often uses a reciprocating motion wherein the workpiece is oscillated bi-directionally with respect to the grinding wheel point of contact. When up or down-grinding is used in conjunction with a jet of cutting fluid, the jet can be placed such that the peripheral motion of the grinding wheel pulls the fluid into the grinding zone or repels it. For large depths of cut where heat is generated rapidly, the fluid jet must be placed so that the wheel pulls the fluid into the grinding zone.

1.2.4 Wheel Wear and Dressing

During the grinding process, the grinding wheel is worn in several ways, namely: grain fracture, bond fracture, attritious wear, and wheel loading. Grain fracture is the partial breakage of individual abrasive grains wherein some portion of the grain is left embedded in the wheel. Bond fracture is the breakdown of the bonding material that results in grains being removed completely from the wheel. It is typically observed as irregular pock marks or a general deformation worn into the surface of the wheel. The removal of used grains results in fresh grains being exposed and, if controlled in the short term, can lead to an increase in cutting efficiency. If rapid wheel break down is allowed to continue, however, the power consumption of the wheel will drop in accordance with the improved efficiency, but at some point the process will become chaotic and perhaps lead to catastrophic failure. Attritious wear is the dulling of individual cutting grains through the creation of "wear flats"—flat spots worn into the active tips of cutting grains due to rubbing. Grain fracture, bond fracture, and wear flats are detailed in Figure 1.10.

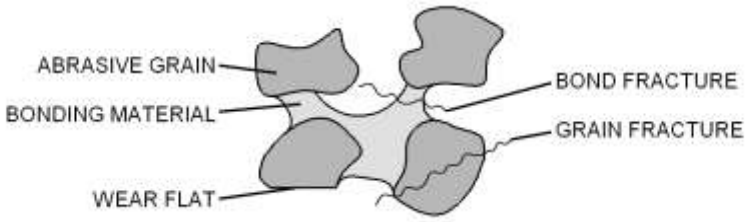

Figure 1.10: Detailed view of grain fracture, bond fracture, and wear flats.

Wheel loading is a combined effect of grain fracture, bond fracture, and the actual material removal process of grinding; that is, as grinding occurs, waste material removed from the workpiece and debris removed from the degrading wheel, collectively referred to as swarf, are gathered within pores on the grinding wheel surface, thus reducing the efficiency of any exposed cutting grains. Figure 1.11 compares the visually apparent varieties of wheel wear; namely, grain and bond fracture and wheel loading.

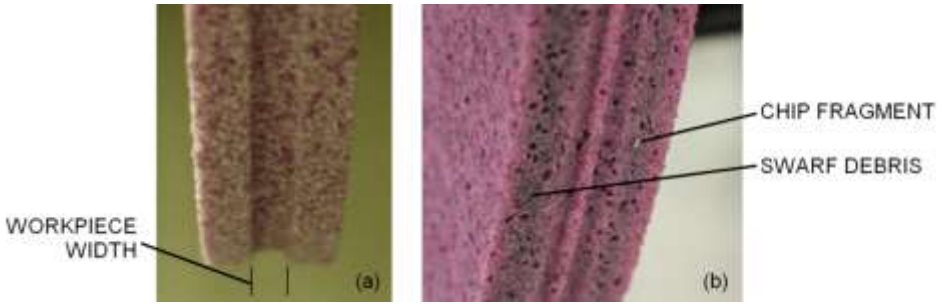

Figure 1.11: (a) Extreme example of grain and bond fracture on a flat-profiled wheel [Steffen 2004] and (b) typical wheel loading on a profiled wheel.

In addition to wheel damage observed visually, power output as measured at the spindle can also be used to determine the presence of these types of wear. Figure 1.12 typifies several sample power curves obtained by modifying feed rate and coolant delivery parameters, summarized in the legend below the figure. There are numerous grinding scenarios that will yield similar power curve trends; explanatory examples are provided. Grain and bond fracture will yield a drop in power followed by large random fluctuations, as shown by the region marked (a) and the steady drop in power immediately preceding it. Attritious wear can be attributed to a steadily rising power curve, as illustrated by (b). When grinding parameters such as feed rate, depth of cut, or coolant flow rate are too aggressive, a power curve such as that represented by (c) will indicate irreparable damage is likely occurring on the workpiece surface in the form of thermal damage. The lower overall power used by curves (b) and (c) as compared to curve (a) is attributable to both slower feed rates—125 and 250 mm/min, respectively, as compared to 300 mm/min—and varying coolant parameters as indicated on the figure.

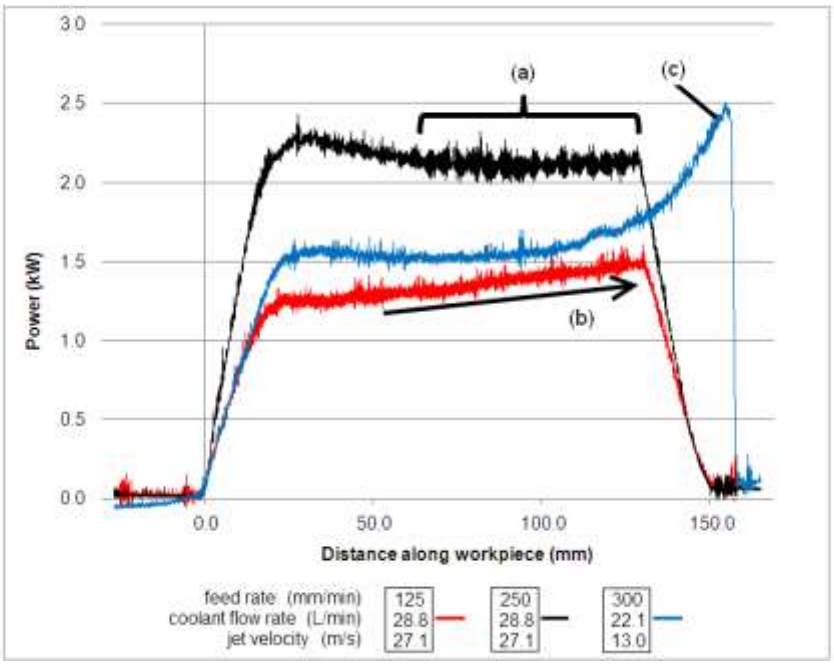

Figure 1.12: Power of the spindle as a result of (a) grain and bond fracture, (b) attritious wear, and (c) wheel loading. Grinding parameters listed in legend.

Wheel wear increases the specific energy of the cutting process, where specific energy can be generally defined as the force used per unit of material removed. As this specific energy is increased, the risk of both thermal damage and surface imperfections rises. Therefore, to counteract wheel wear, the grinding wheel must be dressed frequently. Dressing involves the removal of the outer layer of worn and broken grains along with any loaded surface pores. This dressing process results in a small diameter change that must be taken into account when grinding immediately after dressing. There are numerous dressing procedures available to return a worn grinding wheel surface to its initial state, such as single or multi-point dressing and roll dressing, as shown in Figure 1.13. Single and multi-point dressing involves the use of one or more diamond-tipped dressing tools that are passed linearly across the surface of the grinding wheel as it rotates. Two variables control this dressing operation: dressing feed and dressing lead. Dressing feed refers to the depth at which the dressing tool engages with the wheel—i.e. the depth of cut—and the dressing lead refers to the speed at which the dressing tool moves across the grinding wheel surface—i.e. the cross-feed. A deeper dressing feed exposes more new grains and thus results in a higher cutting efficiency. The behavior of

the wheel during dressing—that is, the number of new grains exposed and the resultant fractured surface of the grains—is largely dependent upon the characteristics of the chosen grinding wheel in combination with the chosen dressing parameters. Roll dressing employs a cylinder coated with abrasive diamond grits that is pressed into the grinding wheel. Ideally, the roll dresser has a peripheral velocity 85% that of the grinding wheel. This method is more efficient than single or multi-point dressing and can be employed simultaneously with the grinding process, as the entire width of the grinding wheel is dressed uniformly. Roll dressing can also be used to impart a desired profile to the grinding wheel if a contoured roll dresser is used; the dressing method used exclusively in this research.

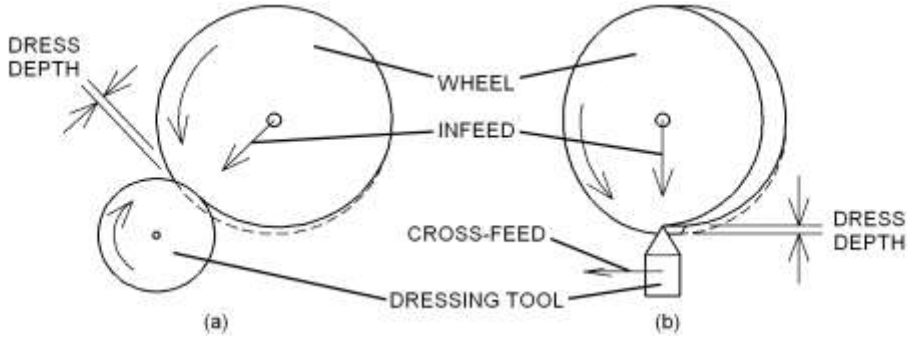

Figure 1.13: (a) Typical rotary dressing setup and (b) single-point dressing setup.

1.2.5 Possible Workpiece Damage

Besides excessive roughness and surface error, thermal damage is the most likely source of unsatisfactory results in grinding. As a result of the grinding mechanics, friction—and subsequently heat—is generated continuously throughout the region of contact between the grinding wheel and the workpiece. As discussed in Section 1.2.2, if the grains are not sharp enough to cut and remove material, the less efficient processes of rubbing or plowing create more heat than necessary. This excess heat can cause surface burns and cracks in the workpiece perpendicular to the wheel motion; defects which can potentially be removed by repeating the grinding operation with less aggressive parameters to remove the affected surface material. Irreparable defects can occur, however, when excess heat results material changes to some depth below the finished surface. This

damage could include strain hardening and tempering—phenomena illustrated in Figure 1.14—or residual stresses caused by uneven plastic deformation of the surface.

The process of strain hardening followed by tempering on a steel workpiece surface is shown in Figure 1.14. Instead of a constant depth of cut, the depth of this grind was linearly increased along the length of the workpiece, as noted on the horizontal axis. Between 0 and 0.7 mm there is an expected linear rise in power due to the increasing depth of cut, but at 0.8 mm a large "burn spike" in the power indicates a sudden hardening of the steel surface with an associated spike in grinding power. Beyond 0.8 mm, grinding continues at a much lower power level, indicative tempering—or softening—of the metal surface has occurred. The fundamental material changes can produce unacceptable surface finishes or material properties, and are therefore to be avoided.

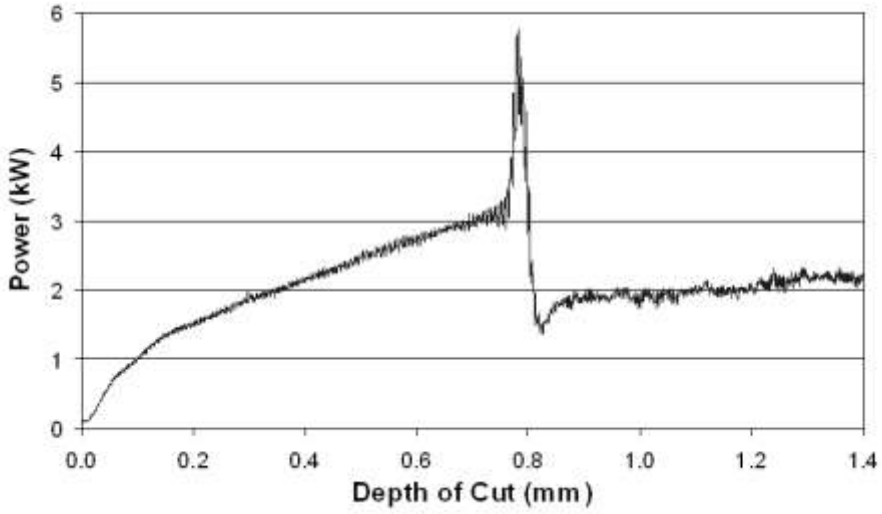

Figure 1.14: Observed power spike associated with film boiling of the cutting fluid [Skerlos 1998].

1.2.6 Cutting Fluid

Damage to materials being ground can be mitigated through prompt removal of waste and effective application of coolant and lubricant. These tasks can be accomplished by directing specially formulated cutting fluid at the region of contact between the grinding zone and workpiece. Due to the importance of cutting fluid application in grinding,

innovative methods of application are widely sought. Simply applying more coolant is not a feasible option since chemical contact with machine operators and eventual disposal into the environment are hazards that must be addressed. In terms of immediate human dangers, aerosol mist that forms when a high velocity jet of cutting fluid impacts a tool is an excellent vector for a variety of bacteria, endotoxins, and fungal spores capable of living in the highly oxygenated, nutritious fluid [Skerlos 1998]. Extended machine operator contact with the mist can also cause chronic respiratory health conditions, in addition to any dermatitis conditions that may arise through contact with the skin [Greaves 1997]. Cutting fluid also becomes contaminated with the workpiece material—which could potentially be a toxic metal or alloy—and therefore presents recycling and disposal challenges in terms of cost and environmental repercussions. With these considerations in mind, the ideal solution is to apply less coolant more efficiently.

1.3 Summary

Grinding is a high-energy, low-efficiency machining process that can yield very high tolerances and very fine surface finishes if it is carried out effectively. The selection of a grinding wheel based on the characteristics of the workpiece material should be followed by the creation of a set of cutting parameters that result in the most efficient cutting mechanics allowable by the geometry of the abrasive cutting edges. Next, the wheel must be dressed periodically to maintain surface finish consistency and prevent excess wheel wear. Finally, a coolant delivery method using minimal fluid must be selected and properly positioned with respect to the grinding zone to prevent workpiece damage. The details of this final step will constitute the remainder of this manuscript.

CHAPTER 2 CUTTING FLUID THEORY

As discussed in Chapter 1, the machining process of grinding is friction and power intensive, a side-effect of which is the requirement for methods of lubrication, coolant, and waste removal. There are numerous delivery options for a variety of substances that lubricate, cool, remove waste, or some combination thereof. Understandably, the grinding scenario in question will play a large role in determining the optimum delivery method, but several physical and geometrical constraints—such as the boiling limit of a fluid, entrained air around a spinning disc, or the discrepancy between fluid velocity and wheel velocity—also affect the choice. This chapter will first describe a variety of common application methods and their advantages and disadvantages, and then highlight several physical obstacles that must be overcome for the fluid to be effective. The final section, Section 2.5, will then discuss in detail the characteristics of a coherent jet of cutting fluid, the method of coolant delivery used exclusively in this research.

2.1 Types of Cutting Fluid

The following section compares several general categories of cutting lubricant and cutting fluid application.

2.1.1 Solid and Paste Lubricants

A powdered solid mixed with oil to form slurry can be used as a lubricant. These materials are chosen based on their lubricity properties, and common choices include graphite, calcium fluoride, or molybdenum disulfide. These can be applied in several ways: a hydraulically controlled container can be used to release measured quantities of paste onto a small dispersal wheel pressed against the grinding wheel; a spring loaded dispenser can be used to hold a soft nozzle against the grinding wheel while paste is directed onto the wheel surface; pockets of the material can be embedded into the grinding wheel during wheel construction, revealing more paste as the wheel wears. The advantages of using a paste are mainly an increase of lubricity in the grinding zone over other methods, thus reducing tangential forces and generated heat (Shaji and Radhakrishnan 2001]. This reduction in heat is sometimes enough to allow for small depths of cut without risking thermal damage, but the lack of cooling and waste removal

means it is impractical for the large depths of cut used in processes like creep-feed grinding where large amounts of material are removed quickly. Another disadvantage of paste lubricant is that constant grinding of the paste directly into the wheel causes more rapid wheel wear and clogging, necessitating continuous wheel cleaning equipment or more frequent wheel dressings to remove worn grains and embedded debris.

2.1.2 Gas and Mist Lubricants

Another form of cutting lubricant is applied in the form of a gas. This gas can be pure air or emulsified oil delivered as a mist. Generally this form of lubricant performs similar tasks to paste lubricants in that they provide mainly lubrication with little—if any—cooling or waste removal. Air has one quarter the specific heat capacity and a coefficient of heat transfer between 50 and 100 times smaller than water depending on the water quality, so in order for an air jet to have a sufficient cooling effect on the workpiece it must be highly refrigerated and impact the workpiece with high volume. Nguyen and Zhang [2003] tested air cooled to −20°C, compressed to 600 kPa and with a flow rate of 4095 liters per minute (LPM). They found they could lower grinding forces and maintain manageable temperatures for shallow depths of cut below 15μm, but any deeper and the workpiece would begin to show thermal damage and surface strain. Jeng *et al.* [2009] tested the fundamental cooling properties of numerous high-pressure air jets directed at an array of heat sinks and determined that increasing the surface area of the heated fins and the jet turbulence at the point of contact were the two main factors that could increase the rate of heat transfer. To implement this phenomenon in grinding would require an array of heat sinks in direct or close contact with the active grinding zone of the workpiece—a complicated proposition that would result in large quantities of wasted material.

Applying a small quantity of emulsified oil to an air jet in a process known as Minimum Quantity Lubricant (MQL) can dramatically increase the possible rate of heat transfer and increase lubricity while keeping the amount of fluid to dispose of to a minimum. Depending on the choice of oil, an MQL setup can result in only 10-20% higher forces in the grinding zone than a typical stock flood liquid coolant system for certain highly

porous grinding wheels. 30-40% higher forces are also achievable with low porosity wheels [Tawakoli *et al*. 2011]. For grinding with shallow depths of cut the decision to use MQL, therefore, is a compromise between slightly higher forces and temperatures in place of a significantly smaller quantity of cutting fluid.

2.1.3 Liquid-Based Cutting Fluids

Using a fluid-based coolant is by far the most common and practical method of cooling, lubricating, and removing waste from the grinding zone. Fluids are also useful in that they provide bulk mass cooling to any workpiece material not directly involved in the grinding process. Cutting fluids can be divided into four main categories based on their major components: straight oil, soluble oil in water, synthetic and soluble oils in water, and synthetic oil in water. The choice of fluid is based on the grinding parameters such as depth of cut and wheel speed: oil provides lubrication while water provides cooling [Salmon 1992]. In addition to carrying away chips and debris directly from the grinding zone, fluid spray to the sides and rear of the grinding zone can entrap any airborne particles and harmful gases created during the grinding process. This waste fluid can then be filtered and reused; an advantage over other forms of lubrication and coolant.

2.2 Issues in Application

The following section deals with issues in coolant delivery that must be addressed when designing a coolant or wheel cleaning jet; namely, the concept of useful flow, the boiling limit of a fluid, entrained air around a spinning disc, counteracting wheel loading, and the difficulties associated with applying coolant in profiled creep-feed grinding.

2.2.1 Useful Flow

The idea of useful flow is simple: the useful flow is the proportion of the applied flow that is used in the grinding zone to perform work. Increasing the applied flow will increase the useful flow until a certain limit, at which point the benefits of any additional fluid applied decline dramatically in significance. Therefore the useful flow of a grinding setup is important to determine for resource conservation. Several methods have been used to measure or approximate the useful flow. Experimental methods include setting up plates behind the grinding wheel to contain only the used fluid, or estimating the

thickness of coolant within the grinding zone via electrical resistance, dye, or equations, and also attempting to approximate the grinding zone with a smooth mock wheel and workpiece of known dimensions [Engineer *et al.1992*; Jin *et al.2003*]. Several attempts have also been made to numerically determine the amount of fluid that passes through the grinding zone by solving equations of fluid momentum and continuity, with results that agree fairly well with those observed [Chang 1997]. It has also been shown mathematically through solving Navier-Stokes equations that there is a theoretical limit to the amount of fluid that can pass through the grinding zone [Klocke *et al*. 2000].

The most widely accepted model of fluid motion through the grinding zone states that the fluid is pushed into the air pockets of the wheel by fluid pressure against the workpiece, is then carried through the grinding zone within the wheel, and afterward exits the wheel by centrifugal force. Based on this model, there are several grinding parameters that can influence the proportion of useful flow—generally only a very small portion of the applied flow, 4-30% [Engineer *et al.* 1992]. First, a higher porosity grinding wheel will provide more air pockets between the abrasive grains and bond material for coolant to ride through the grinding zone. Increases in wheel porosity have been experimentally and analytically observed to increase the flow rate of fluid through the grinding zone by Engineer *et al.* [1992] and Chang [1997]. An increase in wheel speed will increase the number of pores moving through the grinding zone and likewise the available space for fluid to enter the wheel [Gviniashvili *et al.* 2003]. Also, if coolant is applied at higher pressures it will be forced deeper into the grinding wheel and will increase the useful flow [Hartlen *et al.* 200817]. Keeping the wheel free of swarf will also allow more fluid to enter and exit the pores, increasing the possibility of fluid entering the wheel.

If the useful flow passing through the grinding zone is insufficient, the workpiece surface finish will show extensive damage at the microscopic level caused by an excess of friction and heat. Ramesh *et al.* [2004] observed plastic deformation when the coolant velocity was too high and the flow rate too low, and plowing when the coolant velocity was too low and the flow rate too high. If such deformations are allowed to continue or increase, permanent thermal damage and permanent strain hardening of the workpiece

surface layers will result. Numerous experimental, numerical, and simulated methods have been developed to estimate or measure the temperature in the grinding zone. A promising experimental example is that of Webster *et al.* [1994]: they developed a mock workpiece with a rounded profile that matched that of the grinding wheel periphery. Along this curved surface—effectively, along a theoretical chip length—they imbedded a thermocouple that could directly monitor the temperature of the workpiece surface as the wheel was brought into contact with the entire length of the mock grinding zone.

2.2.2 Boiling Limit

While the temperature in the grinding zone is below approximately 100°C, cutting fluid passing through it is in an entirely liquid state with a corresponding heat transfer coefficient determined directly by the properties of the fluid. However, as the temperature rises to between 100 and 130°C, water-based coolant enters the nucleate boiling phase where a dramatic rise in the rate of heat transfer occurs. Small bubbles of vaporized coolant are being rapidly formed and moved along the workpiece surface, increasing the motion of coolant with respect to the material surface and thereby allowing more heat to be removed from the cutting zone by conduction and convection. Above 130°C, water-based coolants will enter the film boiling phase in which fluid vaporizes on contact with the workpiece, creating an insulating layer of gas that slows the rate of heat transfer. If temperatures continue to rise, heat will slowly begin to pass through this insulating vapor barrier once again, but at much slower rates than prior to film boiling. Despite the fact that coolant receives only 10-40% of the total heat generated through friction in the grinding zone, it is a critical relief in order to maintain workable conditions when using typical grinding parameters [Banerjee *et al.* 2007].

Webster and Cui [1995] developed a method to experimentally test the grinding forces and in the process discovered that it would also experimentally show the film boiling limit. A small hole was drilled vertically into a workpiece into which a piezo-electric sensor was inserted to measure the pressure of coolant spray directed onto it. As the wheel approached the hole the hydrodynamic pressure would rise to a maximum positive peak as fluid was flung centrifugally down into the hole, decrease to a negative minimum

as the wheel crossed over the hole, and then level out to zero as the wheel moved away. A siphoning effect was responsible for this small negative peak as fluid was pulled up and away from the sensor by the rotation of the wheel. This phenomenon is shown graphically in Figure 2.1. If this minimum pressure occurred at a pressure value of 0, it was concluded that film boiling had occurred because there was no fluid remaining in the grinding zone to create the hydrodynamic siphoning effect. This method is, therefore, a means to test the film boiling parameters of a grinding setup.

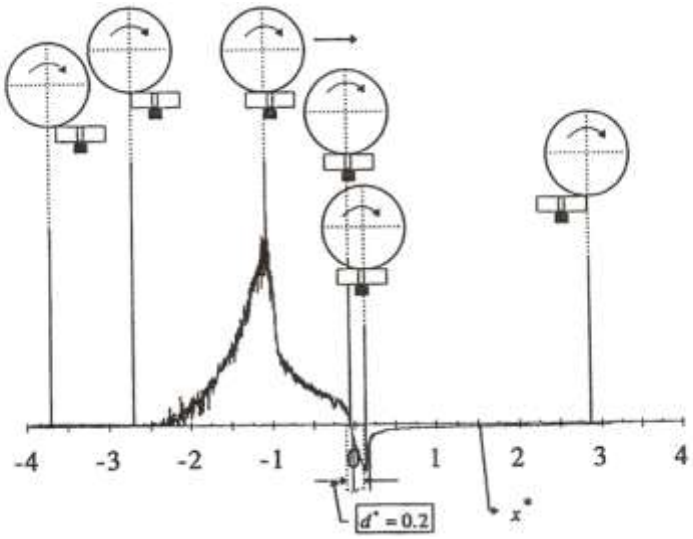

Figure 2.1: Hydrodynamic pressures measured on a workpiece during creep-feed cycle [Webster and Cui 1995].

2.2.3 Air Boundary Layer

A fundamental aspect of fluid dynamics is the concept of boundary flow—for grinding specifically, the entrainment of a protective layer of air around a rotating wheel presents difficulties to the effective application of cutting fluid. Ramesh *et al.* [2004] showed experimentally that the pressure at the wheel surface could be four to five times higher than that of the surrounding air, shown schematically in Figure 2.2.

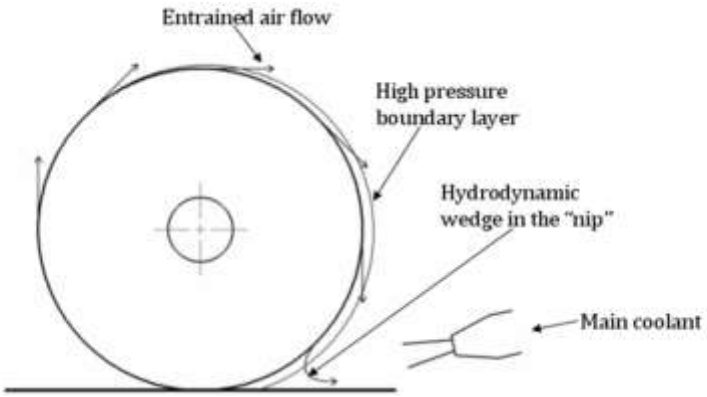

Figure 2.2: Air boundary layer entrained around a rotating disc.

Additionally, Wu *et al.* [2007] experimentally observed air within 0.5 mm of the wheel surface to be moving at 75% the velocity of the wheel for a wheel velocity of 20 m/s and RPM of 2088. The extent to which this air boundary layer plays a role in the grinding process is controversial, but Engineer *et al.* [1992] experimentally proved that a low velocity, high volume flow of coolant did not have enough energy to penetrate this layer of high-pressure, thus leading the way to the widely accepted ideal of applying coolant to the grinding wheel at a speed at least 80% that of the wheel periphery. If a coolant velocity this high is not possible due to pump constraints, then the use of scraper plates or high-pressure fluid jets can effectively shear off the layer of air, thus allowing low velocity coolant to enter the grinding zone without competition. Banerjee *et al.* [2007] developed a flood nozzle with a secondary opening aimed above the main outlet that served the sole purpose of breaking the air boundary layer in advance of primary coolant application, as seen in Figure 2.3. Results using this air scraper jet showed much higher useful flow rates as compared to a traditional single nozzle outlet.

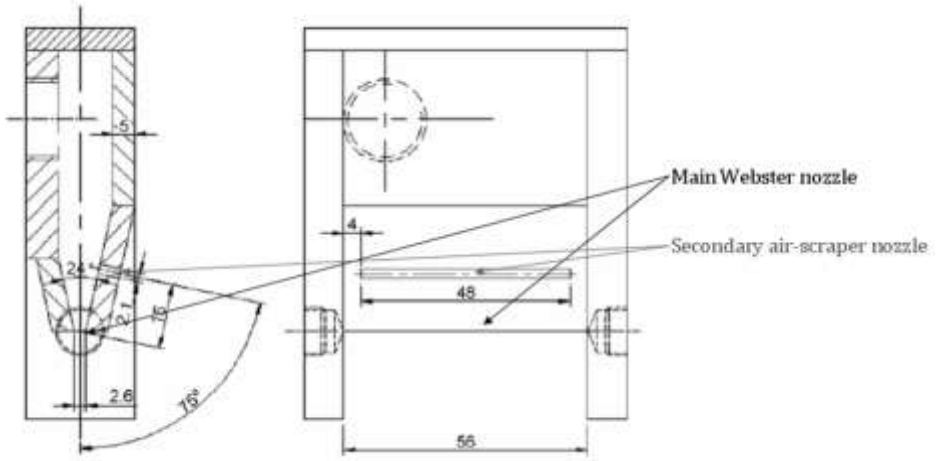

Figure 2.3: Flood nozzle developed with primary jet and secondary air-scraping jet [Banerjee *et al.* 2007].

2.2.4 Wheel Cleaning

Wheel cleaning is a procedure wherein a jet of high-pressure coolant or water is directed perpendicular to the peripheral surface of the grinding wheel as a preventative measure against wheel clogging and wheel grooving. A primary coolant jet is typically not powerful enough, but a high-pressure jet can forcefully dislodge debris and loose abrasive particles that would otherwise increase friction in the grinding zone and decrease the cutting efficiency of the grinding wheel. If used simultaneously with the active grinding process, wheel cleaning can reduce the dressing requirements on the grinding wheel. According to research by Cameron [2010], a high-pressure cleaning jet directed at the proper velocity and flow rate can reduce the number of dressing passes required to obtain an acceptable surface finish three-fold.

2.2.5 Profile Grinding

Profile grinding is a grinding procedure wherein the grinding wheel imparts a desired profile to the workpiece. The wheel periphery can be given this profile at the time of manufacture, or it can be imparted through the use of dressing or machining afterward. If shallow depths of cut are utilized, the grinding process is no more challenging to implement than standard surface grinding. When combined with the high depths of cut associated with creep-feed grinding, however, profile grinding presents much higher risks for thermal damage. As shown in Figure 2.4, a profiled grinding cross-section may

present several challenges to a high-quality surface finish, namely, excessive depths of cut in certain regions, sharp corners that accelerate wheel wear, and regions where coolant may be difficult to apply effectively.

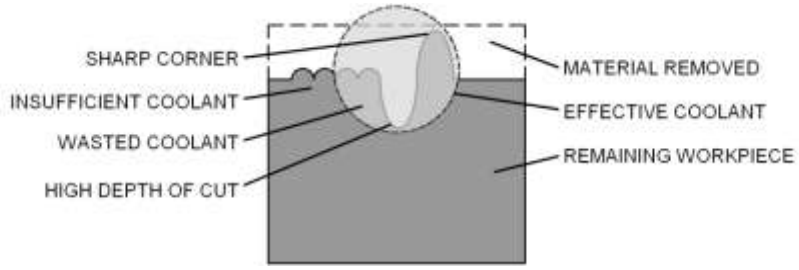

Figure 2.4: Arbitrary grinding profile cross-section illustrating regions at high-risk for damage.

2.3 Unconventional Application Methods

There are many methods that can be used to apply coolant and lubricant to an active grinding zone, though some are simpler and more cost-effective to implement. Described in this section is a selection of application methods either not possible or impractical to implement given the resources and scope of this research project.

2.3.1 Shoe Nozzle

A shoe nozzle is a large apparatus designed to closely fit against the grinding wheel circumference and physically guide fluid directly into the grinding zone, as seen in Figure 2.5. This setup is advantageous in that almost 100% of applied coolant enters the grinding zone; however, in order to maintain this level of efficiency the shoe must actively shrink to accommodate wheel wear. Because effectively all of the applied coolant enters the grinding zone, another difficulty is that the flow rate must be carefully metered: superfluous incompressible fluid will result in an elastic deflection of the system, causing surface and form error. Once the correct flow rate is determined for a particular setup, shoe nozzles can lower the grinding forces 40-60% and thereby decrease the required spindle power four to five fold [Ramesh *et al.* 200143].

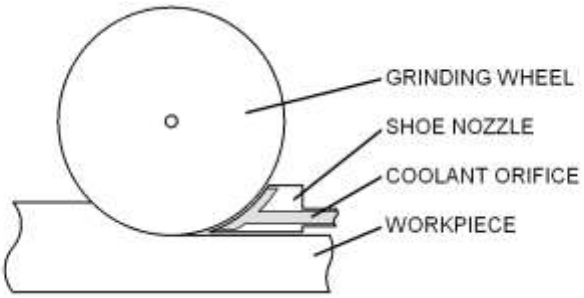

Figure 2.5: Typical shoe nozzle.

2.3.2 Floating Nozzle

Delivery of paste or chalk-like lubricant is done through the use of a floating nozzle. A floating nozzle consists of a grindeable nozzle endpiece that is positioned close to the grinding wheel surface, a reservoir of coolant, and a length of pipe that supplies the coolant directly to the wheel surface at low velocity, as shown schematically in Figure 2.6. The nozzle endpiece can be held in close proximity to the wheel through the use of a compression spring. Nimomiya *et al.* [2004] discussed the results of work that showed using a floating nozzle could reduce the wear of a vitrified CBN wheel by half while only using approximately 8% of the volume of coolant required by a traditional flooding method. However, grinding with a floating nozzle is limited to small depths of cut due to the lack of cooling effects—friction is reduced, but no heat or waste material is actively removed from the grinding zone. Also, without a wheel cleaning jet the paste can load the grinding wheel and eventually increase friction at the grinding zone, thus accelerating wheel wear over time.

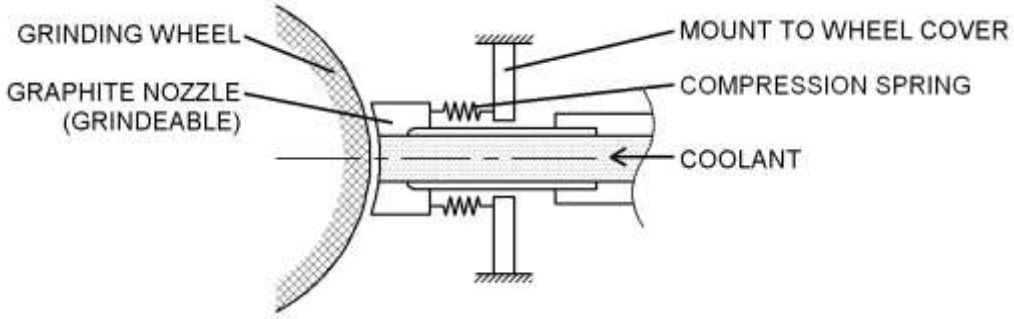

Figure 2.6: Simplified schematic of a typical floating nozzle.

2.3.3 Radial Jets

Tubes cast or machined radially into the grinding wheel can deliver coolant directly to the grinding zone by pumping it through the spindle assembly, as illustrated in Figure 2.7. With this method, no adjustments to the fluid supply are required as the wheel wears. Xu *et al.* [2001] discusses the promising results of their study conducted using electroplated CBN grinding wheels cast with internal radial coolant jets: fluid applied at 90 and 100 m/s through the hub assembly could maintain grinding zone temperatures at 100°C as compared to the conventionally cooled equivalent setup where temperatures rose to 800°C. The main difficulties with this method of coolant delivery lie in the production of an accurate hub-based coolant pumping system and the complex production of the wheels.

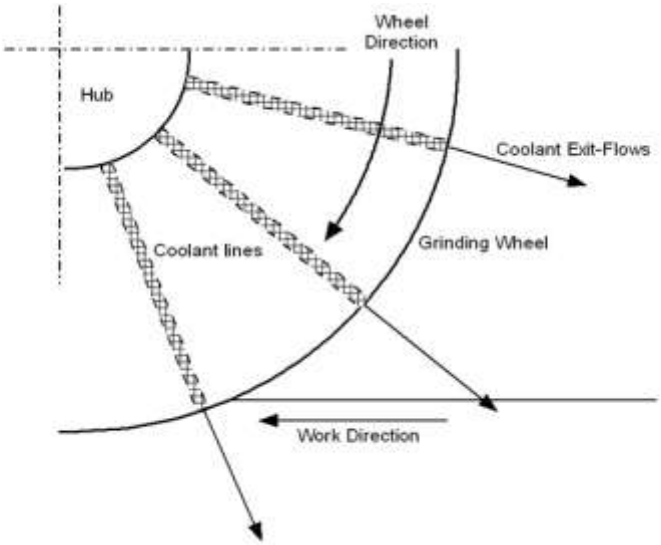

Figure 2.7: Cross-section of grinding wheel showing internal radial coolant jets [Irani *et al.* 2005].

2.3.4 Dual Fluid

Several experiments have been conducted to examine the effects of using two fluids to cool and lubricate the grinding zone. Yokogawa and Yokogawa [2001] describes a method used in cylindrical grinding wherein water was applied to the underside of the workpiece for bulk cooling and oil was applied to the grinding zone for lubrication and waste removal. The results showed that surface finish could be improved three fold over a single jet with mixed fluid at the same material removal rate, and be kept at a much

lower temperature. Irani [2006] performed similar work with creep-feed grinding that used a single lubricant jet directed at the grinding zone and two coherent water jets directed at the workpiece for cooling as shown in Figure 2.8. It was found that nearly all conditions in the grinding zone were improved: lower temperatures, higher material removal rates, and lower specific energy. The only difficulty in dual fluid application is the subsequent separation of the two fluids after grinding in order to recycle them. Because oil and water naturally separate, possible methods developed to re-separate used fluids included a centrifuge and a collecting apparatus to take advantage of discrete fluid layers in a holding tank.

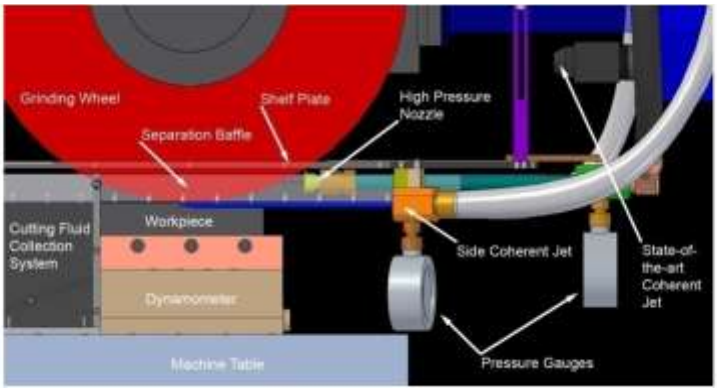

Figure 2.8: Apparatus for the separate application of lubricant and coolant [Irani 2006].

2.4 Conventional Application Methods

Several conventional methods used in industry to apply coolant to the grinding zone are described in this section; namely, a flood type jet, a coherent jet, and a high-pressure jet.

2.4.1 Flood Jet

Free jet flooding is the traditional method of applying coolant to a grinding zone because the nozzles required to generate a flooding jet of fluid are easily produced and can operate at a wide variety of pressures, fluid velocities, and physical orientations. A smooth workpiece surface finish is possible with flood jets at low flow rates as long as the dresser feed rate is high, that is, a sharper wheel surface is created that results in a more efficient cutting process [Webster *et al.*1995]. As with all forms of coolant there exists a critical flow rate below which the grinding zone is starved and the workpiece will burn [Webster 1999]. Within the plumbing preceding the nozzle, flood type systems

typically do not allow the coolant flow to achieve a uniform cross-sectional velocity distribution and, therefore, the resulting energized flow causes the jet stream to disperse and aerate rapidly after leaving the nozzle. As a result, flood type nozzles are typically rectangular in shape in an effort to spread the flow as widely as possible over the grinding profile before the jet becomes unusable; as seen in Figure 2.9 [Cui and Webster 1994]. Also, numerous studies have shown strong correlation between workpiece surface quality and the distance between the nozzle and the grinding zone: a closer nozzle yields a higher finish quality [Irani *et al.* 2005]. This phenomenon is understandable due to the rapid dispersion and aeration of the jet. As McCarthy and Molloy [1974] pointed out, this can be reduced via the use of a coolant with lower Reynold's number—achievable by refrigeration or increased oil content.

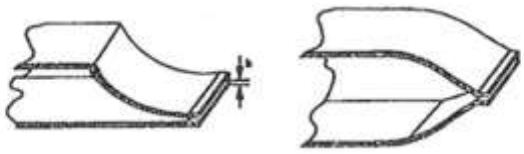

Figure 2.9: Two variations of a traditional rectangular flood-type nozzle [Cui and Webster 1994].

Orientation of a flood type nozzle is important because high flow rates and low velocities are typically used. The nozzle must be repeatedly adjusted during the grinding process as the wheel wears. Ideally, aiming the flow at or just above the grinding zone will cause the fluid to adhere to the wheel and be carried into the grinding zone [Webster 2008]. As discussed in Section 2.2.3, if the velocity of the coolant is between 60% and 100% of the peripheral speed of the wheel, the jet will have enough momentum to penetrate the air barrier; any slower than 60% and the coolant will either be rejected completely or accelerated by the wheel and cause excess drag on the spindle [Brinksmeier *et al.* 1999, Gviniashvili *et al.* 2003]. The critical wheel speed above which all applied coolant is rejected tangentially by centrifugal force is determined by the pressure of the air barrier, the coolant density, and the wheel radius [Gviniashvili *et al.* 2005].

2.4.2 Coherent Jet

Coherency—a unitless dimension defined by the ratio of jet width at some distance downstream over jet width at the aperture—represents one of the most promising fields of coolant delivery. The initial concept of applying a coherent fluid jet to machining originated in the 50's with Rouse *et al.* [1952] who had observed the jets created by fire-hose nozzles. The nozzle was later designed and tested by McCarthy and Molloy [1974], who determined numerous characteristics that were necessary to create a high-quality coherent jet: uniformly concave walls with a smooth surface, a smooth, rapid transition from inlet diameter to outlet diameter, and a small length-to-diameter ratio. The ideal shape of the internal contours was not known at that point and is still under scrutiny with computerized flow simulations today—"pleasing to the eye" remains the rule of thumb, but Figure 2.10 shows a current version of the coherent nozzle used in industry, including inlet and exit diameters, length of curvature, and length of a cylindrical exit region. The contraction ratio from inlet to outlet should be larger than 2:1 for best coherence, as shown experimentally by Webster [2007] and Morgan and Baines-Jones [2009]. A major difference between the modern coherent nozzle and the fire-hose nozzle initially examined lies in the region immediately following the aperture: after the concave region of contraction, fire hoses often have a short tubular span that acts as the final outlet. This tubular piece effectively ruins the coherence of the jet by creating laminar friction along the outside of the flow, slowing it, and causing the internal portion of the jet to curl away from the centerline and disperse the jet [Morgan and Baines-Jones 2009].

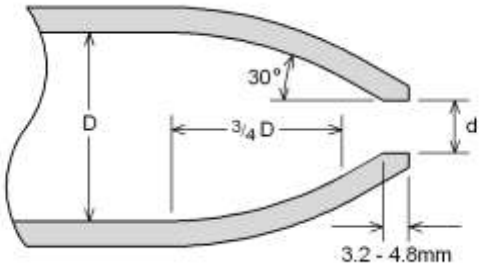

Figure 2.10: Suggested design parameters of coherent circular nozzle, including inlet and exit diameters (*D*, *d*).

For grinding, an effective coherent jet has a uniform core length that extends for as long as possible downstream in order to apply coolant to the grinding zone consistently regardless of nozzle placement. Coherency relies on velocity distribution that is as uniform as possible. This type of uniform flow is achieved through the exclusive use of straight or gently curved sections of pipe before the nozzle as discussed in the development of flow above [Webster 1999]. Morgan and Baines-Jones [2009] performed hot-wire anemometry tests on several nozzles to compare the jet velocities of a typical flood nozzle to a coherent nozzle. The results reveal that the uniform velocity distribution across the flow of a coherent jet yields a central peak velocity for a longer distance and within a larger proportion of the jet profile than a typical flood nozzle (Figure 2.11). A single circular exit to the nozzle is not the only shape that can create a coherent jet: Webster [2007] created a multiple orifice nozzle that yielded a series of parallel semi-coherent jets, but the design was bulky and complex to implement. Through the work of Steffen [2004], a coherent jet was developed for the Dalhousie grinding lab and a 30-60% critical specific material removal rate improvement was reported, encouraging further research into the use of coherent coolant jets.

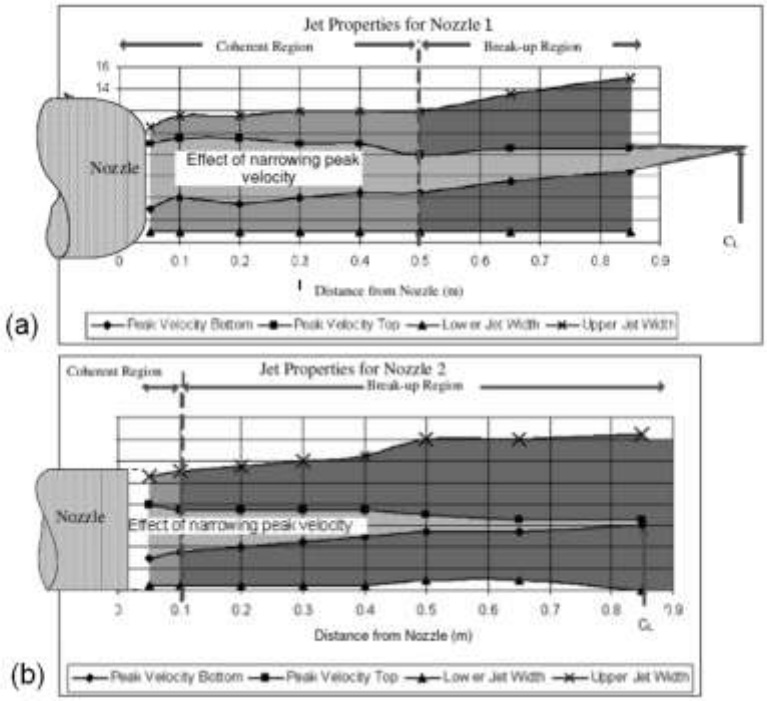

Figure 2.11: Jet velocity profiles for (a) a coherent nozzle and (b) a flood-type nozzle. [Morgan and Baines-Jones 2009]

2.4.3 High-Pressure Jet

Coolant applied at high-pressures and low flow rates can be superior to other forms of coolant for several reasons, but is also a risk: excessive pressure risks breaking down the grinding wheel itself. An example of excessive pressure would be that of water jet cutters that use a stream of high-pressure fluid to directly cut metal using fluid pressures in the 100-300 MPa range. The miniscule diameter of these jets, however, dramatically increases their penetrating power over comparable pressures for coolant jets [Li *et al.* 2002].

Hartlen *et al.* [2008] found by measuring the form error of a ground workpiece that a high-pressure jet resulted in less wheel wear—and subsequently less form error—than flood and coherent jets applied under the same grinding conditions. These results are shown in Figure 2.12. As discussed in Section 2.2.1, the useful flow of a coolant jet can be improved if high-pressure forces more fluid into pores within the grinding wheel. In addition to this benefit, a high-pressure jet also performs the same task as a wheel cleaning jet: clearing the wheel of debris and lengthening the life of the tool.

Experiments with high-pressure coolant in turning have corroborated this phenomenon. Nandy and Paul [2008] discovered that with a coolant pressure of 10 MPa they could consistently show tool life lengthened 3.5 times over flood cooling. Ezugwu [2005] was able to show 7 fold improvement in tool life, attributing the dramatic results to a reduced heat partition passing to the tool—the heat was instead being flushed away by the coolant. Moving coolant rapidly through the cutting zone, however, reduces the amount of fluid present and available to perform work at any given moment, requiring that—for grinding—the flow rate be low and the dresser feed rate be increased [Webster *et al.* 1995]. Despite this requirement, other experiments have shown that with coolant pressure as high as 380 MPa, grinding forces can be improved 25% and surface roughness improved 50% [Cameron 2010].

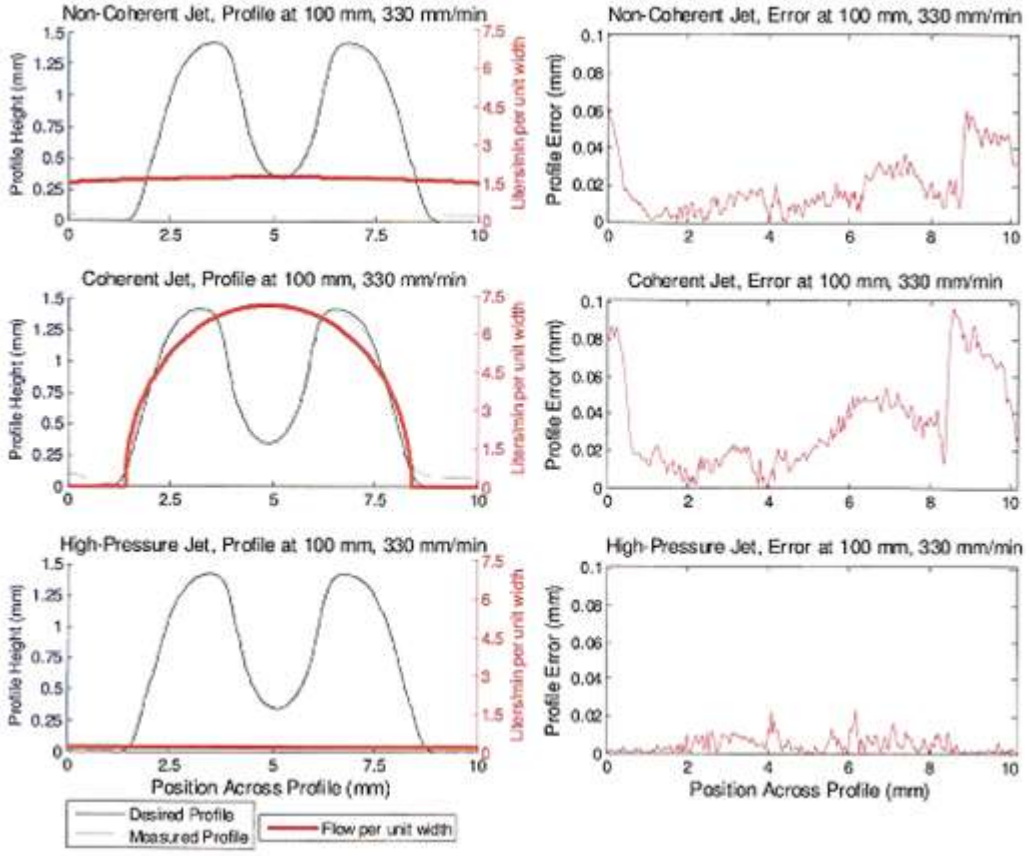

Figure 2.12: Workpiece form error with flood, coherent and high-pressure coolant jets [Hartlen *et al.* 2008].

2.5 Coherent Jet Nozzle Design

Efforts are continuously being made to create nozzles that will improve the efficiency and predictability of free jets. Several design parameters have been established for the internal geometry of the nozzle if a low-divergence coherent jet is desired. These parameters include the shape of the cross-section and aspect ratio of the aperture as well as the specific contours of the internal nozzle geometry and critical exit region. Various reasons for the ability of the design parameters to influence the emerging jet have been cited based on extensive experimental data of jet velocity profiles. This section will highlight such studies, and will go on to discuss a variety of parameters that control the behavior of the jet with respect to grinding applications, such as fluid flow within the plumbing and placement of the nozzle with respect to the grinding zone.

2.5.1 Nozzle Design Parameters

In large part, nozzles designed to create coherent jets have been circular in cross-section and, therefore, yield circular jets. Other shapes have been tested – though only superficially, as summarized by Steffen [2004]. Quinn [1981] and Quinn [2006], for example, used hot wire anemometry to measure the velocity profile of jets emerging from cruciform apertures in a flat plate. Iyogun and Birouk [2009] performed similar analyses using a Doppler velocimeter, but tested a variety of triangular, rectangular, elliptical, and circular nozzle apertures. Numerous other research projects have dealt with apertures of these shapes, such as the work of Azad *et al.* [2012] and Ghassemieh *et al.* [2006]; however, none of the nozzles designed utilized complex internal contouring. Cui and Webster [1994] cut apertures of several shapes into a flat plate and then rounded the internal edges, but no specific reason was given for the choice of fillet radius. In the work of Zeng [2011], cylindrical tubes with a variety of collared and beveled apertures were tested, all resulting in high air entrainment and highly divergent jets. Other recent analyses of jet velocities performed with hot-wire anemometry and Doppler velocimetry by Quinn [2007] and Iyogun and Birouk [2009], respectively, show a clear trend of higher ambient-air entrainment and faster velocity decay in nozzles with large aspect ratio elliptical or rectangular apertures. This trend has been confirmed in numerous studies, such as with rectangular nozzles used in grinding applications designed by

Webster *et al.* [1995] or the variety of elliptical nozzles tested by Husain and Hussain [1992].

Some of the earliest work on nozzle internal geometry performed by McCarthy and Molloy [1974] and Rouse *et al.* [1952] found that a continuously-contoured, smooth-walled concave nozzle with a region of rapidly increasing contraction near the exit could create a coherent circular jet of water at Reynold's values well beyond the limit of turbulence. These researchers did not, however, specify constraints on the curvature or smoothness; rather, they admitted that a contour shaped to please the eye could perform satisfactorily. Hoyt and Taylor [1985] tested a variety of simple cone-shaped nozzles using high-speed macrophotography and found a direct correlation between interior surface smoothness and achievable coherency, thus verifying the qualitative work previously set out. Webster *et al.* [1995] later developed a nozzle with a rectangular aperture that utilized the converging concave geometry of the Rouse nozzle. Dispersion of the jet was found to increase 27% if a chamfer was applied to the outer lip of the aperture, thus suggesting that a sharp exit region may contribute to low divergence in jets. This conclusion is supported by extensive hot-wire anemometry tests conducted by Quinn [1981], Quinn and Marsters [1985], Quinn and Militzer [1989], and Quinn [2006]. Webster [1999] then went on to demonstrate that a higher contraction ratio – that is, the ratio of nozzle inlet to outlet diameter – proved more beneficial to creating a coherent jet. While the behavior of jets has been thoroughly studied, thus far in this field little improvement has been made to the purely qualitative "by eye" approach of nozzle contouring pioneered by McCarthy and Rouse.

2.5.2 Visualization of Flow within the Nozzle

There have been numerous attempts to analyze the fluid flow within coolant nozzles, both experimentally and analytically. Quinn [1981] and Quinn and Marsters [1985] hypothesized that the layer of fluid closest to the wall remained mostly laminar in nozzles with a contoured geometry – a similar conclusion to that of the earlier work by McCarthy and Molloy [1974] and Rouse *et al.* [1952]. In contrast, the photographic study conducted by Hoyt and Taylor [1985] asserted that the laminar flow of fluid in a long,

straight pipe is lost in the nozzle due to the high contraction ratio and then relaminarizes in the initial region of the free jet. Most recently, a study conducted by St-Pierre *et al.* [2012] used jet divergence angles obtained from photographs of coherent jets at various pressures to create a computer simulation that was used to deduce the general behavior of the fluid within the nozzle. The simulation was able to predict jet coherency to an accuracy of ±2% when applied to coherent circular nozzles of the Rouse design. In 1987, Ho and Gutmark [1987] observed the phenomenon of axis switching in jets emerging from elliptical apertures – that is, spreading of the jet first in the plane of the minor axis of the ellipse, and then at some point downstream reversing to the plane of the major axis of the ellipse. Ghassemieh *et al.* [2006] and Husain and Hussain [1992] also observed axis switching in later experiments. It is generally accepted that uneven jet divergence is caused by an imbalance between vortices induced in the major and minor axis planes. Regardless of the behavior of the jet near the aperture, it has been noted by Quinn [1995] and Azad *et al.* [2012] that all jets eventually disperse in all directions to form a roughly circular cross-section.

Using analytical approaches and computer modeling, other studies have attempted to describe the effects various geometric nozzle parameters have on fluid behavior. Shen *et al.* [2011] analyzed high pressure tubular exit nozzles and found that, as with coherent jets, the nozzle with the most rapid transition from inlet to outlet diameters provided the smoothest flow (Figure 2.13). Alberdi *et al.* [2011] analyzed a typical rectangular Webster flood nozzle at low velocity; Figure 2.14 shows the results of their work.

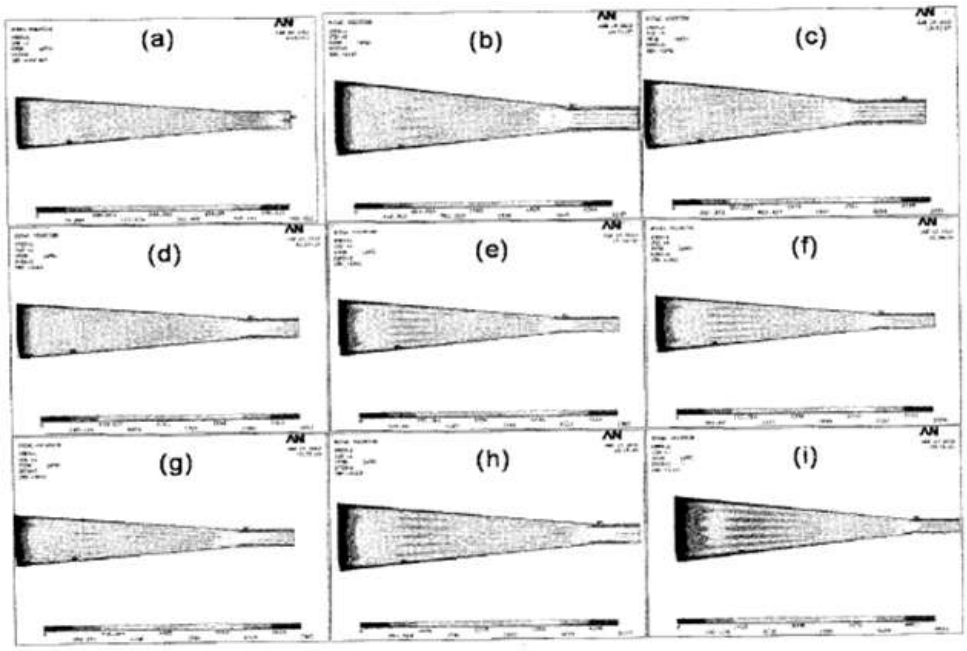

Figure 2.13: CFD analysis performed within various nozzles [Shen *et al.* 2011].

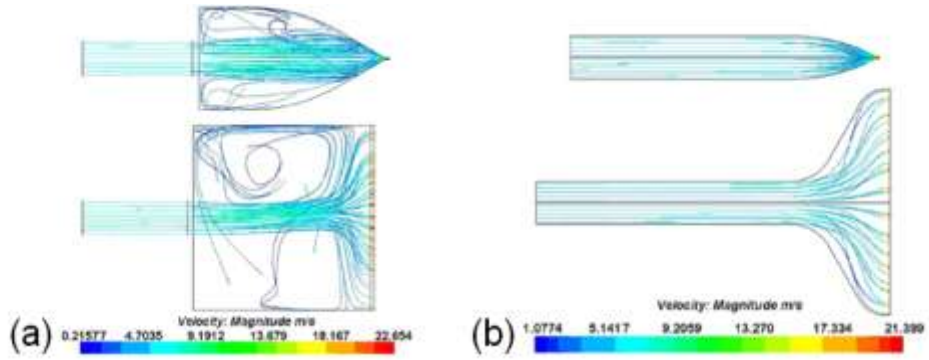

Figure 2.14: CFD analysis of (a) a typical and (b) improved Webster nozzle [Alberdi *et al.* 2011].

Large regions of turbulence above, below, and to the sides of the central flow cause a highly non-uniform velocity distribution at the nozzle exit. In an attempt to remedy this inefficient spreading of flow into corners, they designed an improved Webster nozzle that eliminated the corners where eddies could form, resulting in a much more uniform flow towards the aperture, as seen in Figure 2.14. Based on simplified computerized flow dynamics (CFD) models of highly complex and rapidly changing fluid dynamics phenomena, analytical models such as those discussed here must still be tested experimentally in order to verify their potential.

In addition to virtually testing nozzle designs, there has been a recent interest in computerizing the selection of coolant application parameters. Some of these methods are spreadsheet-based, relying on the user to collect data that relate grinding forces, power, coolant properties, tool wear, and surface finish in order to recommend the ideal method and parameters of coolant delivery [Axinte and Chiffre 2008]. Another method, developed by Cai and Morgan [2008], uses an idealized coherent nozzle to recommend flow rate and fluid velocity based on properties of the grinding wheel, chosen coolant, and limitations of the chosen pump.

2.5.3 Fluid Flow

Generally occupying 120% of the physical space of the grinding machine itself and drawing 7-17% of the budget, the fluid storage and delivery apparatus should not be treated as an afterthought [Alberdi *et al*. [2011], Ramesh *et al*. [2004]. The plumbing used to direct coolant towards the grinding zone is a critical portion of the cooling process. Turbulence in a column of moving fluid leads to unpredictable velocities and flow patterns [Webster 1999]. For grinding, where a uniform application of coolant across the grinding zone is ideal, an unpredictably dispersed flow is therefore not advantageous. In order to create an approximately uniform laminar cross-sectional velocity profile within a pipe, it has been determined in numerous experiments that a straight section of pipe 48 times the inner diameter of the pipe is required. If space is a limiting factor, however, a straight length of pipe 15 times the inner diameter may be used in conjunction with a flow conditioner [Cui and Webster 1994]. A flow conditioner is essentially a honeycomb of short, small diameter parallel pipes placed in the coolant flow to create uniformly laminar motion (Figure 2.15). Webster and Cui [1995] experimented with various flow conditioner designs and concluded that a conditioner no longer than 2 cm would smooth the flow and not cause sufficient drag to inhibit laminarization. Also, they showed that placing a flow conditioner in a fully developed flow would actually increase turbulence.

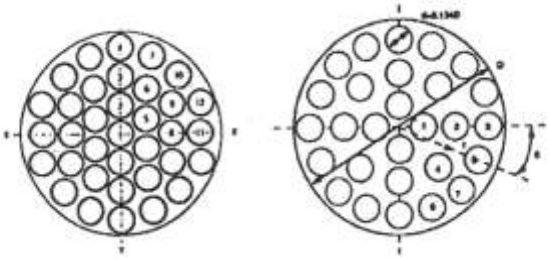

Figure 2.15: Various styles of flow conditioners [Cui and Webster 1994].

As any fluid jet emerges from a nozzle it immediately begins to disperse. McCarthy and Molloy [1974] outlined attempts to analytically predict the region of breakup based on surface tension, inertia, and the Reynold's number of the fluid, revealing that more viscous fluids moving at higher velocities remained in a coherent jet for a longer distance regardless of the nozzle used. This fact corroborated work done earlier by Rouse *et al*. [1952] that predicted the origin of jet breakup: microscopic surface disturbances in the flow at the nozzle exit that grow exponentially along the length of the jet. These disturbances proliferate until they reach a size scale that rivals the jet radius, at which point they have enough orthogonal surface area for air friction to slow individual globules and disperse the stream. A more contemporary explanation for jet breakup depends on the principle of conservation of momentum: as the velocity of a jet of fluid slows, the jet must entrain mass from the surrounding medium in order to maintain the same momentum, thus causing the cross-sectional area of the jet to increase and the fluid distribution to disperse. Understandably, a jet that maintains a more uniform cross-section over a longer distance is more favorable for use in grinding because the distance between the nozzle and grinding zone is not critical.

2.5.4 Jet Placement

Numerous studies have been conducted into the most effective placement of a coherent jet nozzle in order to obtain the best possible surface finish. Three variables commonly tested are illustrated in Figure 2.16. Irani *et al.* [2005] explored various impact angles—the angle between the work surface and the impinging jet—and stand-off distances—the distance between the nozzle aperture and the active grinding zone. Hartlen *et al.* [2008] also tested the placement of the jet vertically with respect to the peripheral region of the wheel in contact with the active grinding zone. Steffen [2004] methodically tested the

effects of vertical nozzle placement, stand-off distance, and impact angle. All studies are in agreement that the nozzle position plays an insignificant role in the ultimate surface finish as long as sufficient coolant enters the grinding zone, but that a stand-off distance as small as possible will ensure the most uniform, high-velocity core region of the jet is being utilized.

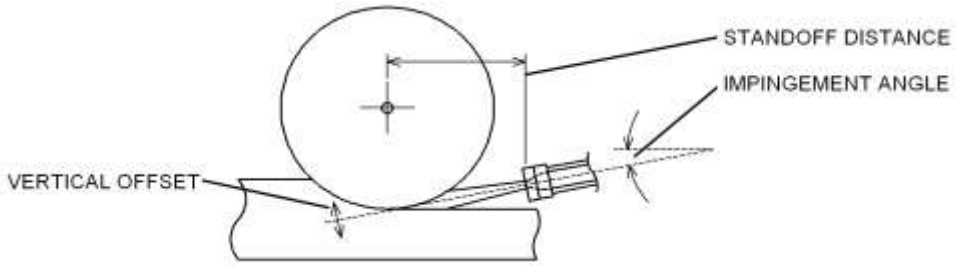

Figure 2.16: Geometric nozzle positioning variables.

2.6 Summary

Cutting fluids are a critical aspect of the grinding process; encouraging cutting efficiency and material removal, reducing the potentially damaging effects of friction, and removing waste material with as little excess of fluid as possible. During the application of fluid to the active grinding zone, the boiling limit of the fluid, the concept of useful flow, and the inhibitory layer of air entrained around the grinding wheel must be taken into consideration. These obstacles can be overcome by choosing an appropriate delivery method, such as one of those discussed in this chapter. For the purposes of this research, a nozzle capable of generating a coherent jet of fluid was chosen to be studied exclusively; a coherent jet is the easiest to aim consistently at the grinding zone as the wheel wears, applies the most uniform distribution of fluid to the grinding profile, and is the least sensitive with regard to the stand-off distance between grinding zone and nozzle. The fluid flow within the plumbing system of the grinding machine must also be regulated in order to generate a uniform velocity distribution across the profile; a fundamental requirement of a high-quality coherent nozzle. Therefore, when looking at the combination of these variables, the possible increases in cutting effectiveness make the study of an elliptical-shaped coherent jet worthwhile for profiled creep-feed grinding.

CHAPTER 3 NOZZLE STUDIES

The remainder of this thesis will deal with experimental work conducted with the following main objectives in mind:

- Develop a cost-effective fabrication method to create complex reproducible nozzles.
- Determine the effects on jet behavior of a variety of internal nozzle geometric parameters, with an eye toward creating low divergence elliptical jets.
- Compare the performance of a low divergence elliptical jet to that of a circular jet in terms of the results of a creep-feed grinding process.

Chapter 3 will detail the development, design, and fabrication of elliptical nozzles, followed by Chapter 4 and Chapter 5, collectively, a description of the experimental grinding work conducted to verify the novel jet performance with respect to grinding.

3.1 Nozzle Fabrication

The first goal of this research—to create a low-divergence elliptical jet—depended first on the development of a method to generate numerous unique nozzles in a cost-effective and rapid manner. An experimental focus was used in this work to increase efficiency of the design process. While computer simulations allow unparalleled freedom in terms of permissible variables, any simulations performed would have required experimental corroboration; therefore, a method to design and fabricate nozzles quickly and cost-effectively was the top priority. Where traditional hand and CNC machining are often time and cost-intensive, a "rapid-prototype (RP) printer" can fabricate pieces in a fraction of the time and—often—for a fraction of the cost. Therefore, a fused-deposition modeler utilizing acrylonitrile butadiene styrene (ABS plastic) was chosen to fabricate the array of nozzles to be tested. The following section details the process of manufacturing nozzles using this novel technique, from internal geometry generation to three-dimensional extrapolation and RP printing.

3.1.1 Rapid-Prototyping Feasibility

Several initial proof-of-concept tests were performed to verify that the RP material would withstand experimental testing and could be satisfactorily substituted for an aluminum nozzle currently used for the grinding machine. Using an aluminum nozzle of circular cross-section and aperture diameter of 8 mm, an RP replica was created with an identical internal geometry. A cross-section of this geometry is shown in Figure 3.1.

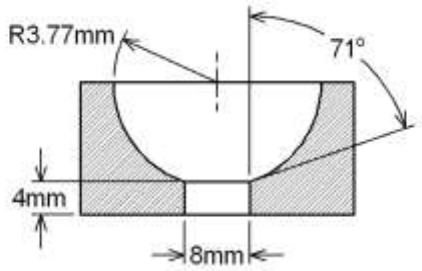

Figure 3.1: Cross-section of circular stock aluminum nozzle used to create an identical RP nozzle.

Fluid was applied to both the RP nozzle and the aluminum nozzle under identical flow rate conditions—that is, 37.9 LPM—and the resultant jet divergence angle and jet width were measured over time using image analysis. Figure 3.2 provides examples of images captured of the jet issuing from the aluminum nozzle (a) and the RP printed nozzle (b).

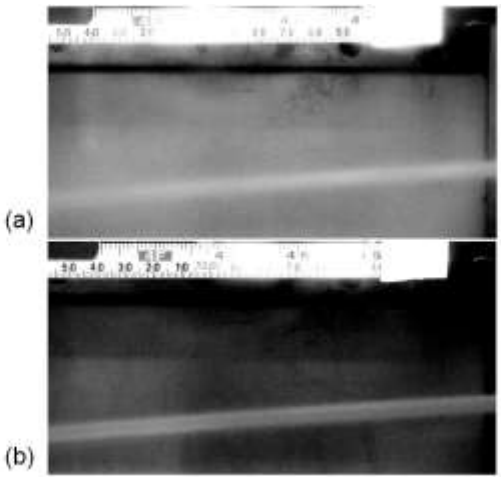

Figure 3.2: Sample of RP nozzle feasibility testing; jets issuing from (a) aluminum nozzle and (b) RP nozzle under the same conditions: flow rate 37.9 LPM.

Results of this feasibility testing indicated that, within the measurement capabilities, an RP printed nozzle with an internal geometry matching that of an existing aluminum nozzle could produce an identical jet and remain stable without showing any signs of wear in excess of 90 minutes of continuous use. Despite differences in inner surface roughness and material hardness between the smooth aluminum nozzle and the layered RP nozzle, performance remained stable throughout the 90 minute test period; there was an insignificant 0.09% total migration in measured values. These results are shown in Figure 3.3: at each data point, three photographs were obtained, the jet characteristics noted and averaged, and from these averages standard deviations were calculated.

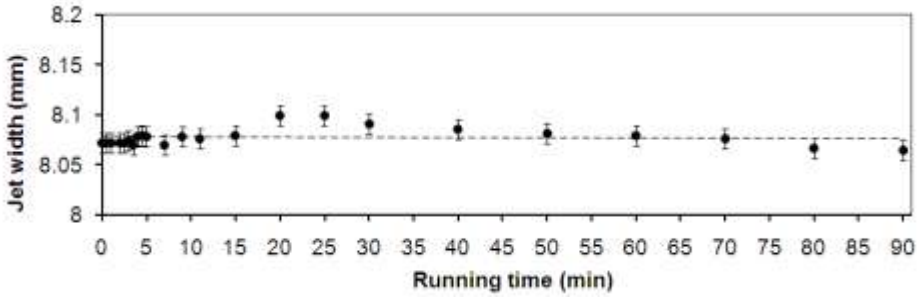

Figure 3.3: Results of RP nozzle durability testing with one standard deviation of uncertainty.

Extended use—in excess of 8 hours—at pressures occasionally exceeding 4 MPa also had no detectable influence on the inner surface of the RP nozzle beyond a slight surface discoloration, as illustrated in Figure 3.4; note, two different nozzles are illustrated in Figure 3.4 (a) and Figure 3.4 (b). If the slow migration detected during the 90 minute test period is assumed to be roughly linear, the total change in jet width would be no more than 0.48%, or 0.038 mm, for the entire span of experiments. Assuming a linear trend, 1 mm change in jet width at the grinding zone would be achieved in 208 hours of high pressure cutting fluid usage.

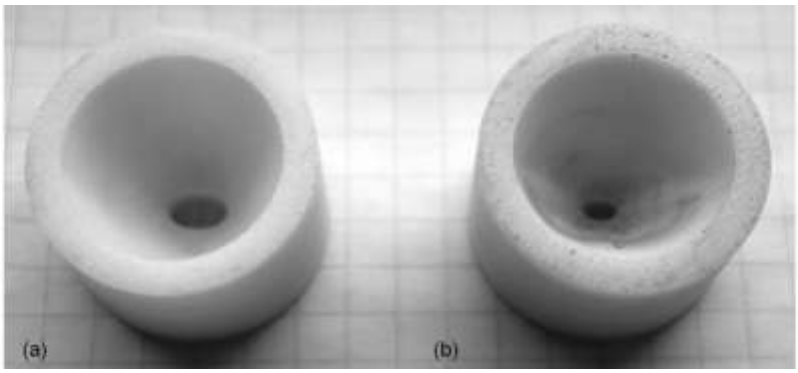

Figure 3.4: Internal surface of two RP nozzles (a) before and (b) after extended use.

Given the promising results of these proof-of-concept tests, this novel nozzle fabrication approach was deemed satisfactory to pursue further research into the effects of internal geometry on jet behavior.

3.2 Internal Contour Overview

Elliptical nozzles developed in historical studies have tended to use stock circular or rectangular tubing in advance of the nozzle, and standard milling and boring operations to form the internal contouring of the nozzle. Discontinuities yielded by a rectangular pipe butted directly to an elliptical nozzle, for example, create regions of high turbulence and lower the possible coherency of any jet issuing from the aperture.

Within the nozzle itself, another aspect of contouring has also been historically overlooked. Using a radially or linearly symmetric internal contour leading up to an aperture of non-circular or non-square shape creates asymmetrical eddies and turbulent regions; an effect exaggerated for larger aspect ratio apertures. This phenomenon is illustrated for several industry-standard configuration nozzles in the simplified schematic, Figure 3.5. Radially symmetric vortices effectively cancel each other out, yielding low divergence angles and relatively low mixing of the jet, illustrated in Figure 3.5 (a). As shown in Figure 3.5 (b), the dissimilar vortices induced in the minor and major axes of a non-circular aperture contribute to high jet divergence angles, high jet dispersion within its surrounding medium, and exaggerate the phenomenon known as axis switching.

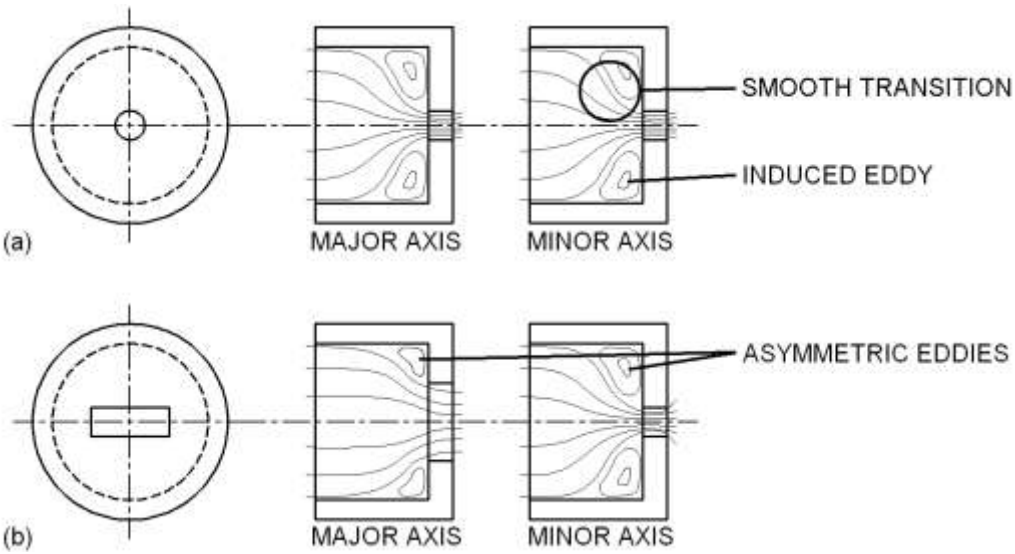

Figure 3.5: Axial vortices induced in (a) radially symmetric and (b) asymmetric nozzle geometries.

Axis switching is the process wherein the major axis of a non-circular jet alternates between two orientations—passing through a circular phase—due to competition between the elasticity of surface tension and the inertia of the mass flow. A high-speed image captured of this process is illustrated in Figure 3.6 [Amini and Dolatabadi 2012].

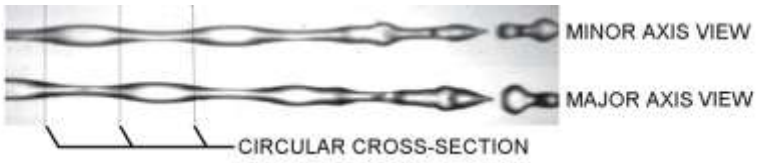

Figure 3.6: Example of axis switching in a free jet, as seen from simultaneous minor and major axis views [Amini and Dolatabadi 2012].

In order to carefully control the radial asymmetry of nozzles developed for this research, a set of radially-oriented "profile curves" were blended together to define the internal contours that connected the circular pre-nozzle tubing to the elliptical final aperture—that is, the nozzle—in a smooth and continuous fashion with measurable geometric attributes. The profile curves defining the major and minor axes of a sample nozzle are shown in Figure 3.7. The creation and modification of these profile curves are discussed in the following Section.

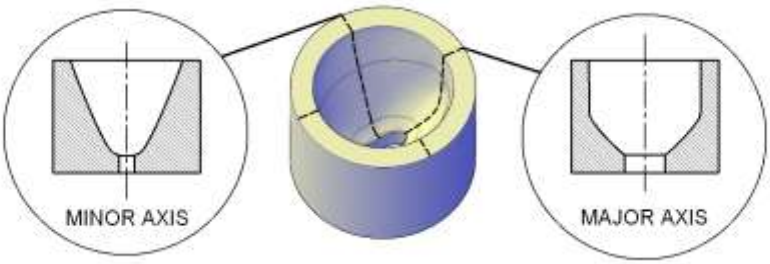

Figure 3.7: Cross-sections of a sample nozzle revealing the major and minor axis profile curves.

3.3 Generation of Internal Contours

The internal contours of the nozzles were developed through application of a novel approach to grinding nozzle design. A fourth-order Bezier polynomial curve was chosen to represent the various independent cross-sectional profile curves, as detailed in Section 3.3.1. Section 3.3.2 goes on to discuss the specific characteristics of the curves chosen to be investigated. Constraints inherent and inflicted upon these chosen characteristics are detailed in Section 3.3.3. Following this discussion of possible curves, Section 3.3.4 will describe the process used to automate production of predictable Bezier curves based on a set of user-input parameters. Finally, Section 3.3.5 will highlight extrapolation of the curves into a three-dimensional solid capable of being printed by a rapid-prototyping machine.

3.3.1 Validation of Bezier Curve Use

Fourth-order Bezier curves were selected to represent the radial profiles for several reasons: there exist definable, unique, geometrical attributes for every Bezier curve; adjusting curvature is accomplished by manipulating three control points and two end points; and finally, freedom to shape the curve is reduced with lower-order polynomials while the risk of concavity "rippling" increases for higher-order polynomials. For these reasons, a fourth-order Bezier curve proves to be advantageous over applicable polynomials as parabolic, cubic, or even a higher-order Bezier curve.

A general Bezier curve *B(t)* is defined by:

$$B(t) = \sum_{i=0}^{n} \frac{n!}{i!(n-i)!} t^i (1-t)^i P_i \qquad (3.1)$$
$$0 \le t \le 1$$

where n is the degree of the curve, t is the step parameter, P_i are the control points and *B(t)* is an arbitrary point on the curve. Through manual modification of the various control points, geometric attributes such as curvature sharpness, concavity, slope, arc length, and overall "smoothness" can be controlled and monitored.

3.3.2 Defining Characteristics of a Bezier Curve

In order to sample across a spectrum of nozzle contours and extrapolate resultant trends in jet behavior, three geometric properties of the nozzle interior were selected: aperture aspect ratio, nozzle exit angle and curve arc length.

Setting the input and output aperture aspect ratios was accomplished by modifying the start and end points of the profile curves. All nozzles were required to have a circular input aperture with a 25.4 mm diameter—in order to exactly match the coolant infeed pipe—thus fixing the start point of all curves. The output apertures used were elliptical and of a uniform area equivalent to a 6 mm diameter circle, but the various designs employed different aspect ratios. The aspect ratio of an ellipse is defined as *a/b*, where *a* is the semi-major axis and *b* is the semi-minor axis. The smallest aperture aspect ratio tested in this research was 1.00—corresponding to a circle—while the largest aspect ratio was 2.45. Figure 3.8 compares these various aperture sizes.

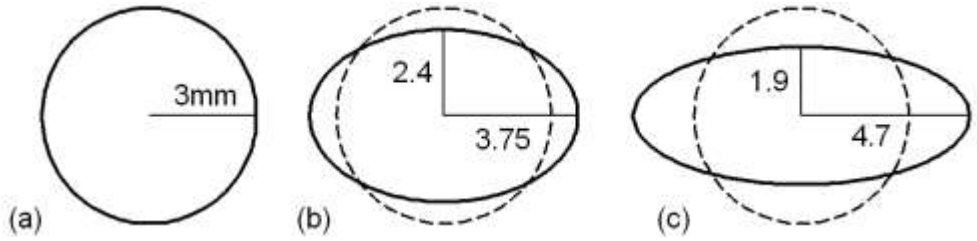

Figure 3.8: Various aperture aspect ratios tested, all measurements in millimeters; (a) 1.00, (b) 1.56, (c), 2.45.

Figure 3.9 shows the geometric attributes of a fourth order Bezier curve. Radial length r of the exit aperture with respect to the Bezier curve can be a true circular radius, a semi-major axis, or a semi-minor axis. Exit angle α is defined as the angle between the longitudinal streamwise axis of the nozzle and the region of the nozzle curvature immediately next to the aperture. In order to facilitate an accurate angular measurement of α, the Bezier curve terminates before it reaches the elliptical aperture: a 1 mm long line segment, oriented at the desired exit angle, connects this floating end point of the Bezier curve to the aperture. Finally, Figure 3.9 shows the locations of the three mid-span control points; the final two control points are the end points.

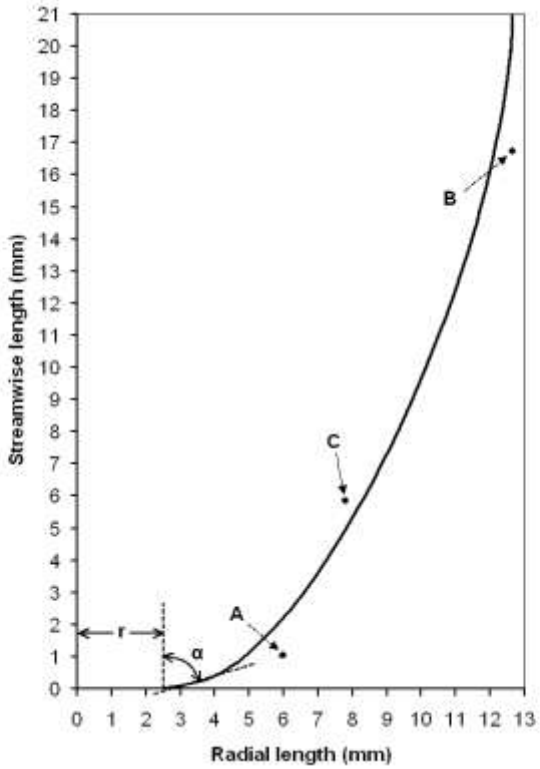

Figure 3.9: Geometric properties of a sample fourth-order Bezier curve.

Given only aperture aspect ratio and an exit angle, several Bezier curves exist that can satisfy the parameters. Therefore, an additional parameter was required to ensure that only one unique curve could exist for a desired aperture aspect ratio or exit angle. Arc length was selected as this final design parameter because it allows for the indirect manipulation of the curvature. Illustrated in Figure 3.9 is a sample fourth-order Bezier curve with its three control points A, B, and C highlighted; the final two control points, that is, the start and end points, lie on the curve itself. The calculated placement of A, B, and C within a set of imposed constraints will determine the arc length of the curve, as will be discussed further in Section 3.3.3. The approximate arc length *S* of a Bezier curve is found using the linear approximation:

$$S = \sum_{t=1}^{n} \sqrt{(x_t - x_{t-1})^2 + (y_t - y_{t-1})^2} \qquad (3.2)$$

where *t* is the step parameter, and *x* and *y* are the coordinates of the curve.

Nozzles used in this research were designed so that the curve with the shortest arc length was aligned in the direction of the minor or major axis plane of the aperture, while the curve with the longest arc length was aligned in the direction of the opposite axis plane. This geometry is illustrated on a cutaway model of a sample nozzle in Figure 3.10. The arc lengths of the various profile curves oriented between these two extremes is varied in a linear fashion, depending directly on the orientation of the plane in which the curve lies with respect to the major and minor axis; orienting the various profile curves is discussed in more detail in Section 3.3.5. Using this linear progression of arc lengths allowed for control of the global curvature of individual profile curves and assured that the global curvature changed in a predictable fashion around the circumference of each nozzle. The difference between the longest and shortest arc length is referred to as the "arc length range", and it is this value that will be used in discussion of all experimental work to follow.

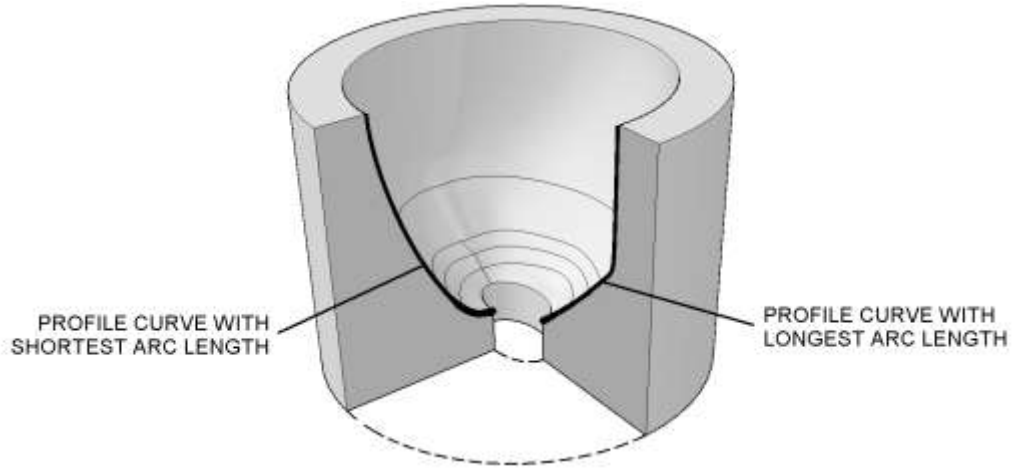

Figure 3.10: Cutaway of a sample nozzle, showing the profile curves with the shortest and longest arc length.

3.3.3 Constraints on Design Parameters

In order to test the effects of the three design parameters—aperture aspect ratio, exit angle, and arc length—in isolation, each parameter was adjusted over its own range of possible values as bounded by both inherent and imposed constraints.

Inherent constraints were present in the form of experimental apparatus dimensions: given the tubing diameter of the coolant plumbing system, there exists a limit to the possible aperture aspect ratio and dimensions. This fact taken in conjunction with the equipped coolant pump dictated that only fluid pressures between 0 and 8.3 MPa (1200 PSI) were possible to test. Inherent constraints were also imposed by the characteristics of the desired internal contours, such as continuous concavity and a smooth transition from inlet to outlet apertures. For an elliptical aperture of aspect ratio 1.56 and a semi-major axis of 3.75 mm—the dimensions chosen for a majority of this research—the exit angle, for example, could only vary between 40 and 80° in order to ensure the curvature of the Bezier curve remain concave. Another example is illustrated in Figure 3.11 when the aperture and exit angle are held constant; the two extreme values of possible arc length are shown, bounding the envelope of possible curves testable by varying only arc length. Within the scope of this research, it was feasible to test only the extremes and midpoint of this possible range—and indeed for all three chosen design parameters—in order to identify general trends in jet behavior.

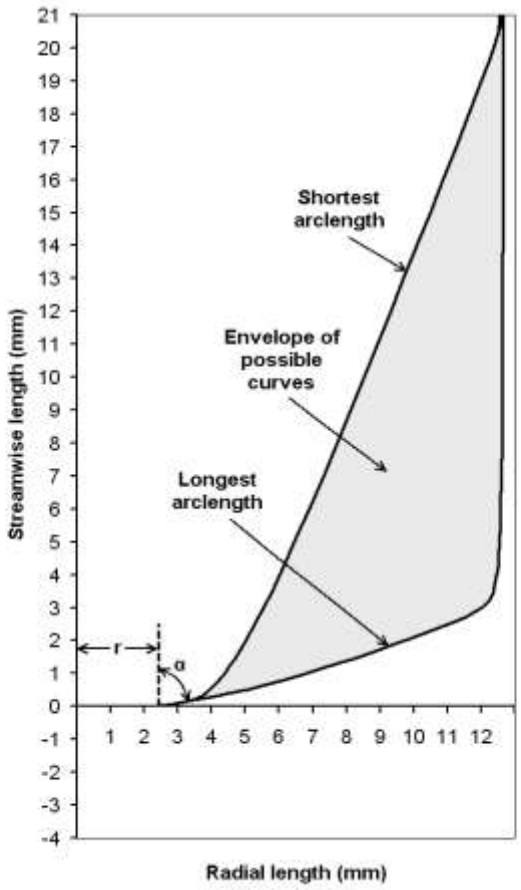

Figure 3.11: Envelope of testable curves when aperture aspect ratio and exit angle are held constant.

Due to this large domain of entirely valid, testable curves, a set of graphical constraints was placed on the possible locations of the three Bezier control points A, B and C illustrated in Figure 3.9. As shown in Figure 3.12, control point A lies on a line extending from the linear exit region and passing through the end point D; that is, the end point of curve connecting it to the 1 mm long straight line segment defining the aperture exit angle. With the domain of point A bounded graphically on the right by 13 mm and on the left by a 2 mm padding added to the *x*-value of point D, the slope of the linear exit region and the initial slope of the curve are equal, thus forcing a smooth and continuous transition from curve to exit. Control point B lies on a vertical line that extends through end point E between $y=-4$ mm and 20 mm. This constraint on control point B ensures a similar smooth, continuous transition between the plumbing of the coolant system and the nozzle. Finally, control point C lies along the internal angle bisector of the lines

corresponding to the locus of possible control points A and B between x=5.50 mm and 9.45 mm. The domains of these constraints correspond to the limits of an upwardly-concave curve and provide an effective way to adjust the arc length of the curve while leaving all other design attributes intact. Combined, these inherent and imposed constraints ensure that only a single unique Bezier curve can satisfy a set of user-defined geometric parameters.

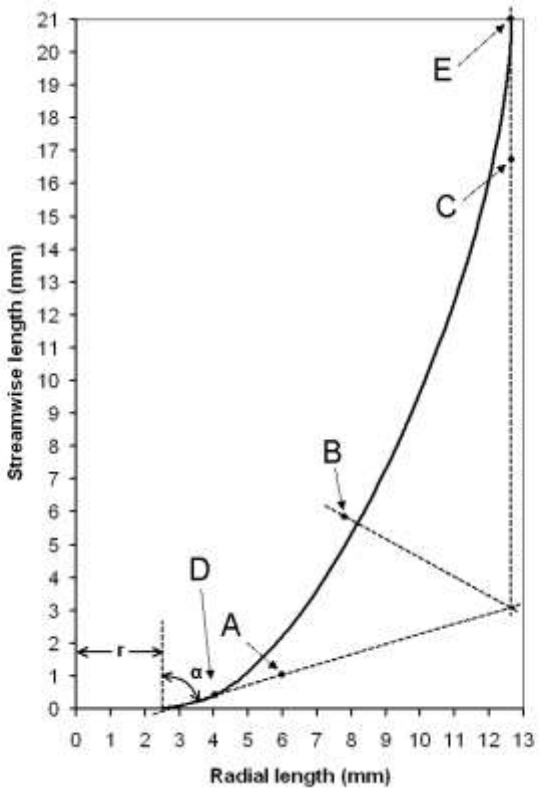

Figure 3.12: Sample profile curve with control points defined along the imposed constraint lines.

3.3.4 Curve Generation

An algorithm was developed in MATLAB to create Bezier curves based on a user-defined exit angle, arc length, and aperture aspect ratio. The program was designed to iterate through every possible combination of locations for the three control points within the constraints discussed in Section 3.3.3 and illustrated in Figure 3.12. An exhaustive optimization routine was then employed to minimize the discrepancy between a user-desired arc length $S_{desired}$ and the calculated arc length $S_{calculated}$:

$$\min(|S_{desired} - S_{calculated}|) < 0.01\text{mm} \quad (3.3)$$

This approach ensured that the final curve identified was the global optimum, matching the desired arc length—and therefore, indirectly, the curvature. The algorithm is generally represented in the flowchart of Figure 3.13. The variables x_A, x_B, and y_C represent the necessary x or y coordinates, respectively, of the three mid-span control points A, B, and C shown in Figure 3.12.

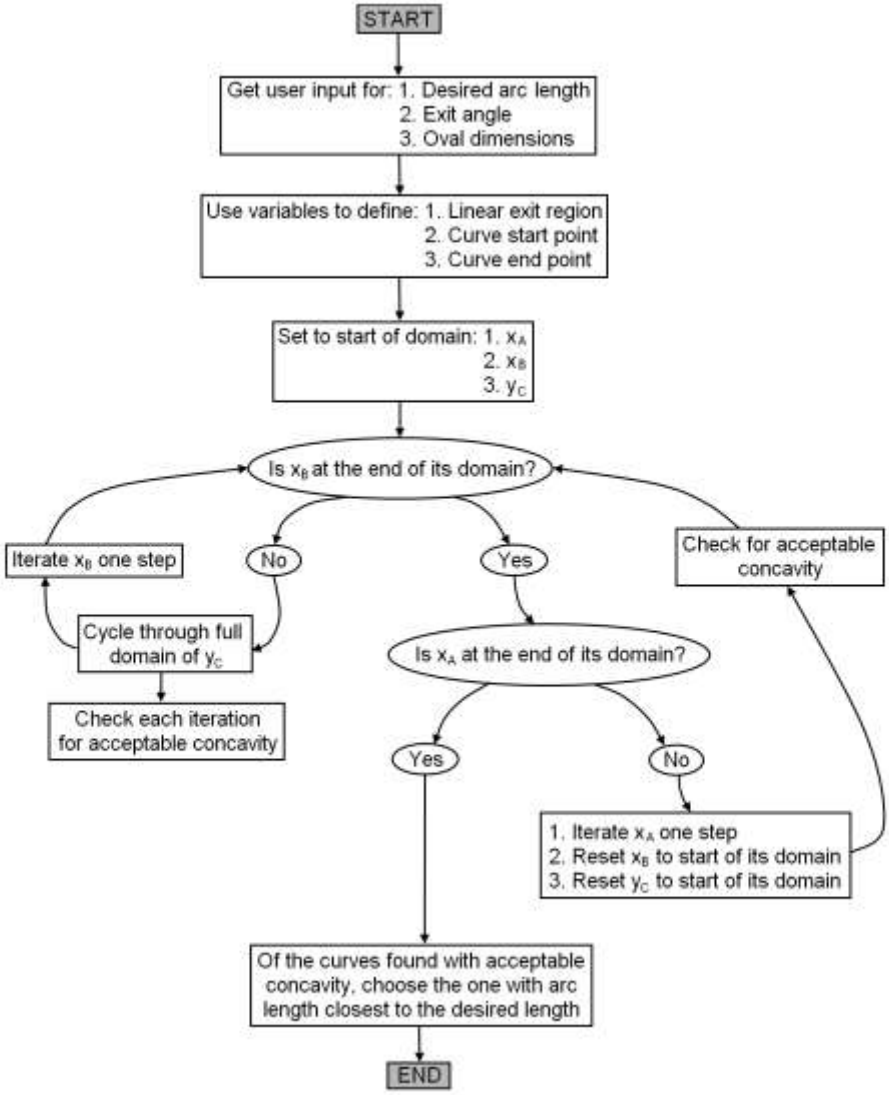

Figure 3.13: Flowchart representing the algorithm of the MATLAB code used to generate profile curves based on user-input.

Through the use of this exhaustive optimization methodology, the necessary curves were identified to fully define the three-dimensional internal nozzle geometry. The details of orienting and lofting these curves into the final shape is discussed in the following section.

3.3.5 Extrapolation to Three-Dimensional Solid

Multiple radial planes were chosen around the central streamwise axis in which to define the Bezier curves. Due to the experimental scope of the work and the 0.01 mm accuracy achievable by the rapid prototype modeling equipment, six planes proved sufficient to define distinct nozzle geometries, the orientation of which are shown in Figure 3.14.

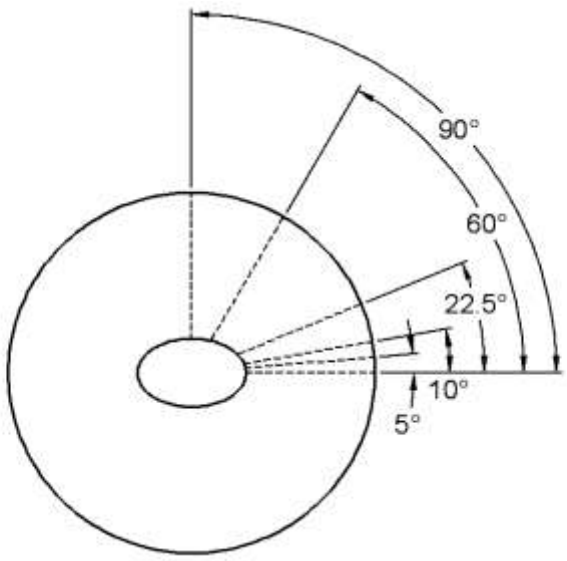

Figure 3.14: Orientation of planes in which profile curves are defined.

As mentioned in Section 3.3.2 during the discussion of arc length as a curve parameter, a linear progression was used to transition the various geometric attributes from one plane to the next; that is, as the orientation of the curve's plane varies from 0 to 90°, the arc length and exit angle vary linearly between the major axis plane and the minor axis plane. There is a higher concentration of planes near the major axis of the aperture in order to capture the more rapid change in curvature of the ellipse in this region.

A separate research project undertaken concurrently by mechanical engineering student Josh Latka delved into the exact repercussions of orienting the planes. Using the same design parameters as those used for this research—aperture aspect ratio, exit angle, and arc length—he utilized ten equally spaced planes instead of the six used in this work. The layout of equally spaced profile curves Latka developed is illustrated in Figure 3.15. The result of this placement was found to be a much more discontinuous internal surface contour, and similarly, a much higher overall jet divergence. The result of this side project was to confirm that six planes are sufficient to describe a complete set of nozzle contours.

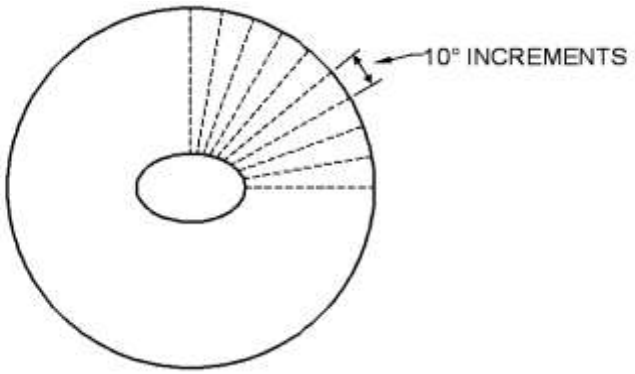

Figure 3.15: Ten equally spaced planes used in Josh Latka's work.

AutoCAD 2013 was then used to loft the curves symmetrically around the aperture to create a three-dimensional solid model. A StrataSys Dimension BST 1200ES series fused deposition rapid prototype modeler was then employed to fabricate the nozzle in acrylonitrile butadiene styrene (ABS) plastic. Figure 3.16 compares the CAD model and final product of a sample nozzle; prominent above the aperture is the guide boss used in mounting the nozzle to the experimental apparatus, and will be discussed in more detail in Section 3.4.

Figure 3.16: Sample nozzle as both a CAD model and final rapid-prototyped product.

This novel use of rapid prototyping and curve extrapolation in nozzle development made it possible to test many different nozzle designs in a cost-effective manner. Section 3.4 will next detail the experimental procedure employed to investigate the resultant behavior of jets issuing from these nozzles.

3.4 Jet Behavior Testing Process

A series of experiments were developed to study the three selected nozzle design parameters of aperture aspect ratio, exit angle, and arc length. Sections 3.4.1 and 3.4.2 below describe the experimental apparatus and procedures used in order to investigate characteristics of the resultant jets.

3.4.1 Experimental Setup

Experimental measurements of jet characteristics were carried out using a customized coolant system on a Blohm Planomat 408 CNC grinding machine. CimCool CimTech 310 cutting fluid maintained at 19°C and a Brix concentration of 6.6% was used in a recycled closed-loop delivery system. A Giant Triplex P400A pump driven by twin 575V motors was able to achieve a pressure of 0.586 MPa at a flow rate of 37.9 LPM given the size of the aperture to be used. For more extensive details concerning the grinding machine and cutting fluid pump apparatus, see Section 4.1.1, Table 1.

In order for the fluid to achieve the best possible velocity distribution—ideally, uniform—before reaching the nozzle, the coolant plumbing system was entirely redesigned from the factory setup. The stock setup is shown compared to the customized setup in Figure 3.17 (a) and (b), respectively. Rubber tubing routed along large radius curves replaced several short sections of straight pipe and elbow joints. A section of straight pipe then immediately preceded the nozzle. As demonstrated by Cui and Webster [1994], secondary flow along the mid-plane of a tube persists for some length. It can be effectively negated, however, through the use of either a long straight pipe or a flow conditioner—that is, a set of short tubes mounted in concentric rings in-stream. While a straight pipe having a length of 48 times the internal diameter of the pipe can virtually match the flow uniformity that can be achieved with a flow conditioner, a straight pipe having a length of 30 times the internal diameter of the pipe can reasonably approximate the flow uniformity that can be achieved with a flow conditioner. The setup used for this research consisted of a 787 mm section of 25.4 mm diameter straight pipe without a flow conditioner—a length approximately 31 times the diameter. As shown in Figure 3.17, the coherent jet of the customized system clearly achieves much lower jet dispersion than the stock setup.

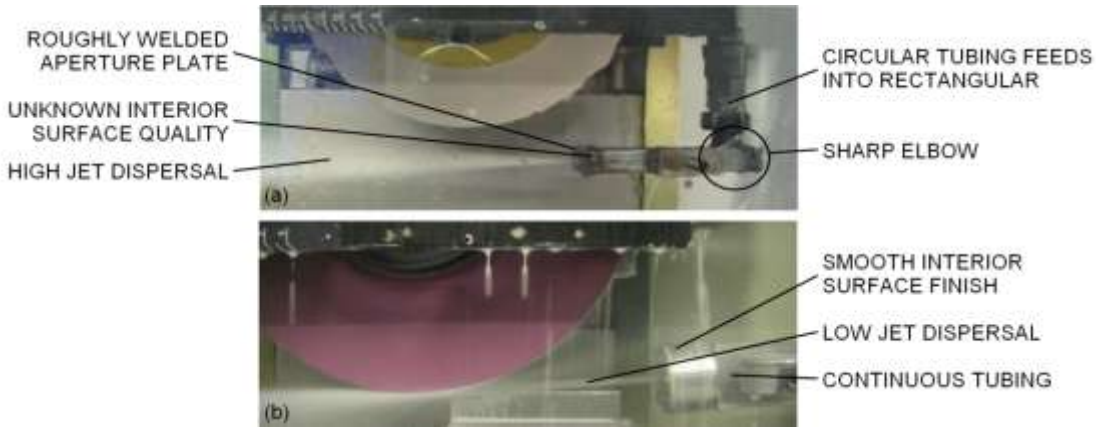

Figure 3.17: (a) Stock and (b) customized setup of coolant delivery system in the Blohm Planomat grinding machine.

To mount the rapid-prototyped nozzles to the existing plumbing of the grinding machine, an aluminum mounting block was fabricated. A schematic of the block is shown in

Figure 3.18 alongside a photograph of the setup. To ensure orthogonal alignment in both a vertical and horizontal orientation, a guide boss was modeled onto the nozzle and similarly cut out of the mounting block. With the nozzle mounted securely in the block, a view perpendicular to the jet was possible through the grinding machine viewing window.

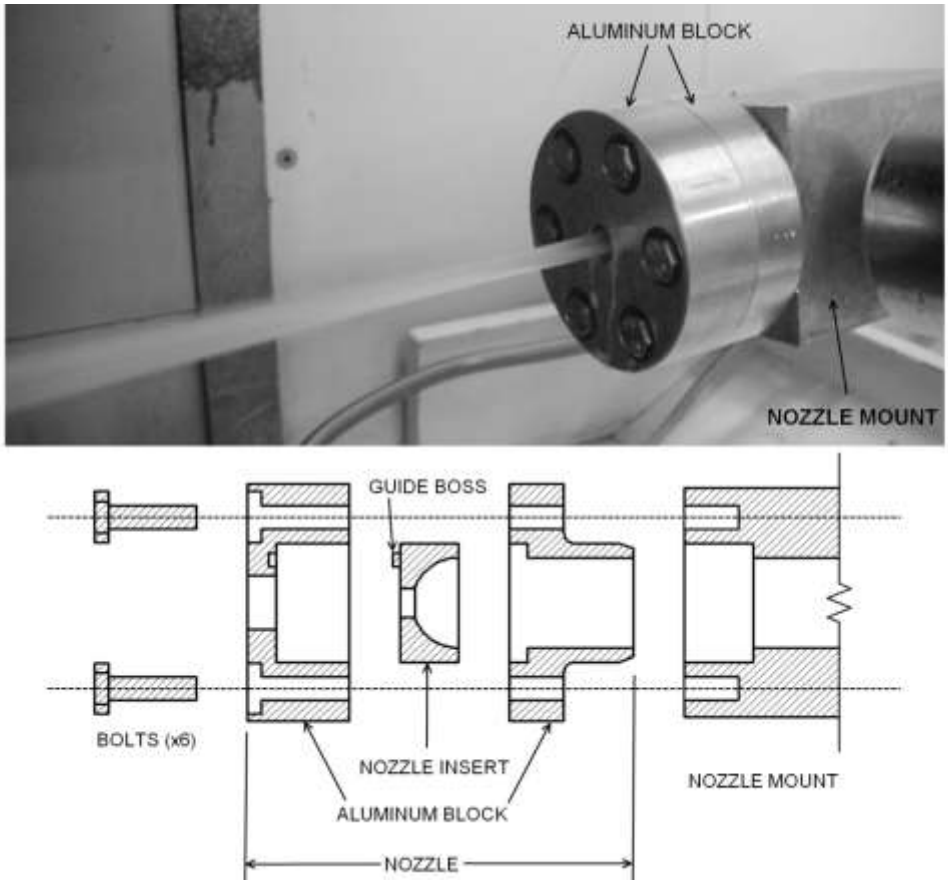

Figure 3.18: Schematic and photograph of nozzle assembly.

3.4.2 Experimental Procedure

The pressure and flow rate of the coolant was monitored and adjusted by digitally controlling the revolutions-per-minute (RPM) of the twin triplex pumps employed by the coolant system. Nozzles were tested at five RPM values corresponding to a range of flow rates; 13.6, 20.4, 26.9, 33.3, and 37.9 LPM. Because all nozzles used an aperture with an area equivalent to that of a 6 mm diameter circle, flow rates corresponded to the same RPM and pressure values for all experiments.

Given the orthogonal views allowed of the major and minor axis of the jet by the experimental apparatus discussed previously, image analysis proved to be the most effective measurement device to quantify downstream jet characteristics. Multiple digital images of the fluid jet were taken at each flow rate with an 8.0 megapixel Pentax Optio Z10 digital camera against a high-contrast background panel fixed to the grinding machine; as shown in Figure 3.19 for the major and minor axes of two sample nozzles. Measurements of jet width and divergence angle were then obtained through image analysis performed in AutoCAD and calibrated through the use of a scale present in each photograph. The locations where these measurements were taken in each image are also shown in Figure 3.19. A similar digital image analysis methodology was used by St-Pierre et al. [2012] during their investigation of jet divergence angles of Rouse nozzles. In the present work, three images were taken of each jet at each tested flow rate, and the resulting measurements of jet width and divergence angle averaged to produce the data discussed in the following section.

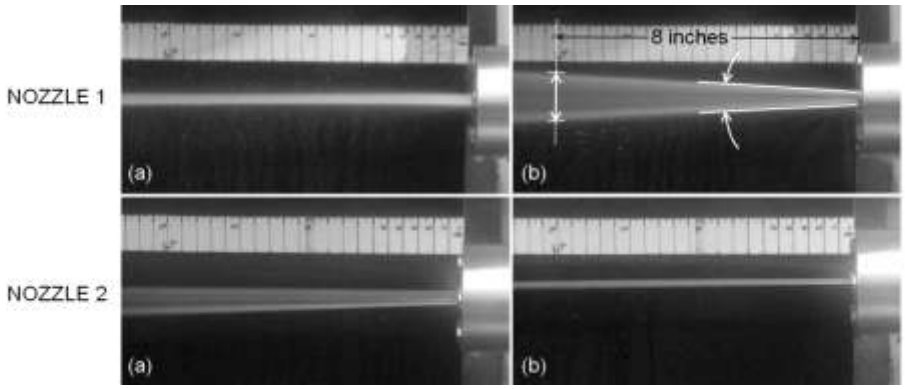

Figure 3.19: (a) Major and (b) minor axis views of sample jets 1 and 2, with locations of observed divergence angle and jet width measurements indicated.

3.5 Summary of Jet Characteristics

The following section details the results of experimental testing performed on 29 nozzles with unique internal geometries to investigate the effects of aperture aspect ratio, exit angle, and arc length on the properties of their resultant jets. This discussion will begin by highlighting apparent trends in jet divergence angles and jet fluid distribution. Section

3.5.1 first divides the observed jet divergence results into three categories based on the three design parameters tested: exit angle, arc length range, and aperture aspect ratio. After presenting the data, the ideal geometries tested are discussed in Section 3.5.2 accompanied by a brief description of work conducted alongside this research by Josh Latka. In order to begin transitioning to the next stage of this research project—that is, application of these low-divergence elliptical jets to creep-feed grinding—Section 3.5.3 introduces the idealized theoretical jet fluid distribution for several jets tested in comparison to the profile of a sample workpiece to be used in the eventual creep-feed grinding process.

3.5.1 Jet Divergence Angle

The most informative and useful observed jet characteristic proved to be the divergence angle; in grinding and other machining operations, it is the low divergence angle that makes a coherent coolant jet valuable for its ease of use and precision. The following Sections 3.5.1.1, 3.5.1.2 , and 3.5.1.3 detail the results of investigating the effects on jet divergence of manipulating exit angle, arc length, and aperture aspect ratio.

3.5.1.1 Exit Angle Investigation

To study the effect that different exit angles have on the resulting jet divergence, Figure 3.20 (a) and Figure 3.20 (b) plot the minor and major axis jet divergence, respectively, as a function of the major axis exit angle for different flow rates and minor axis exit angles. This data was collected at a constant aperture aspect ratio of 1.56 and arc length range of 0.0 mm–that is, a uniform arc length for all profile curves.

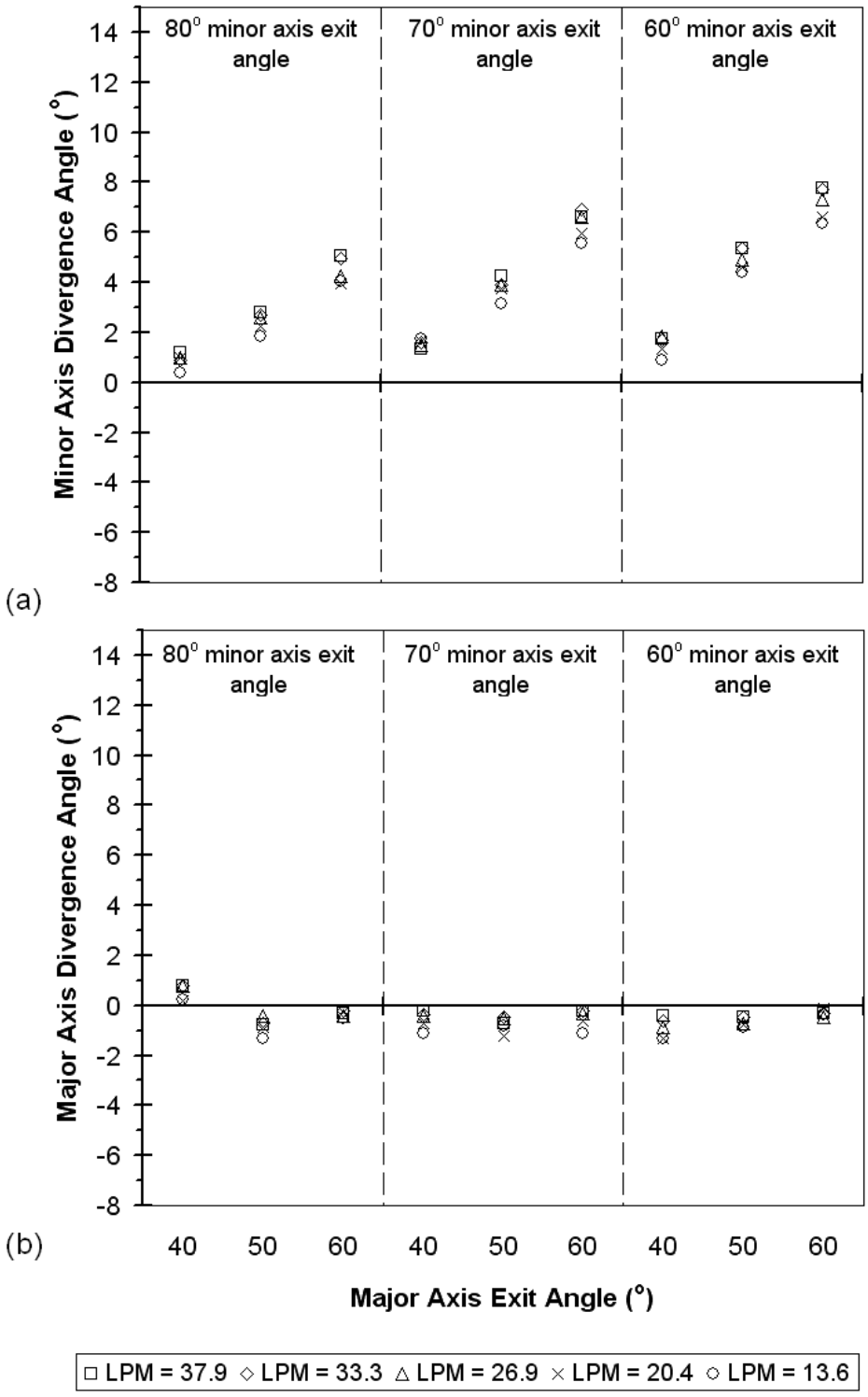

Figure 3.20: (a) Minor axis and (b) major axis jet divergence values as functions of both the major axis exit angle and minor axis exit angles; multiple flow rates are super-imposed. Constant aperture aspect ratio of 1.56; constant arc length range of 0.0 mm.

It can be seen in Figure 3.20 (a) that the minor axis jet divergence angle appears to increase when: the flow rate increases, the major axis exit angle increases, or the minor axis exit angle decreases. Having a high major axis exit angle around the elliptical aperture approaches the fluid conditions induced by simply cutting an aperture into a flat plate—as is standard practice for creating a nozzle in many applications. Indeed, the observed jet divergence angles of 5 to 10^{o} in the minor axis plane corroborate numerous previous studies of high-entrainment jets emerging from flat plate orifices, such as those of Azad *et al.* [2012], Iyogun and Birouk [2009], Quinn [2006], and Quinn and Marsters [1985]; that is, large jet spread in the minor axis. Changes in the major and minor exit angles, however, have no significant influence on the divergence of the jet in the major axis plane as shown in Figure 3.20 (b) by the relatively flat distribution of points across the various exit angles tested. The negative divergence angle values represent a short initial period of convergence within the first few millimeters of the jet. This initial convergence was inevitably followed shortly thereafter by dispersion and jet breakup. Axially asymmetric divergence angles—that is, divergence in one plane being unequal to that of the orthogonal plane—were observed for all nozzles. However, the nozzle with 40° and 80° major and minor axis exit angles, respectively, showed remarkably low divergence in both axes; 0.8° in the major axis and 1.2° in the minor axis for the highest pressure tested.

3.5.1.2 Arc Length Investigation

To study the effect of the arc lengths of various cross-sectional curves around a nozzle on the resulting jet divergence, the variance between maximum and minimum arc lengths of a nozzle were tested, namely, the arc length range. Figure 3.21 (a) and Figure 3.21 (b) plot the minor and major axis jet divergence, respectively, as functions of arc length range for different flow rates and minor axis exit angles. These experiments were performed with a constant aperture aspect ratio of 1.56 and a major axis exit angle of 50°—values chosen to yield the largest possible testable region of parameters.

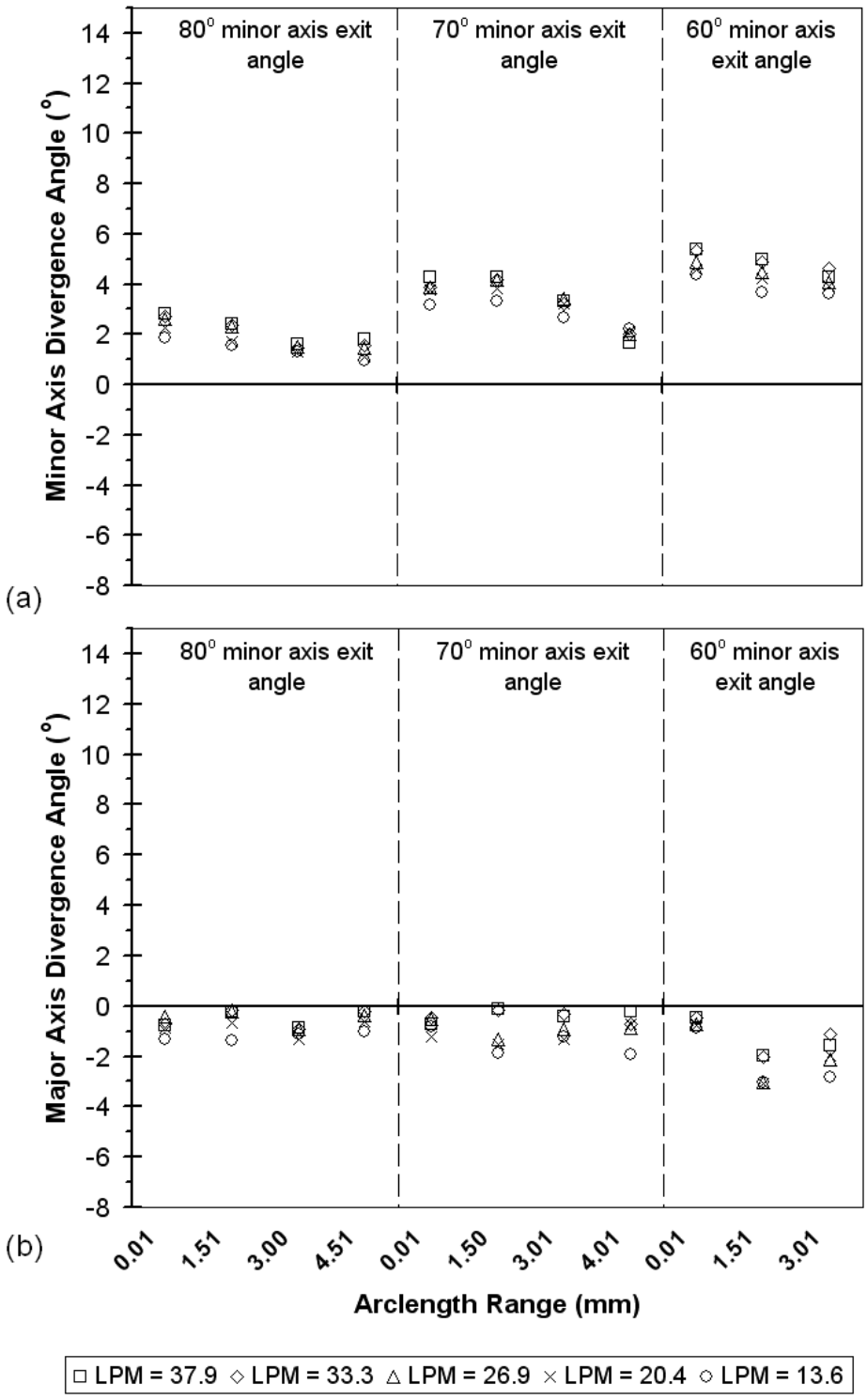

Figure 3.21: (a) Minor axis and (b) major axis jet divergence as functions of both the arc length range and minor axis exit angle; multiple flow rates are super-imposed. Constant aperture aspect ratio of 1.56; constant major axis exit angle of 50°.

As the arc length range around the internal contouring of a nozzle increases—that is, as regions of the contour gain or lose arc length with respect to other areas—the minor axis jet divergence angle appears to decrease as shown in Figure 3.21 (a). Furthermore, increasing the minor axis exit angle also causes the minor axis divergence angle to decrease. There are no apparent effects, however, of arc length range on the major axis divergence angle, as illustrated in Figure 3.21 (b) by the relatively unpredictable distribution of points for each of the arc length ranges and minor axis exit angles tested.

3.5.1.3 Aperture Aspect Ratio Investigation

To understand the effects that different aperture aspect ratios have on the resulting jet divergence, Figure 3.22 (a) and Figure 3.22 (b) illustrate the minor and major axis jet divergence, respectively, as functions of aperture aspect ratio for different flow rates and minor axis exit angles. The nozzle arc lengths for this set of experiments were held uniform while the major axis exit angle was fixed at 50°—again, these values were chosen to yield a large testable domain of parameters.

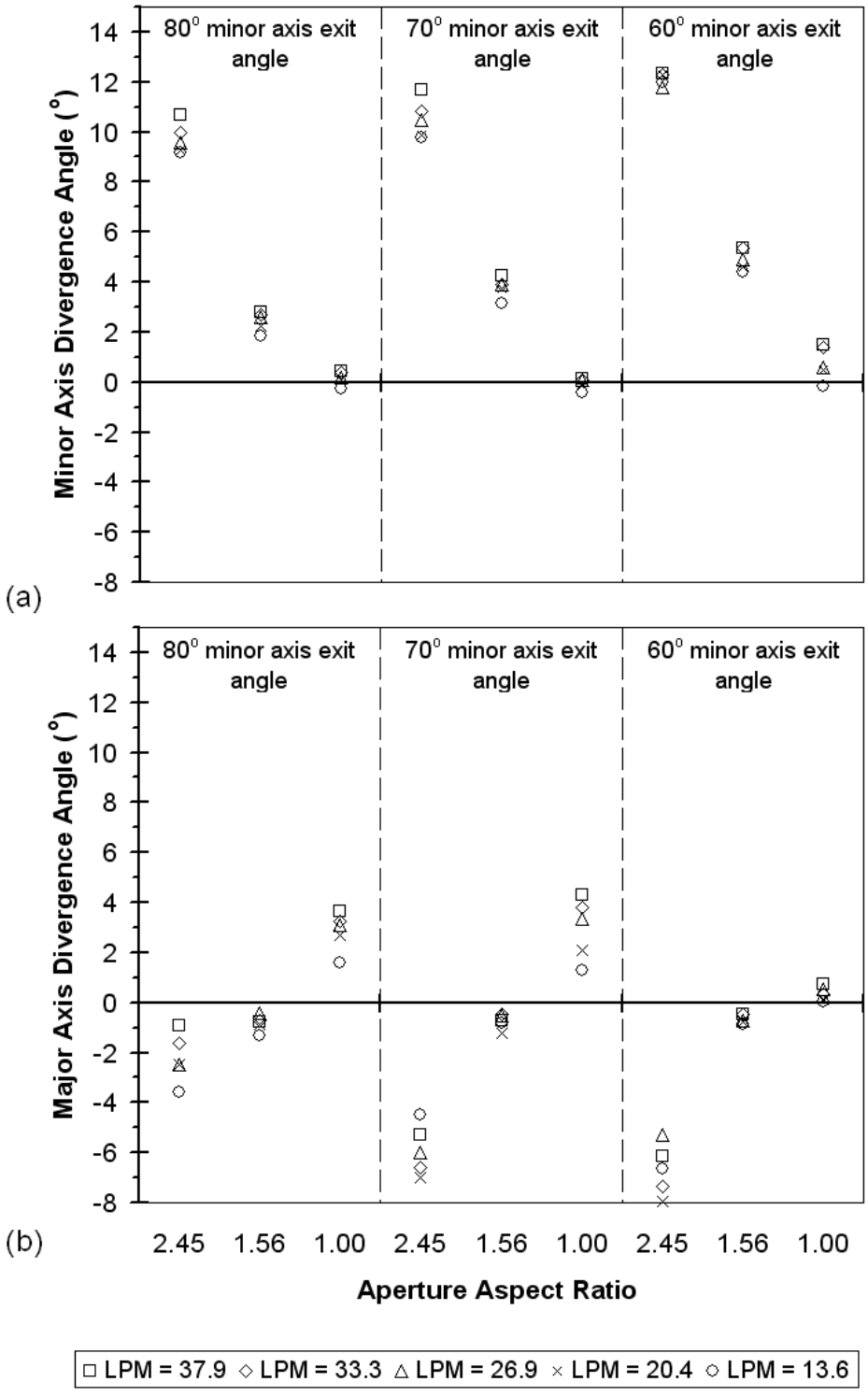

Figure 3.22: (a) Minor axis and (b) major axis jet divergence as functions of both aperture aspect ratio and minor axis exit angle; multiple flow rates are super-imposed. Constant arc length range of 0.00 mm; constant major axis exit angle of 50°.

It can be seen that high aperture aspect ratio nozzles yield jets with high divergence angles in both axes. As the aspect ratio of the aperture decreases to 1.00, the divergence angles similarly decrease. At an aspect ratio of 1.00, the nozzle indicated by the furthest right points in Figure 3.22 (a) and (b) shows the best coherency; this result is expected because the minor axis exit angle is 60° and the major axis exit angle was fixed at 50°, and so therefore the nozzle is nearly radially symmetric.

3.5.2 Lowest Divergence of an Elliptical Jet

The lowest overall divergence achieved with an elliptical jet was found to be competitive with the standard idealized circular coherent jet. Sample digital images of the minor and major axes of the most successful elliptical jet are shown in Figure 3.23 (a) and Figure 3.23 (b), respectively. The nozzle capable of producing this jet is represented by the data point in Figure 3.20 (a) and Figure 3.20 (b) having an aperture aspect ratio of 1.56, arc length range of 0.00 mm, and minor and major axis exit angles of 80° and 40°, respectively.

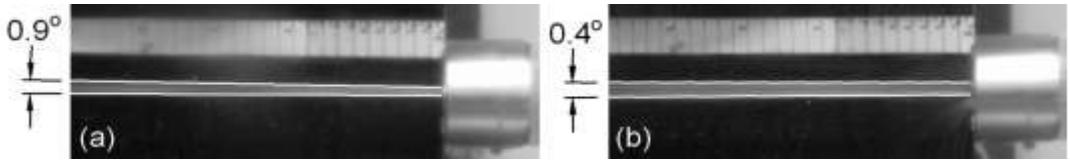

Figure 3.23: Digital images of the lowest divergent elliptical jet tested in the (a) minor and (b) major jet axes; testing flow rate of 33.3 LPM.

A topographical diagram of the internal contouring of this ideal nozzle is shown in Figure 3.24, with a note indicating an unusual "ridge" landmark brought about directly by the arc lengths necessary to fulfill the constraint of a uniform arc length around the contour. Also important to note with Figure 3.24 is that the central isometric lines nearest the aperture are placed at heights separated by 0.5 mm, whereas the rest of the topographical isolines are spaced apart by 1 mm.

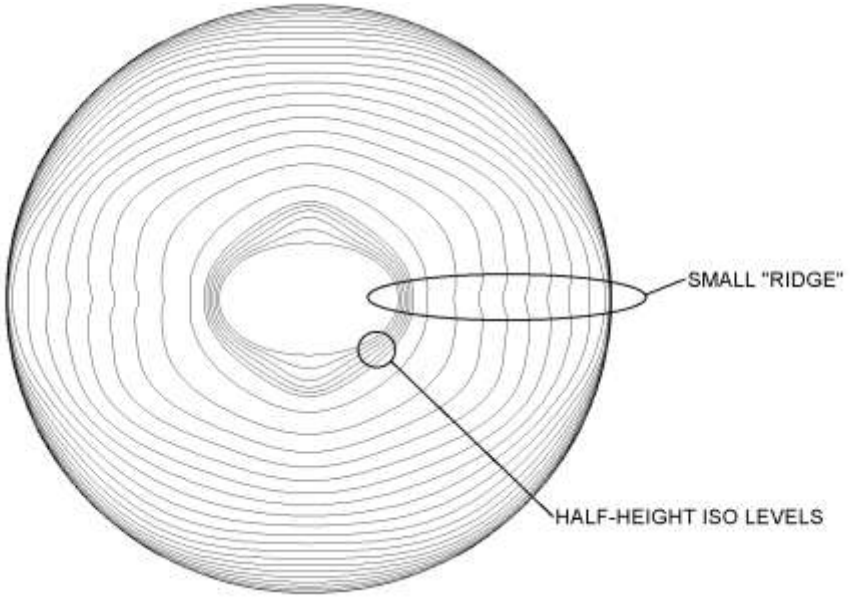

Figure 3.24: Topographical diagram of a nozzle having an aperture aspect ratio of 1.56, arc length range of 0.00 mm, and minor and major axis exit angles of 80° and 40°, respectively.

The divergence angles of this jet were the smallest exhibited by any of the jets within the range of geometric parameters tested: at a flow rate of 33.3 LPM—a standard value for use in grinding—the minor axis divergence angle was 0.9^{o} and the major axis divergence angle was 0.4°. Coherency, as defined by the ratio of the jet diameter at the aperture to the jet diameter at 200 mm, or approximately 8 inches, is 0.82 in the minor axis and 0.86 in the major axis. For comparison, a circular jet of similar scale with a coherency of 0.92 is shown in Figure 3.25.

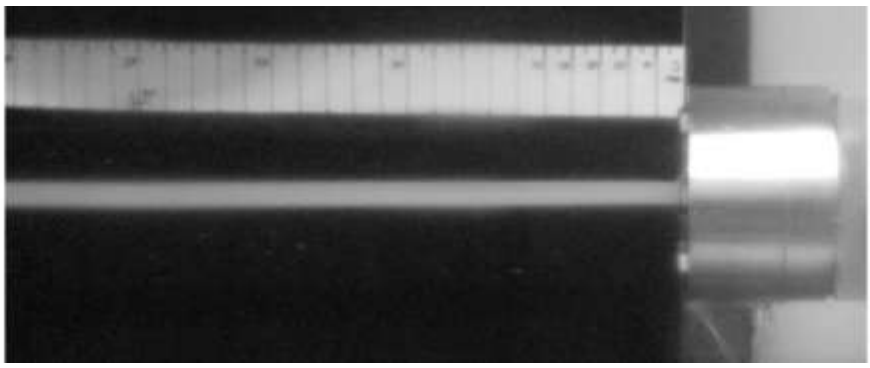

Figure 3.25: Digital image of a jet with a coherency of 0.92 emerging from a circular nozzle.

3.5.3 Fluid Distribution

In addition to analysis of the digital images with an eye toward divergence angle, further inspection of apparent fluid homogeneity within the visible planar region of the jet for 200 mm downstream of the nozzle was also possible. Uniformity across a fluid jet is a highly desirable characteristic previously only encountered in circular coherent jets. For comparison, the ideal elliptical jet illustrated previously in Figure 3.23 (a) and (b) has high homogeneity while the jet illustrated in Figure 3.26 (a) and Figure 3.26 (b) has low homogeneity.

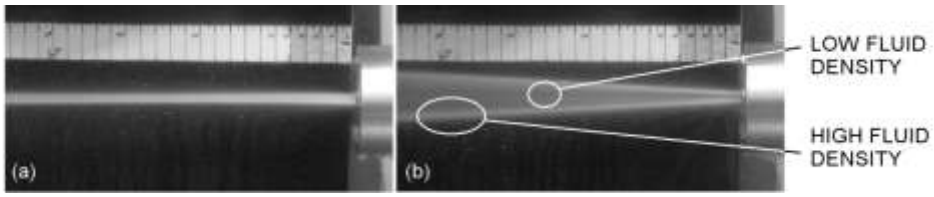

Figure 3.26: Jet showing low fluid homogeneity, (a) minor and (b) major axis views.

In application to grinding, specifically profiled grinding, Figure 3.27, Figure 3.28, and Figure 3.29 illustrate jet cross-sections for the circular coherent jet and the final elliptical nozzle selected in both orientations, respectively, at 200 mm downstream—the location of impact with the grinding zone.

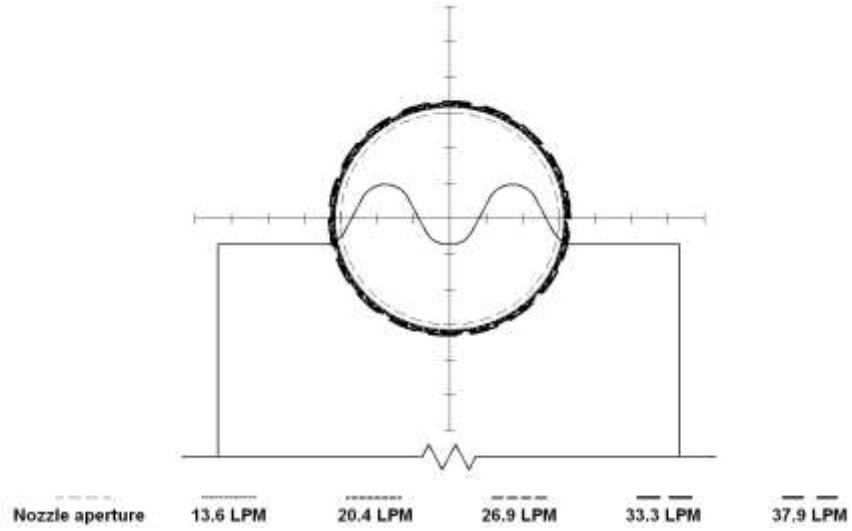

Figure 3.27: Theoretical circular jet cross-sections at the grinding zone for various flow rates.

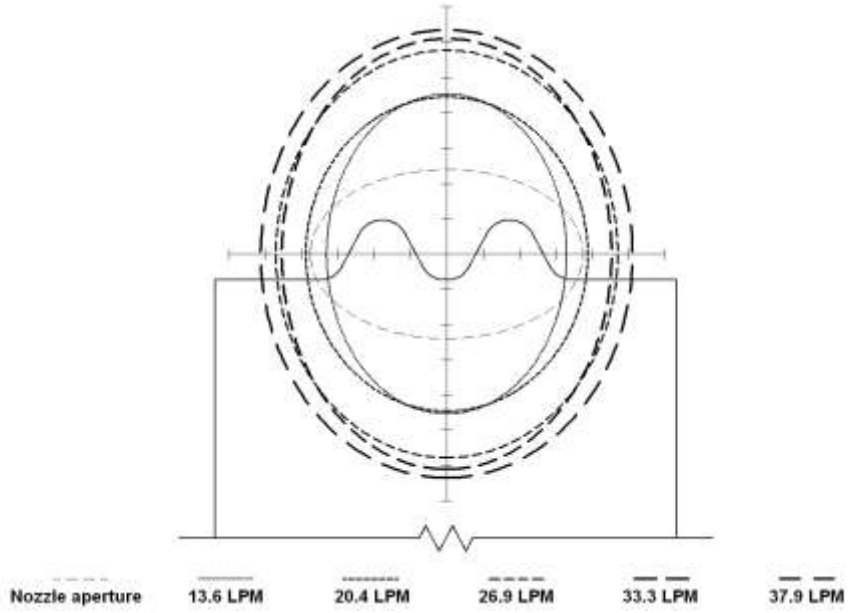

Figure 3.28: Vertical jet orientation; jet expansion at the grinding zone for various flow rates.

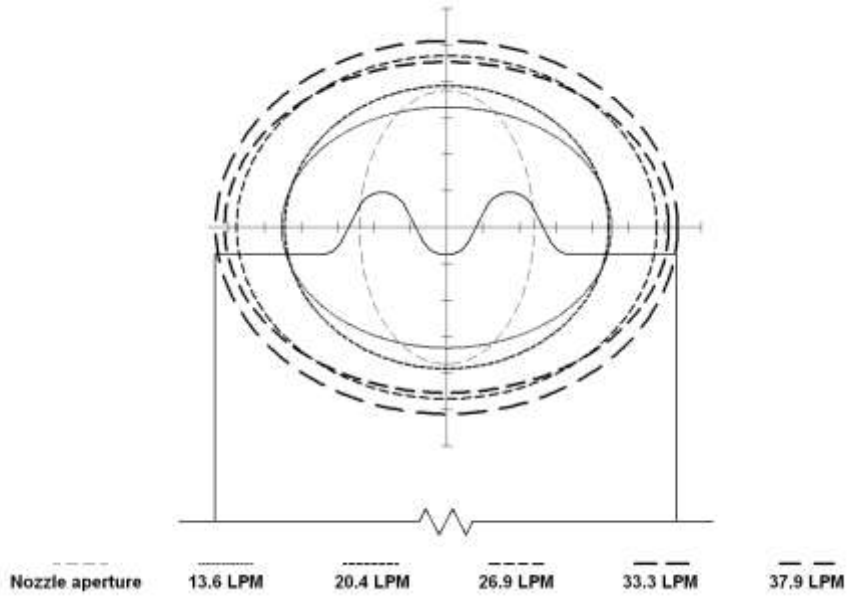

Figure 3.29: Horizontal jet orientation; jet expansion at the grinding zone for various flow rates.

The circular jet in Figure 3.27 is applying insufficient coolant to the profiled workpiece; all the coolant is directed at the central valley of the profile. Conversely, for flow rates above 26.9 LPM, the elliptical jets in Figure 3.28 and Figure 3.29 are not only applying coolant across the entire central core of the profile, but do so using the same fluid volume, fluid homogeneity, and jet pressures as the circular jet. Also, as discussed

previously, note the 90° offset of the aperture major axis with respect to the jet major axis.

3.6 Summary

Fluid jet characteristics associated with the modification of several novel design parameters for low-divergence nozzles were examined in this Chapter using rapid-prototyped models and digital image analysis. Exit angle, arc length range, and aperture aspect ratio were the design parameters selected for the investigation. The geometry for each nozzle was generated by producing six unique fourth-order Bezier curves with user-specified properties. These curves were then arrayed about a point and lofted to form a three-dimensional nozzle in AutoCAD, which was subsequently fabricated with a rapid-prototype fused deposition modeler.

Results of digital imaging experiments at various flow rates show that minor axis jet divergence can be reduced by increasing the minor axis exit angle while holding fixed the major axis exit angle. Minor axis jet divergence can also be decreased by increasing the major axis exit angle. Furthermore, major axis jet divergence is seemingly not affected by exit angles or arc length range.

Of the elliptical aperture nozzles tested in this research, the best nozzle—in terms of divergence angle and flow homogeneity—had a major axis exit angle of 40° and a minor axis exit angle of 80°, along with an arc length range of 0.00 mm and an aperture aspect ratio of 1.56 at a flow rate of 33.3 LPM. The trends discovered during this research will enable the development of jets with predictable angles of divergence in both the major and minor axes. Given the low divergence angles yielded, the results also indicate that elliptical jets are now a viable alternative to circular jets if a wider, narrower cross-sectional region is required in addition to a predictable direction, divergence rate, and flow distribution.

Based on the theoretically possible fluid distributions discovered through this research, the grinding work subsequently conducted and summarized in Chapter 5 began with an

initial hypothesis that the elliptical jets would perform differently than the circular jet across a variety of comparable grinding and fluid parameters. This hypothesis will be expanded and then experimentally investigated in the following Chapters.

CHAPTER 4 Preliminary Experiments and Testing Procedure

The previous chapter discussed the development and testing of a variety of nozzles. Several nozzle design parameters; namely, exit angle, arc length, and aperture aspect ratio, were evaluated through analysis of the jet emerging from the nozzle with an eye toward low divergence and high fluid uniformity from an elliptical jet. A single elliptical nozzle with ideal jet properties was developed, and the following chapter will describe the experimental procedure necessary to evaluate its performance in application to profiled creep feed grinding alongside a standard circular jet. Section 4.1 will first describe the grinding, dressing, surface measurement, and data acquisition equipment and parameters. Cutting fluid equipment and parameters follow in Section 4.2. Section 4.3 explains the final experimental procedure in addition to the procedure of surface analysis performed subsequently on the finished workpieces. Finally, Section 4.4 will summarize the preliminary experiments and procedures in preparation of introducing the results discussed in Chapter 5.

4.1 Experimental Apparatus

This section will present the apparatus and system parameters employed during the grinding phase of this research. Section 4.1.1 will first detail the grinding, surface measurement, and data acquisition apparatus, followed by Section 4.1.2 with the grinding and dressing parameters.

4.1.1 Grinding and Data Acquisition Equipment

All grinding experiments were performed on the apparatus shown in Figure 4.1.

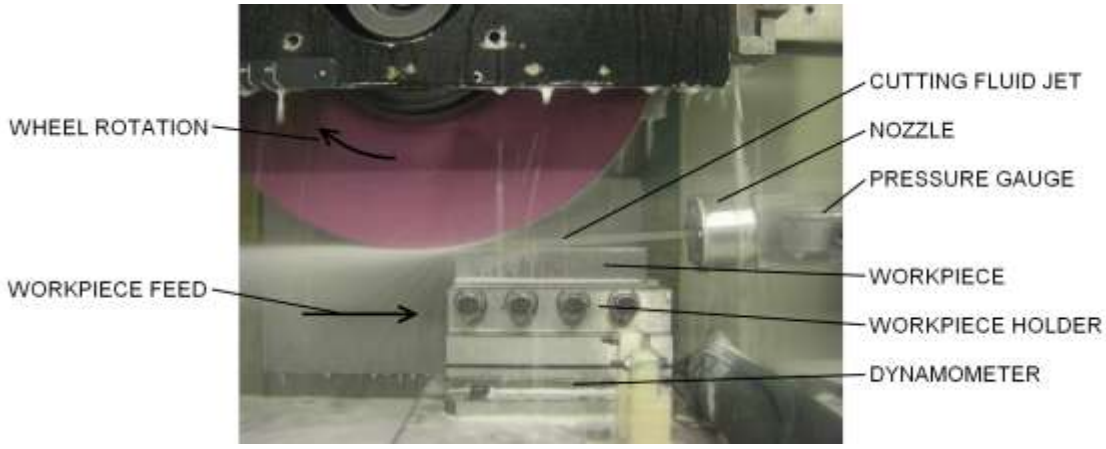

Figure 4.1: Photograph of experimental apparatus immediately prior to start of cutting.

The grinding machine used was a Blohm Planomat CNC grinding machine equipped with twin triplex cutting fluid pumps. A force dynamometer was mounted rigidly to the carriage of the machine to which the mounting fixture for workpieces was mounted. The dynamometer was capable of recording the normal, tangential, and thrust forces via a purpose-built LabView program and National Instruments DAQ card. In addition, the real-time grinding wheel spindle power could also be recorded. The wheel employed was an industry standard vitrified aluminum oxide wheel from Radiac, and the workpieces to be ground were cold-rolled 1018 low carbon steel flat bar. Details of this equipment are enumerated in Table 1.

Table 1 – Grinding and Data Acquisition Equipment

Component	Make and Model
GRINDING APPARATUS	
Grinding Machine	Blohm Planomat 408
Grinding Machine Controller	GE Fanuc Series 10i-M
Cutting Fluid	CimCool CimTech 310
Cutting Fluid Pump	Giant: P400A Series Triplex Ceramic Plunger Pump
Pump Motor	Reliance Electric: Calibre 575V Standard Motor, Enclosed
Motor Controller	GS2 Series AC Drive
Grinding Wheel	Radiac: RPA 801 G+800 VOS, 0.875 inch width
DATA ACQUISITION SYSTEM	
DAQ Computer	Pentium 4, 2.4 GHz, 512 MB RAM, Windows 2000
Acquisition Program	Purpose-designed program compiled in LabView
Data Acquisition Card	National Instruments: PCI-MIO-16XE-10
Connector Block	National Instruments: BNC 2120
Force Dynamometer	Kistler: 3 Component Dynamometer, Type 9257 B
Force Amplifier	Hoskin Scientific: Multi-Channel Charge Amplifier, Type 5019
Spindle Power Meter	Load Controls Inc.: PH-3A Power Cell Power Transducer
WORKPIECE	
Material	1018 Cold rolled steel bar stock
Preparation	Upper and lower surfaces leveled
Approx. overall dimensions	152.4 x 12.7 x 50.8 mm
Profile depth	1.70 mm

4.1.2 Grinding and Dressing Parameters

Dressing parameters were held constant throughout all preliminary and final experiments. Non-continuous profiled diamond roll dressing was utilized with an in-feed of 0.762 μm per wheel rotation, and an aggressive 0.381 mm dressing depth was found to be necessary because of the large amounts of wheel breakdown that occurred during grinds where cutting fluid starvation occurred. A dressing ratio of 0.85 was used with 0 roll out passes.

A range of grinding parameters was used: three feed rates, four jet pressures, and three jet shapes. The domains of each of these tested parameters were bounded by both previous research and industry standards so that the resultant workpiece surface finishes could be evaluated by comparison. Nozzles used included a circular aperture and two orientations of an elliptical aperture, jet pressures ranged from 0.45 to 4.45 MPa, and feed rates

ranged from 100 to 200 MPa. A detailed description of the dressing and grinding parameters is provided in Table 2.

Table 2 – Dressing and Grinding Parameters

Parameter	Value
DRESSING PARAMETERS	
Style	Non-continuous diamond roll dressing
Dressing wheel	Norton RPC 6393
In-feed	0.762 μm/wheel rotation ($30x10^{-6}$ inch/wheel rotation)
Total in-feed	0.381 mm
Grinding wheel speed	22.35 m/s (4400 ft/min)
Dressing wheel ratio	0.85
Number of roll out passes	0
Sense of rotation	Down-cut dressing
GRINDING PARAMETERS	
Depth of cut	1.78 mm
Wheel speed	22.35 m/s (4400 ft/min)
Sense of rotation	Down-cut grinding
Feed rates	100, 150, 200 mm/min
Coolant nozzles	Circular, elliptical (See Table 3 for design parameters)
Nozzle standoff	200 mm
Nozzle orientations	Vertical ellipse, horizontal ellipse
Coolant jet pressures	0.45, 1.72, 3.21, 4.45 MPa

4.2 Cutting Fluid Apparatus Preliminary Testing

The following Section 4.2.1 describes the selection of the nozzle dimensions; Section 4.2.2 deals with the subsequent creation of the nozzles. Section 4.2.3 will then explain how proper nozzle orientation was determined for application of the cutting fluid to creep feed grinding.

4.2.1 Selection of Nozzle Dimensions

As discussed, the coolant delivery system has a positive displacement Giant P400A triplex pump, capable of pumping a variety of fluids and slurries. As shown in Figure 4.2 from Murphy *et al.* [2007]—modified from the original to utilize SI units—these pumps can produce approximately 9 MPa (1200 PSI) when used with circular coherent nozzles of 2 or 3 mm aperture diameter; as measured immediately before the nozzle inlet. Larger diameter apertures of 4 or 5 mm yield pressures of less than 2.76 MPa at the maximum possible flow rates and are therefore not used in this study.

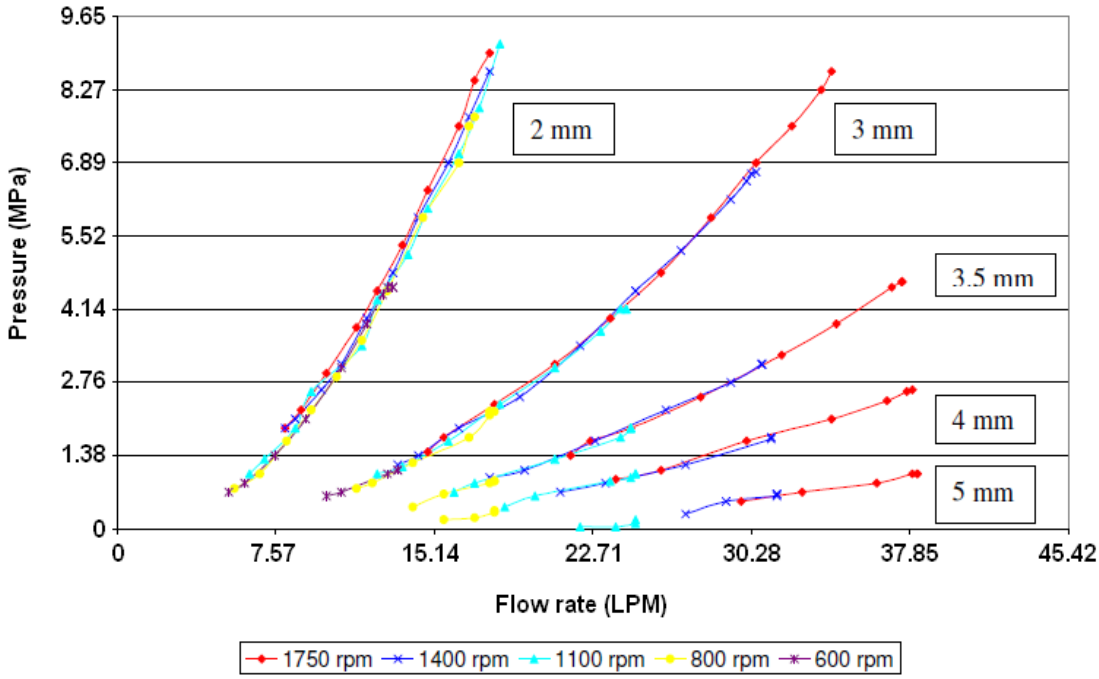

Figure 4.2: Pressures and flow rates achievable with equipped coolant system for various pump RPM and various aperture diameters; fluid units converted to SI from source figure [Murphy *et al.* 2007].

Given the dimensions of the workpiece to be used—shown in Figure 4.3 (a) and Figure 4.3 (b)—an aperture roughly 3.5 mm in diameter was selected. The peaks of the workpiece profile occur 3.5 mm apart, and therefore fluid distribution on the extremities of these peaks can be investigated using a nozzle of roughly the same size scale with slight variations in coverage area.

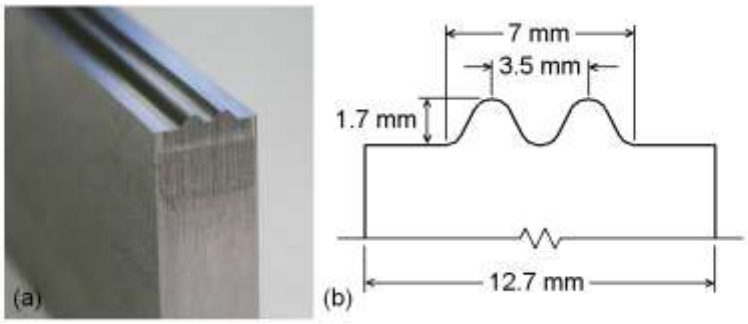

Figure 4.3: (a) Profiled workpiece and (b) dimensions.

A circle of diameter 3.5 mm and an equivalent oval of aspect ratio 1.56—as was determined the ideal aspect ratio for an elliptical aperture—share the same area value.

Given this area and the known flow rate achievable with the coolant pump as shown in Figure 4.2, jet velocity at the aperture was calculated using the approximation:

$$v_j = Q/A * (6.309*10^{-5}) \quad (4.1)$$

where v_j is the jet velocity in meters per second, Q is the fluid flow rate in gallons-per-minute (GPM), A is the area of the aperture in square meters, and the multiplier is the conversion factor from GPM to cubic meters per second. This jet velocity equation is graphed in Figure 4.4 with respect to jet pressure. The peripheral wheel speed of 22.35 m/s is also indicated.

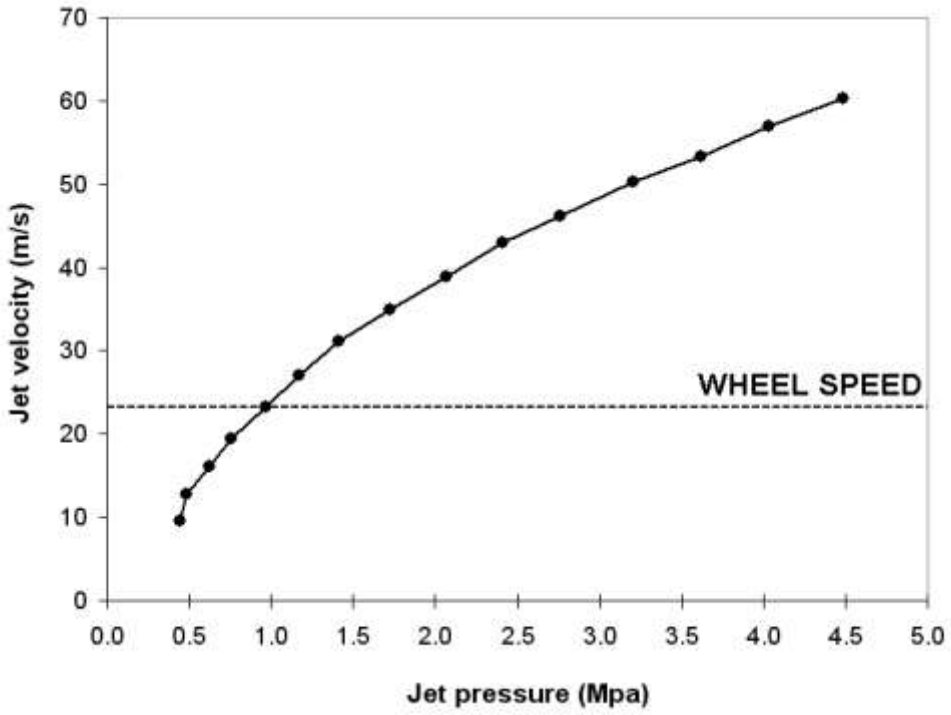

Figure 4.4: Achievable jet velocity at the nozzle for various jet pressures, aperture equivalent in area to a circle 3.5 mm in diameter.

A coherent jet with a diameter of 3.5 mm was selected not only for the specific size scale of the workpiece, but also for the large achievable range of appropriate jet pressures and velocities. Using an aperture of this size fulfils the recommendation that a coolant jet velocity be at least 80% that of the wheel periphery [Engineer *et al.* 1992]. Four

pressures were chosen for study from across the spectrum: 0.45, 1.72, 3.21, and 4.45 MPa.

4.2.2 Generation of Specific Nozzles

The procedure described in Chapter 3 was used to generate both a circular nozzle with an aperture 3.5 mm in diameter and an equivalent elliptical nozzle. The exit angle, arc length range, and aperture aspect ratio of the ideal elliptical nozzle discussed in Section 3.5.2 were used to develop the elliptical nozzle with an area equal to that of a 3.5 mm circle. The effective contraction ratio—as defined by inlet area divided by outlet area—had to be changed from 17.5 to 51.5, resulting in a less coherent jet. The circular and elliptical nozzles shared an aperture area and a uniform arc length range of 0.00 mm. Where the circular nozzle had a uniform exit angle of 80° around the aperture, the elliptical nozzle utilized 40° and 80° exit angles for the major and minor axes, respectively. A detailed summary of the geometric attributes of the nozzles is listed in Table 3.

Table 3 – Nozzle Design Parameters

Parameter	Value
CIRCULAR 3.5 mm DIAMETER NOZZLE	
Aperture diameter	3.5 mm
Aperture area	9.6 mm^2
Contraction ratio	51.5
Arc length range	0.0 mm
Exit angle	80°
ELLIPTICAL 3.5 mm EQUIVALENT DIAMETER NOZZLE	
Major axis, minor axis	4.38, 2.8 mm
Aperture area	9.6 mm^2
Effective contraction ratio	51.5
Arc length range	0.0 mm
Major axis exit angle	40°
Minor axis exit angle	80°

Three photographs were taken at each pressure to be used in the grinding experiments for every nozzle. For the elliptical nozzle, images were obtained of both the vertical and horizontal jet orientation. From the divergence angles and jet widths obtained through

analysis of these images, Figure 4.5 through Figure 4.7 were generated to show expansion of the jet cross-section at 200 mm downstream of the nozzle with increasing pressure. The position 200 mm was chosen for investigation because the standoff distance between the grinding zone and the nozzle aperture during all experiments was fixed at this value so that the nozzle did not interfere with the workpiece during grinding experiments. Figure 4.5 shows the expansion of the circular jet with respect to pressure superimposed over the workpiece profile.

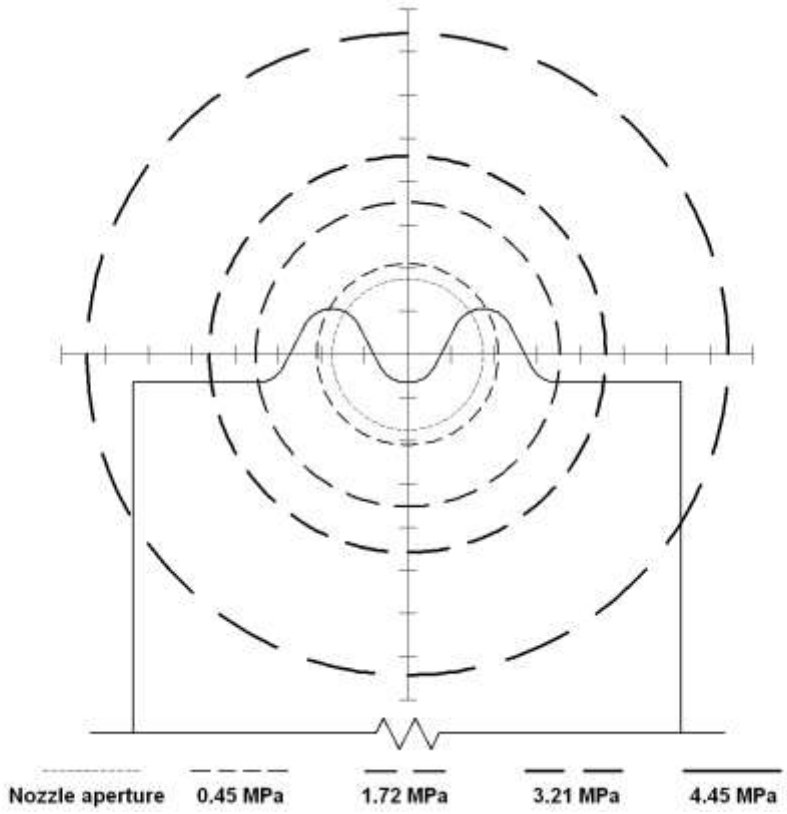

Figure 4.5: Circular jet cross-sections 200 mm downstream for various pressures.

Figure 4.6 and Figure 4.7 show the expansion of the elliptical jet when positioned in the vertical and horizontal orientations, respectively.

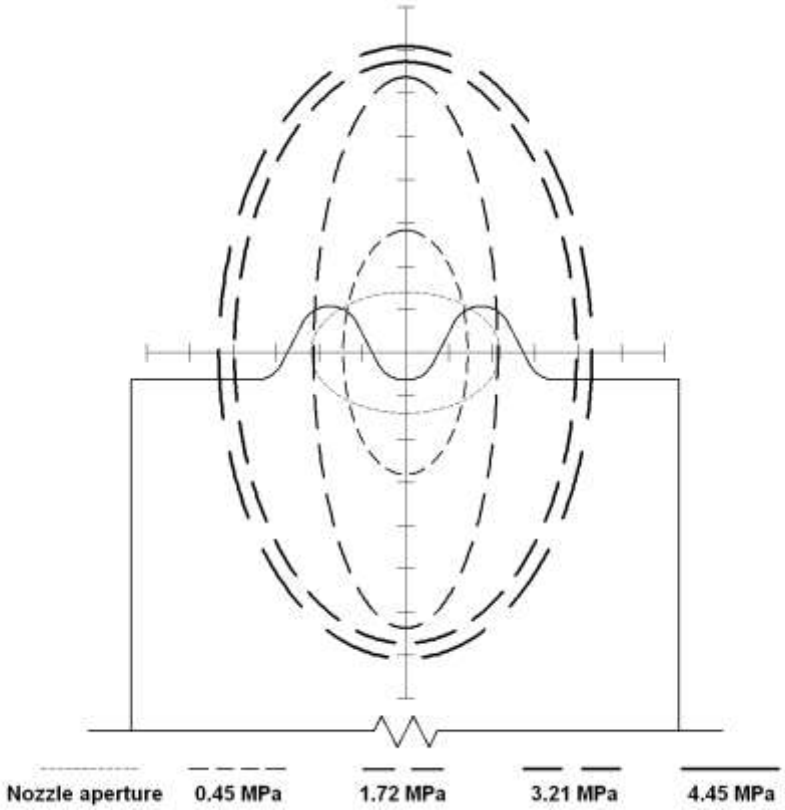

Figure 4.6: Elliptical jet cross-sections 200 mm downstream for various pressures; "vertical jet orientation".

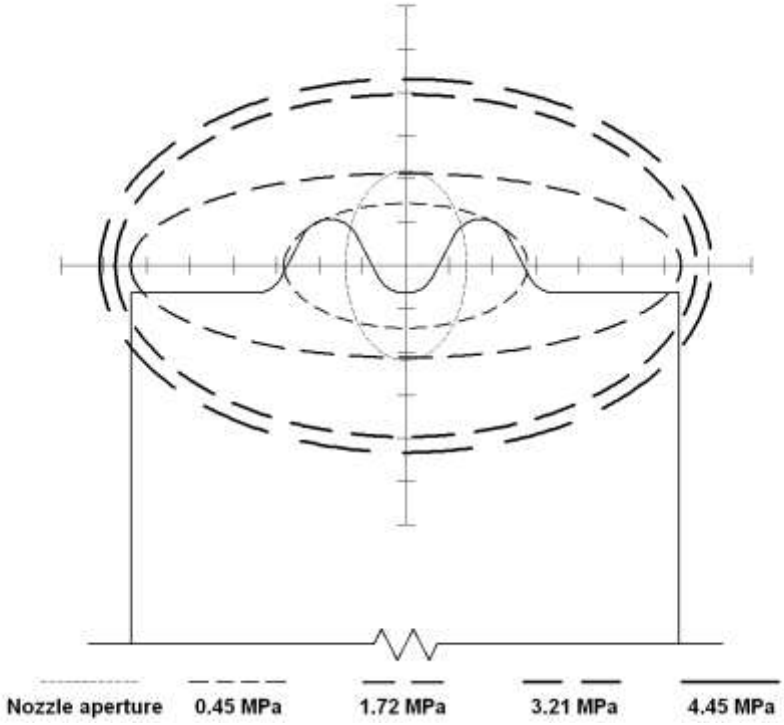

Figure 4.7: Elliptical jet cross-sections 200 mm downstream for various pressures, "horizontal jet orientation".

As with the 3.5 mm diameter circular jet, it was desirable for the elliptical jet to have a variety of widths for the different pressures to be tested in order to determine the impact of fluid distribution on resultant surface finish. Jet width in the horizontal direction at the grinding zone with respect to the jet pressure is plotted in Figure 4.8; a line representing the width of the workpiece is shown at 12.7 mm, illustrating the fact that any flow beyond this limit is wasted.

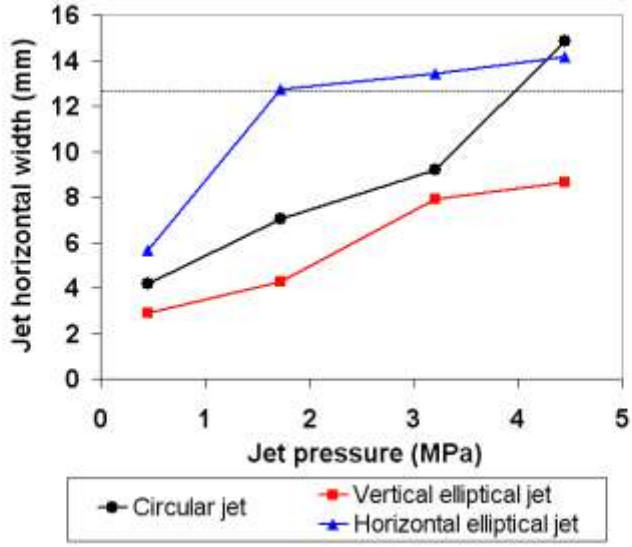

Figure 4.8: Width of the three jets at the grinding zone with respect to jet pressure.

Based on the horizontal jet widths, only the vertically oriented elliptical jet maintains 100% contact with the grinding zone for all pressures tested. The circular jet maintains 100% contact until a pressure 4.45 MPa, but only at 0.45 and 1.72 MPa does the horizontal elliptical jet have full coverage. The percentages of the jet cross section that overlap the grinding zone are plotted in Figure 4.9. Implications of this lack of available fluid will be discussed in the results section to follow in Chapter 5.

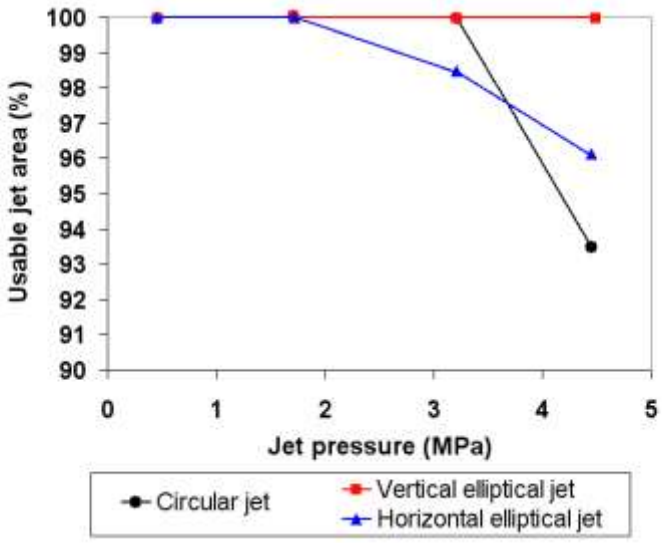

Figure 4.9: Cross-sectional area of various jets available to the grinding zone.

Extensive research by Quinn, Marsters, and Militzer using hot wire anemometry on free jets in air has shown repeatedly that all jets, no matter the initial cross-sectional shape, eventually converge into a circle downstream [2007, 1981, 1995, 2006, 1985, 1989]. With increasing pressure, the rate of convergence is increased. This phenomenon has been explained by the minimization of jet surface area exposed to air resistance—a circle having the largest ratio of volume to surface area of any shape. Results of research conducted here corroborate Quinn's findings to some extent. From the previous figures showing jet expansion with pressure, the theoretical aspect ratio of the various cross-sections can be obtained and are plotted in Figure 4.10.

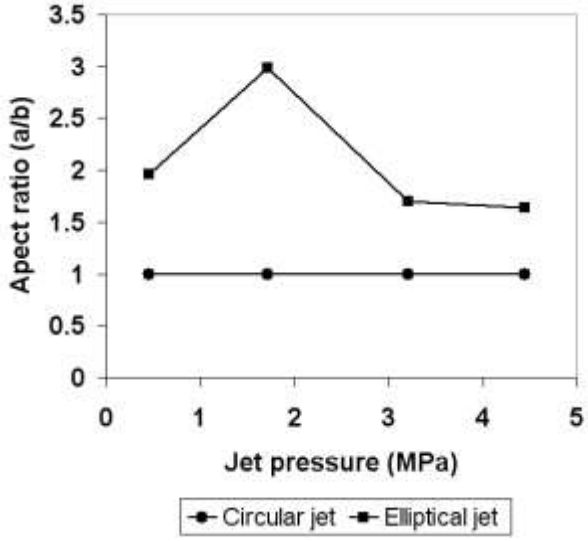

Figure 4.10: Aspect ratio of expanding jet cross-sections.

Repercussions of this trend suggest that elliptical jets at high pressures will perform more similarly to a circular jet than at lower pressures. At 0.45 MPa, the elliptical jet has an aspect ratio 196% that of the circular jet; at 4.45 MPa this relationship is reduced to 164%. The large spike in aspect ratio at 1.72 MPa is likely a product of the complex fluid dynamics occurring in the nozzle and is beyond the scope of this study. Analysis of force, power, and surface finish results in Chapter 5 will use this phenomenon in partial explanation of trends exhibited in the data.

4.2.3 Positioning of Nozzle for Grinding

Once the nozzles were developed, proper positioning of the jet had to be verified. As discussed in Section 2.5.4, research indicates that impingement angle and standoff distance are insignificant factors in determining the effectiveness of the coolant [Irani *et al.* 2005, Hartlen *et al.* 2008, Steffen 2004]. These tests were conducted for circular jets exclusively, but the implications are identical for an elliptical jet. Vertical offset (Figure 4.11), and elliptical orientation (Figure 4.12), however, are variables that must be explored due to the difference in fluid distribution across the cross-section of an ellipse in comparison to a circle.

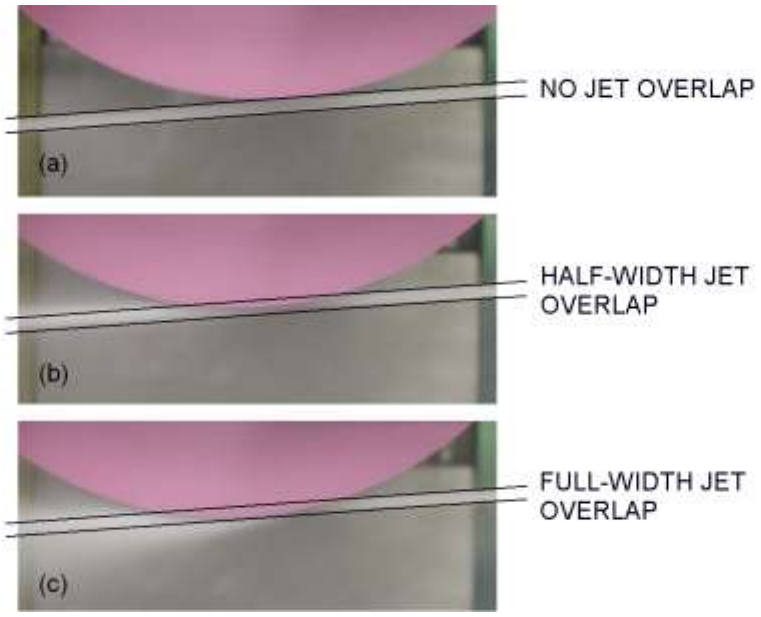

Figure 4.11: Three possible jet vertical offset positions: (a) no overlap, (b) half-width overlap, and (c) full-width overlap.

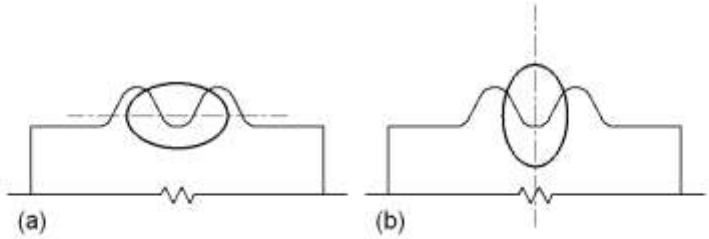

Figure 4.12: Possible elliptical aperture orientations: (a) horizontal nozzle (or "vertical jet") and (b) vertical nozzle (or "horizontal jet").

The general consensus in grinding literature is that a jet centered vertically on the grinding zone, or "nip", provides the most effective cooling and lubrication. The three vertical positions illustrated in Figure 4.11 were tested by performing preliminary creep feed grinding trials with the nozzle oriented both horizontally and vertically. Input grinding parameters for these trials are provided in Table 4, and spindle power readings are graphed in Figure 4.13 (a) and Figure 4.13 (b).

Table 4 – Vertical Offset Grinding Parameters

Parameter	**Value**
Nozzle	Elliptical 3.5 mm equivalent diameter
Nozzle orientation	Horizontal jet (Figure 4.13 (a)) Vertical jet (Figure 4.13 (b))
Coolant pressure	1.72 MPa
Feed rate	150 mm/min
Depth of cut	1.78 mm
Grinding wheel speed	22.35 m/s (4400 ft/min)

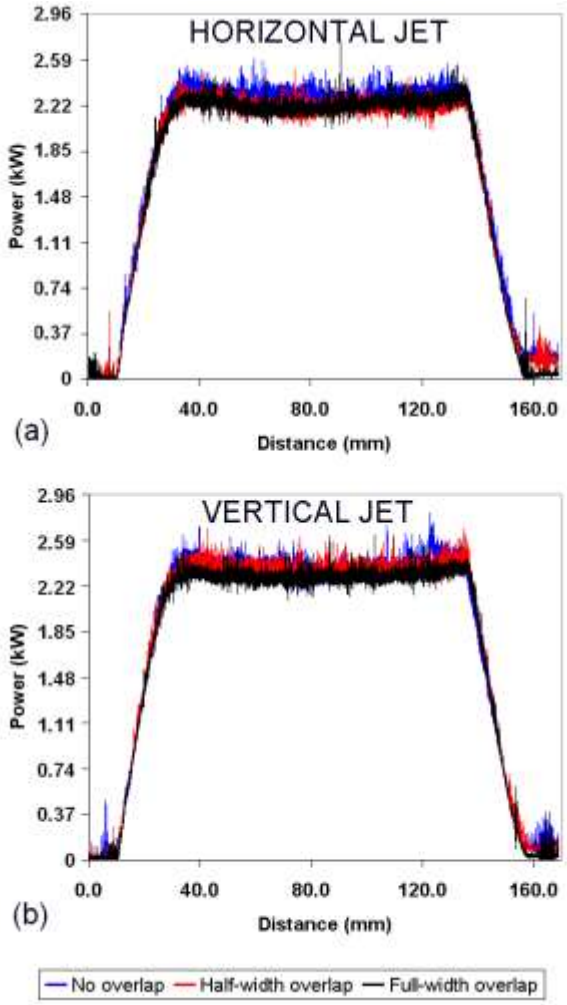

Figure 4.13: Spindle power readings for jet vertical offsets of no overlap, half-width overlap, and full-width overlap, (a) horizontal and (b) vertical jet orientation.

Both the vertical and horizontal jet orientations yielded power traces with remarkable proximity regardless of vertical offset. The vertical offset "no overlap" consistently consumed the largest amount of power, but only by a marginal 6% with respect to full-width overlap. Based on this power analysis, there is no significantly more advantageous choice; therefore, a vertical offset of half-width overlap was selected due to the ease of aiming. An interesting trend was observed: the horizontal jet orientation showed slightly more sensitivity to vertical offset than the vertical jet. This can be attributed to the axis reversal of the jet with respect to the nozzle.

To investigate the final positioning parameter—horizontal or vertical elliptical aperture orientation—both orientations were tested extensively with profiled grinding using three feed rates and four jet pressures; the subject of Chapter 5.

4.3 Experimental Procedure

The experimental parameters—specifically feed rate, coolant nozzle shape, nozzle orientation, and jet pressure—were tested exhaustively by exploring all possible variable combinations. Two nozzles and a total of three possible orientations were tested, each at four flow rates. For each of those twelve combinations therein, three feed rates were tested. This yielded a total of 36 experimental trials to be performed.

In preparation for these trials, numerous preliminary tests were run to explore parameter values based on historic data in order to determine a feasible range for each variable; excessive wheel breakdown, thermal damage incurred on the workpiece, and suggestive power output readings at the spindle denoted when a variable limit had been reached.

The experimental grinding procedure for each trial is outlined as follows:

- Nozzle selected and installed
- Nozzle vertical offset verified
- Workpiece aligned, leveled, and mounted securely in fixture
- Parameters entered into CNC computer
- Grinding wheel brought up to speed
- Cutting fluid pump powered on and adjusted to desired RPM
- Computer data acquisition program initiated
- Grinding program initiated and run to completion
- Computer data acquisition program stopped
- Wheel and workpiece damage inspected and documented
- Workpiece removed from fixture
- Wheel roll-dressed to appropriate depth

After completion of all desired grinding tests, surface measurements were taken across the profile for each workpiece using a Nanovea chromatic confocal optical profilometer, the details of which are presented in Table 5. The measurement procedure can be outlined as follows:

- Custom fixture attached to profilometer stage
- Workpiece mounted in fixture (See photograph in Figure 4.14)
- Optical pen aligned with location of measurements
    - Three measurements taken:
        - within 5 mm of full wheel engagement (30 mm)
        - middle of cut (80 mm)
        - within 5 mm prior to loss of full wheel engagement (120 mm)
- Two measurements* taken at each of the three locations (*See note below)
- Measurements repeated once to obtain an average at each location
- Each profile returned to profilometry software for leveling and analysis

Table 5 – Surface Measurement Equipment

Component	Make and Model
Profilometer	Nanovea: PS 50, Chromatic Confocal Optical Profilometer
Profilometer Controller	CHR 150
Optical Pen	1.2 mm
Acquisition Program	Nanovea 3D
Analysis Program	Mountains 3D

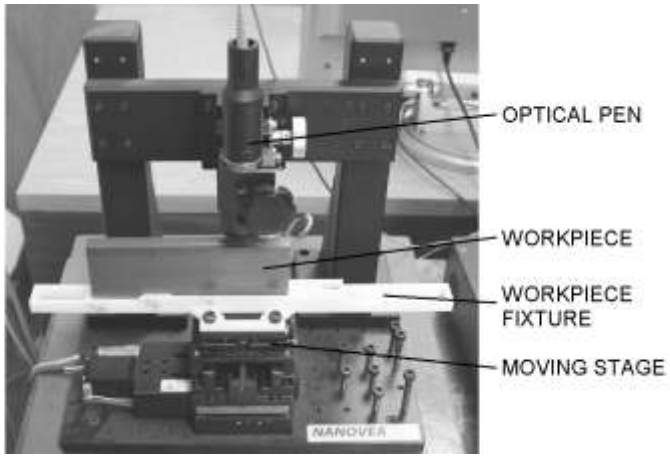

Figure 4.14: Photograph of workpiece mounted in profilometer.

*Note: “Upper” and “lower” measurements were taken across the profile at each location because the optical pen had a measurable height range of 1.2 mm but the profile was 1.7 mm in height. “Upper” measured the upper 1 – 1.2 mm of the profile, while “lower” measured the lower 1 – 1.2 mm of the profile. These two readings were then superimposed in Excel to form a complete measurement of the workpiece profile. Averaging several points within the shared upper and lower domains allowed for highly accurate translation of both curves into the final complete profile. This process is illustrated visually in Figure 4.15.

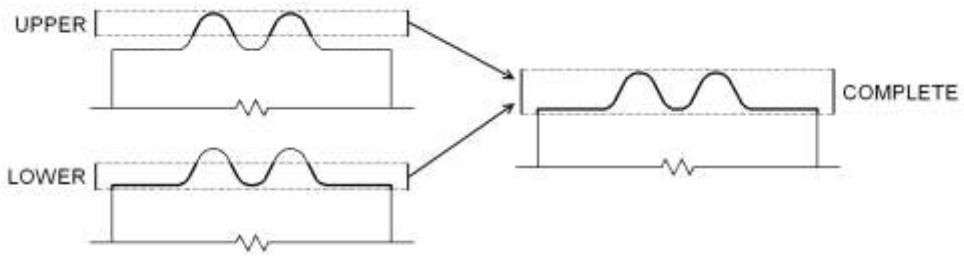

Figure 4.15: Combination of “upper” and “lower” profile measurements.

After three full profiles were obtained for each of 36 workpieces, all profiles were then aligned in MATLAB using a purpose-built curve-matching algorithm. From these aligned profile curves, the data presented in the following chapter was obtained.

4.4 Experimental Preparation Summary

Hitherto unexplored, the application of carefully designed elliptical nozzles in creep feed grinding is now possible. A range of industry-standard cutting, dressing, and fluid application parameters was selected and validated, and taken in conjunction with the new nozzles fabricated specifically for this research, an investigation into which parameter—be it jet shape, nozzle orientation, jet pressure, jet coverage, or grinding feed rate—wields the most influence over workpiece finish was undertaken.

CHAPTER 5 EXPERIMENTAL RESULTS AND DISCUSSION

This chapter presents the findings of experimental work conducted to investigate the influence of various grinding and coolant application parameters on workpiece surface finish. Two major categories of analysis were performed, surface finish and power. Section 5.1 describes surface finish measurements and related analysis such as allowable tolerances. Section 5.2 then discusses the results of power readings taken at the spindle during the various experimental trials and correlates them with surface finish data to develop a measure of the overall cutting quality and efficiency in terms of productivity. Further to the power results, grinding forces can be used for corroboration and additional analysis; these are presented and discussed in Section 5.3. Section 5.4 concludes with a summary of trends and explanations.

5.1 Surface Finish

The surfaces of ground workpieces were measured in three places along their length to obtain an average form error and a roughness value. Section 5.1.1 introduces the analytical process applied to these profile measurements. The results are then presented and interpreted in Section 5.1.2.

5.1.1 Introduction to Surface Finish Measurements

Mated raw data obtained from the profilometer had to cleaned and prepared in several steps in order to begin analysis. First, the raw data was imported to the profilometer analysis software for leveling. By manually selecting the flat 2 mm wide regions on either edge of the profile, a leveling algorithm native to the software was able to average the selected data and obtain a trend line. The angle of this line with respect to horizontal was then used to geometrically translate and rotate the entire data set accordingly.

Once leveled, the profiles were then horizontally aligned using the method summarized for a sample curve in Figure 5.1. The local minimum between 5.5 mm and 6.5 mm on the profile was fit to a parabolic trend line; the local minima of all profiles were aligned with 6.0 mm.

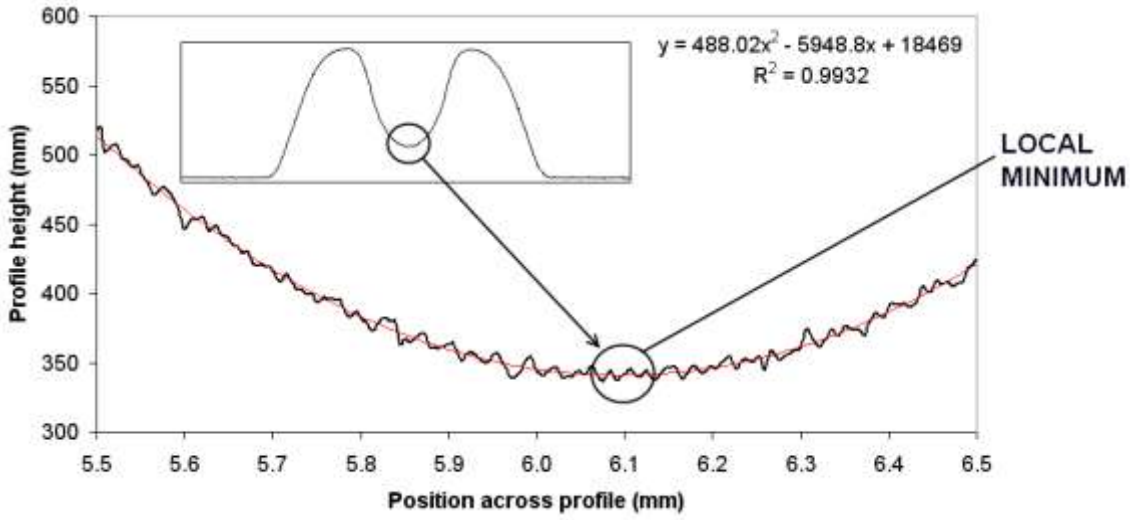

Figure 5.1: Parabola involved in horizontally aligning profile curves.

Before analysis could occur, a datum "desired" profile curve had to be obtained. Acquiring the datum involved assuming the smoothest and most accurately finished workpiece surface occurred immediately after full engagement with the wheel occurred; the grinding wheel is at its sharpest, cutting fluid has unobstructed access to the grinding zone, and the workpiece has not been heated. As such, the surface measurements obtained within the first 5 mm of full wheel engagement on each workpiece that did not instantly burn were averaged to obtain the datum profile curve. Vertical alignment of these profiles was done in Excel by averaging both 2 mm wide flat regions on either side of the profile and appropriately translating the curves—a process made possible by the accuracy of these initial profiles. Finally, a moving average algorithm was employed in MATLAB to smooth out high frequency fluctuations in the dataset.

Horizontally aligned and leveled with respect to horizontal, the profile curves were then ready for import to a purpose-built MATLAB program previously developed for Hartlen *et al.* [2008]. This program vertically translated the profiles, effectively minimizing the total error between the profile measurement and the datum. The error formula to be minimized is defined as:

$$Error = \frac{1}{n}\sqrt{\sum_{i=0}^{n} |y - y_i|^2} \tag{5.1}$$

Where n is the size of the dataset, y is the height of the datum and y_i is the height of the profile being tested. MATLAB plots such as that in Figure 5.2 were then produced, super-imposing the measured profile and the datum in addition to the available cutting fluid at the grinding zone in terms of flow rate per unit width. Using these plots, the location and scale of form error due to wheel breakdown could easily be observed and quantified.

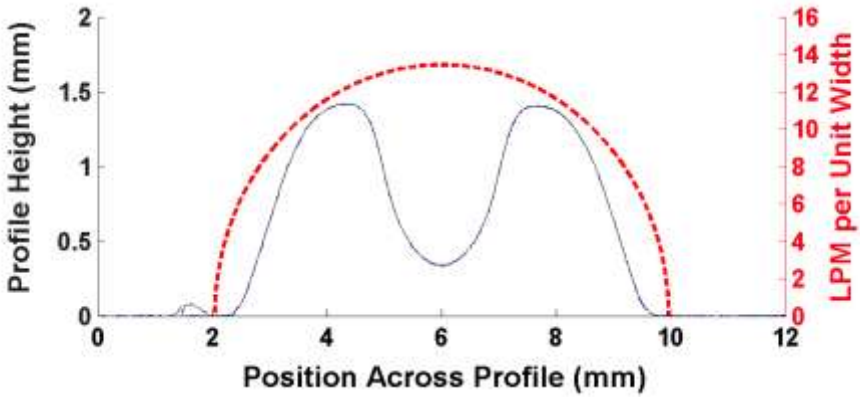

Figure 5.2: Desired profile and profile error in comparison to available fluid flow.

It is important to note that the line indicating available fluid flow to the grinding zone is not representative of the shape of the jet impacting the grinding zone, rather, it is the LPM of cutting fluid per unit width available to the grinding zone. For the higher pressure horizontal elliptical aperture trials and the highest circular aperture trial, the core of the jet exceeded the width of the grinding zone and was therefore not available flow, but the remainder of the experiments had 100% of the cutting fluid jet impacting the grinding zone. In addition to superposition of the fluid flow and the profile with the datum, MATLAB analysis displayed the profile error as calculated by:

$$Profile\ error = \sqrt{|y - y_i|^2} \tag{5.2}$$

Where y is the height of the datum and y_i is the height of the profile being tested. Profile error was graphed in plots such as that of Figure 5.3, which shows the form error of the profile being analyzed in Figure 5.2.

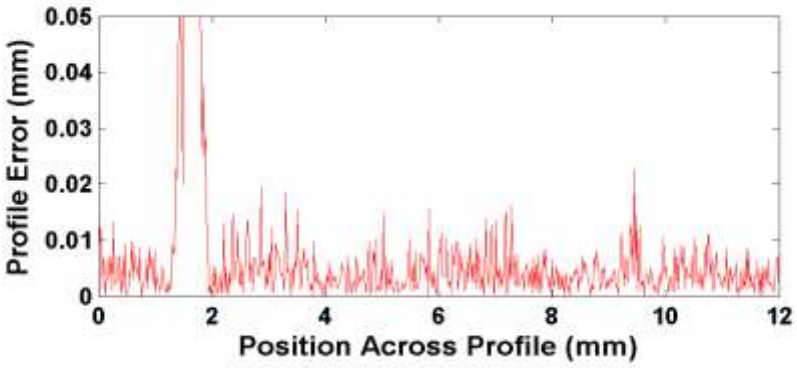

Figure 5.3: Form error between measured profile and desired profile.

The region of wheel breakdown at approximately 1.9 mm can be seen as a large spike in the profile error, well above the displayed 0.05 mm (50 μm) upper limit. This limit on the scale was chosen to keep acceptable error visible within the plot; form error above 0.05 mm is unacceptable and unnecessary to show.

An averaged profile form error was chosen as the single value to represent the form error of each profile curve. Additionally, the workpiece surface finish quality in terms comparable to industry standards was calculated by subtracting the datum profile from the tested profile, leaving behind the surface roughness without the overall profile contours. The average of the absolute values of this resultant data set can be referred to as R_a:

$$R_a = \frac{1}{n} \sum_{i=1}^{n} |y_i| \tag{5.3}$$

where n is the number of samples and y_i is the value of each. For creep feed grinding using feed rates between 100 and 200 mm/min, an R_a value of approximately 3.5 μm is considered the upper limit of a satisfactory finish [Sedighi and Afshari 2010]. Note that grinding utilizing a high depth of cut is not generally intended to be a finishing operation, rather, the focus is rapid material removal with minimal thermal damage.

5.1.2 Surface Finish Results

Several major trends were observed in the surface roughness as the grinding parameters were modified: wheel breakdown along the length of the workpiece, an increase in roughness with decreased jet pressure, an increase in roughness with feed rate, and slight changes in roughness depending on the aperture used.

As expected, wheel breakdown—and the resultant profile form error—increased along the length of the workpiece. A prime example of this increasing form error can be seen in the progression along the workpiece illustrated in Figure 5.4. From the measurement taken 30 mm after the beginning of the workpiece, an average profile form error of 3.5 μm was observed. At 80 mm, the average error had increased to 5.4 μm with error being propagated in the regions of high depth of cut and in the sharp corners of the profile. By the end of cutting at 115 mm, the wheel had broken down in excess of 50 μm in the regions of highest depth of cut. This dramatic wheel breakdown is understandable given the rapid feed and starvation of fluid, 200 mm/min and a pressure of 0.45 MPa issuing from a circular nozzle, respectively.

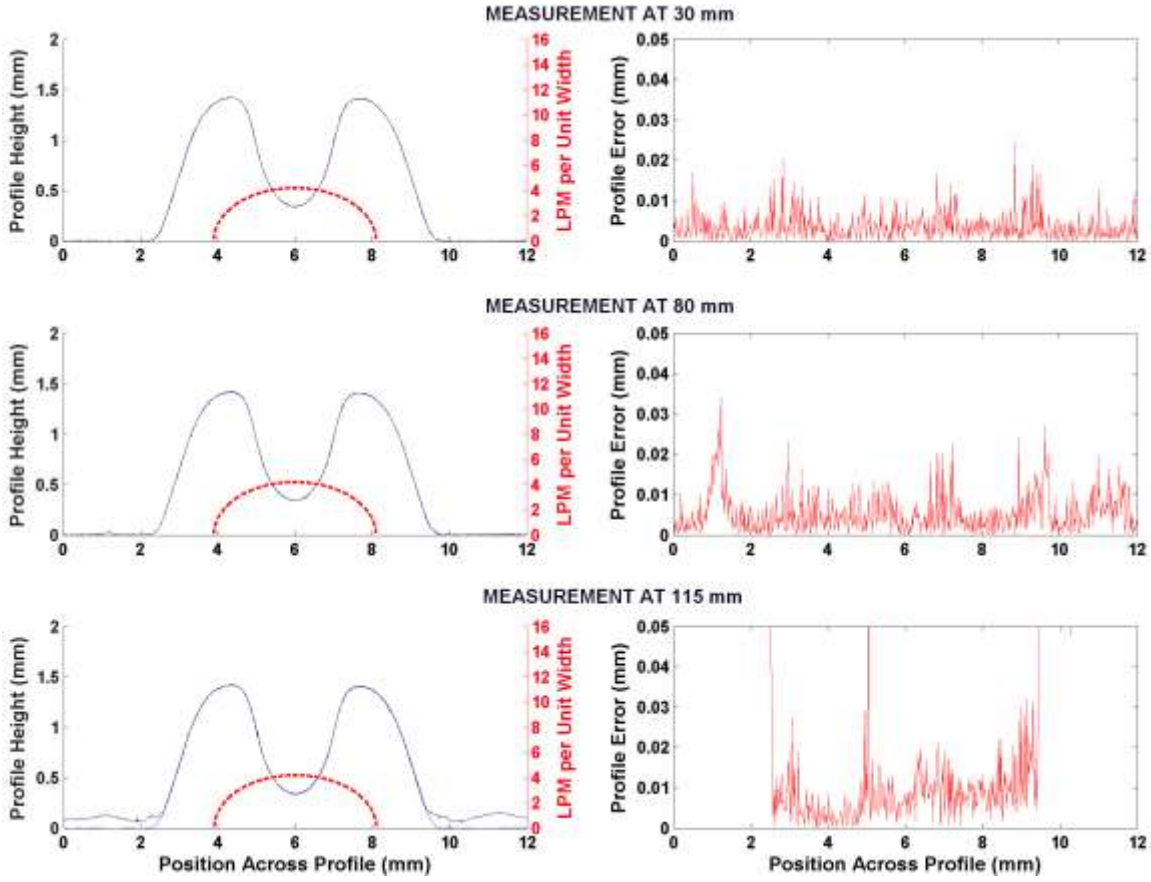

Figure 5.4: Measured and desired profiles, available fluid flow, and form error as measured at three positions along the length of a sample workpiece, circular nozzle.

The trend of wheel breakdown occurring in the sharpest corners of the profile was observed in numerous experimental trials. This is understandable given that the grits of the wheel will be the most exposed at convex corners. Propagation of breakdown from these regions is rapid and dramatic: of the 36 experimental trials, 17 experienced excessive profile error due to wheel breakdown, and of these 8 began in the corners of the profile. Profile and profile form error measurements displaying this trend of breakdown in the corners are illustrated for another sample in Figure 5.5. The grinding parameters used were a feed rate of 200 mm/min, a jet pressure of 1.72 MPa, and the horizontal elliptical jet.

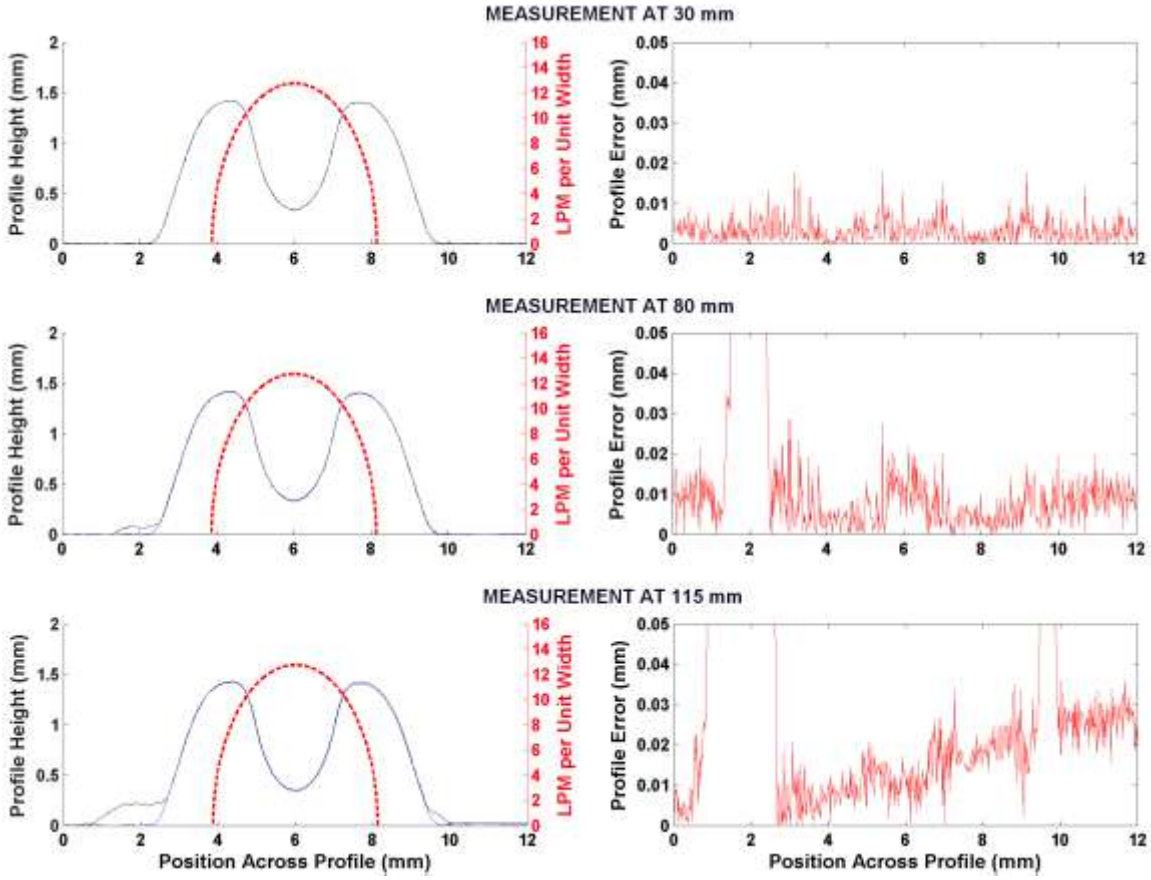

Figure 5.5: Wheel breakdown in the corners of the profile, leading to propagation of profile form error, horizontal elliptical jet orientation.

Wheel breakdown is a highly chaotic process. Grains and bonding material are fractured and removed in an unpredictable way, yielding a surface finish difficult to reconcile with samples where breakdown did not occur. Removing data points where wheel breakdown caused an unacceptable surface finish allows for more accurate interpretation of the results. By removing unacceptable trials, the typical propagation of form error along the length of a workpiece is summarized in Figure 5.6. The three nozzle aperture orientations are shown in the three plots; within each plot is the collection of form error data points collected for all feeds. Various tested jet pressures are not distinguished.

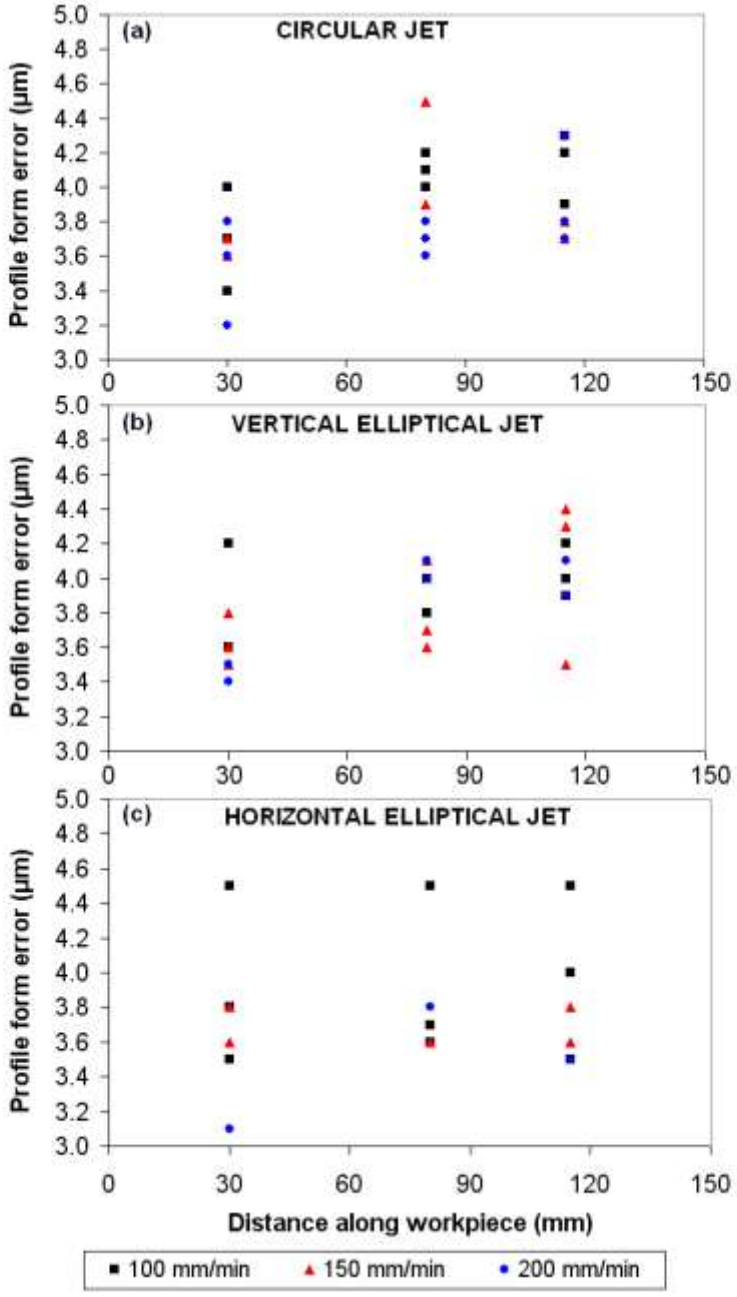

Figure 5.6: Summary of form error propagation along the length of the workpiece for all jet pressures, feed rates, and jet orientations; trials with wheel breakdown removed.

This method of presentation does not yield statistically valid trend lines to describe form error for groupings of trials performed at the various jet pressure values or feed rates; rather, it illustrates the overall trend of increasing form error with distance along the

workpiece. A direct result of wheel breakdown, this phenomenon is corroborated through power and force analysis.

In addition to form error, the surface roughness R_a is also a useful measure in determining the quality of a surface finish. A summary of experimental averaged R_a values obtained is provided in Figure 5.7; the three tested feed rates are shown in three separate plots, with jet orientation and jet pressure detailed in each. For each data point plotted, the uncertainty as a result of averaging yielded standard deviations between 2 and 20%. A line indicating an acceptable surface finish is also indicated on the plots at an R_a value of 3.5 μm.

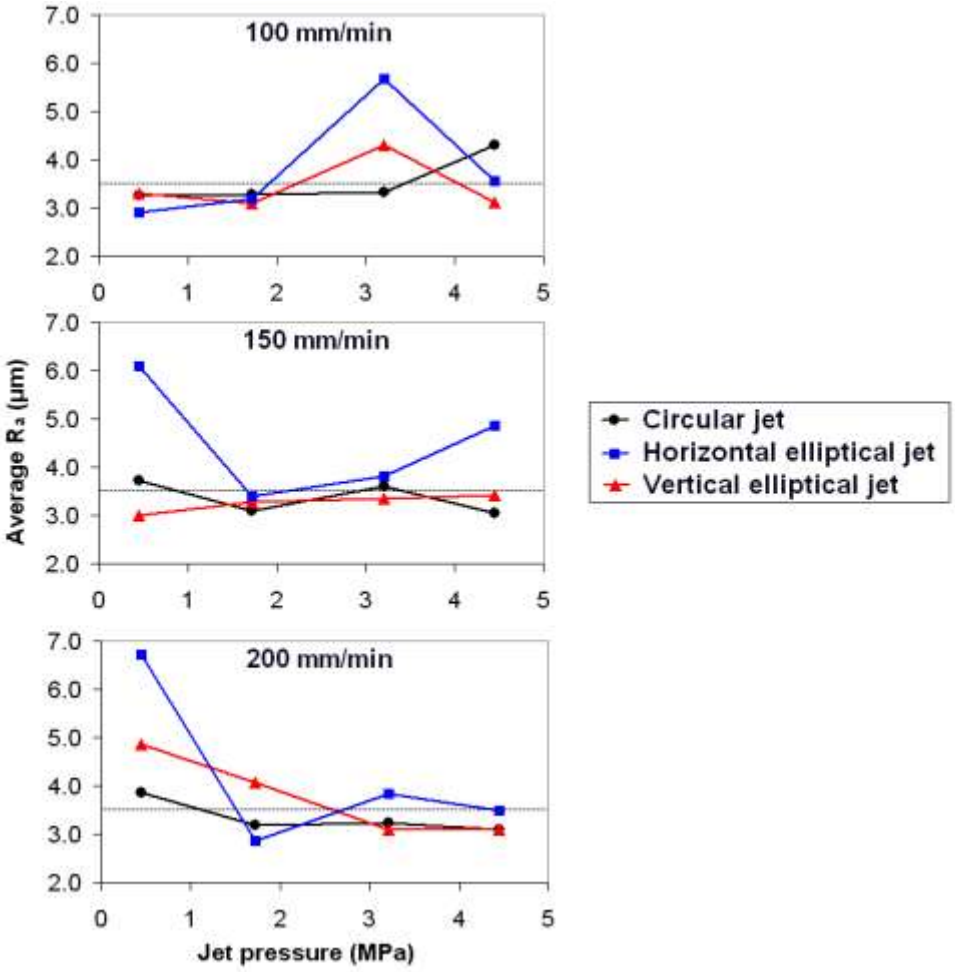

Figure 5.7: Summary of experimental averaged surface roughness values for all jet pressures, feed rates, and jet orientations, including all trials with wheel breakdown.

Several trends are apparent in this figure. First, increasing the feed causes a slight overall increase in surface roughness; the chaotic effects of wheel breakdown on surface finish are exaggerated at higher feeds. Second, increasing the jet pressure improves the chance of achieving a satisfactory surface roughness. At feed rates of 150 and 200 mm/min using a jet pressure of 0.45 MPa, wheel break down is most likely to occur. As discussed, wheel breakdown is a highly chaotic process. Removing the data samples where wheel breakdown occurred yields the results shown in Figure 5.8. Plotting both sets of data gives perspective to the chaotic nature of wheel breakdown.

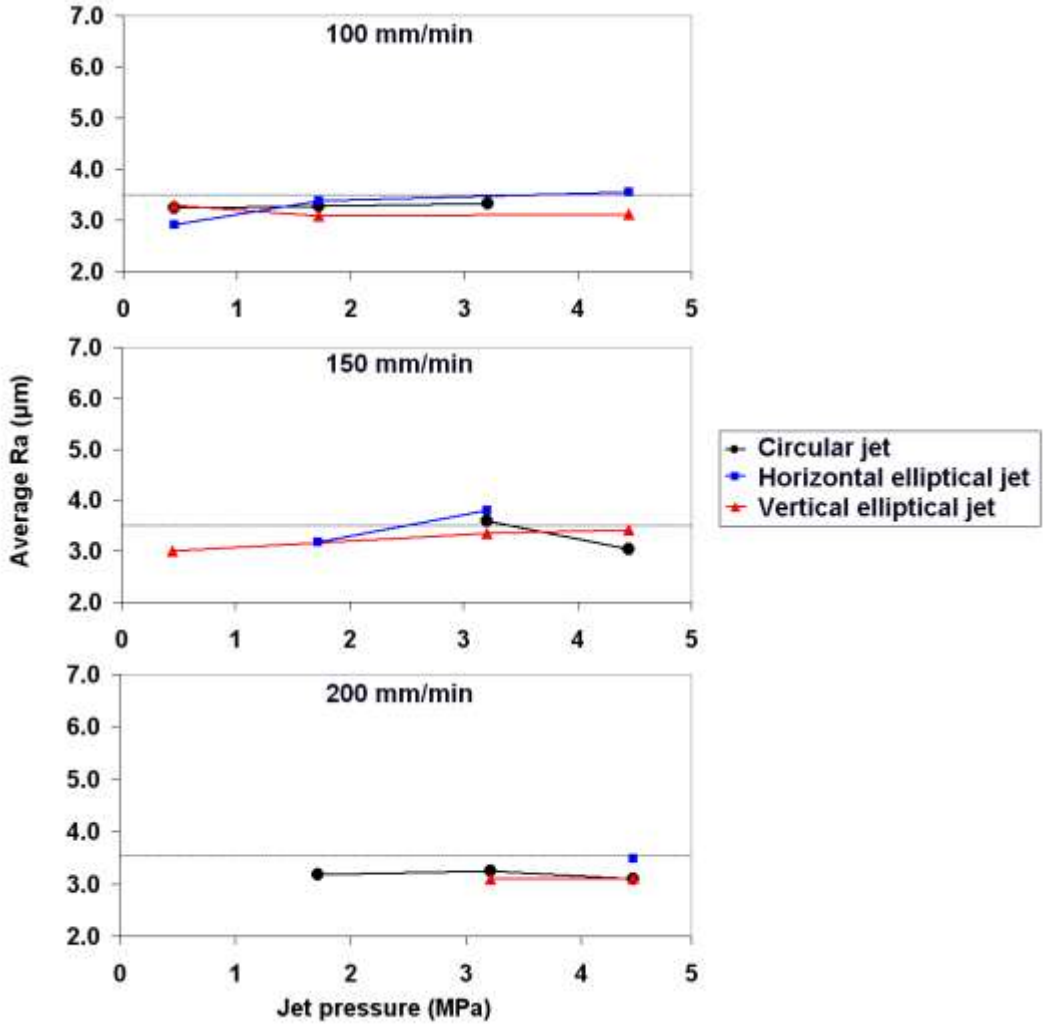

Figure 5.8: Summary of experimental averaged surface roughness values for all jet pressures, feed rates, and jet orientations, trials with wheel breakdown removed.

With interference from wheel breakdown removed, the data lies almost exclusively below the 3.5 μm limit of acceptable roughness, with only the horizontal elliptical jet rising above. Data missing from these plots tell as much of a story as the data in the plots, however: use of the horizontal jet resulted in wheel breakdown in half of all experiments performed at a feed rate of 150 mm/min, and all experiments performed at 200 mm/min with the exception of the trial using the highest jet pressure. This fact would seem to indicate a less efficient distribution of cutting fluid using this orientation. The vertical elliptical jet, on the other hand, resulted in surface finished of equal or marginally better quality than the circular jet—no more than 7% discrepancy existed for any trial. Both the vertical elliptical jet and the circular jet were able to perform satisfactorily for 8 of their respective 12 tests, whereas the horizontal jet succeeded 6 times. Interestingly, the horizontal jet yielded a better surface finish at the lowest feed and jet pressure. This observation, taken in conjunction with the knowledge that lower-pressure jets are better able to maintain their cross-sectional shape due to proportionally stronger surface tension and cohesion, suggests that jet shape does indeed have a minor influence on the grind quality when low cutting fluid jet pressure is utilized.

Finally, there appears to be a trend in the data that as jet pressure increases, the variously shaped and oriented nozzles perform more similarly, negating the influence of shape on surface finish. Assuming this to be the case, it can be explained by the fact that as jet pressure increases, the elliptical jet begins to approach a circular cross-section due to conservation of momentum and the fact that air resistance is minimized for a circular profile. Increasing the jet pressure from 0.45 to 4.45 MPa yields a 32% convergence in the aspect ratio of the elliptical jet toward that of the circular jet—that is, 1.0. A comparably large, statistically significant convergence is apparent in Figure 5.7 in the form of an increased number of acceptable surface finishes achieved at the higher pressures: at 0.45 MPa, 4 of 9 trials were successful; at 4.45 MPa, 7 of 9. Using a higher pressure jet has numerous benefits, a combination of which is likely responsible for the observed behavior, such as improved cleaning of wheel pores, more fluid passing through the cutting zone, and improved swarf removal.

Varying the aperture shape and orientation cannot be otherwise shown conclusively to have a significant influence on the workpiece surface finish. As seen in Figure 5.7 and Figure 5.8, the circular nozzle and elliptical jet oriented vertically appear to perform marginally better than the horizontal elliptical jet. Recalling the phenomenon of axis reversal for elliptical nozzles—that is, the jet diverges in the minor axis of the aperture—this trend appears to be counter-intuitive. Jet divergence in the vertical direction as a result of a horizontally-oriented elliptical aperture does not yield an impact coverage area that envelops the grinding zone, as illustrated schematically in Figure 5.9. However, 100% of the flow is available to the grinding zone when using a vertically oriented elliptical jet, as compared to between 93 and 96% for the circular and horizontal jets, respectively. This suggests that available flow is a more influential factor in surface finish than fluid coverage distribution, as previously hypothesized.

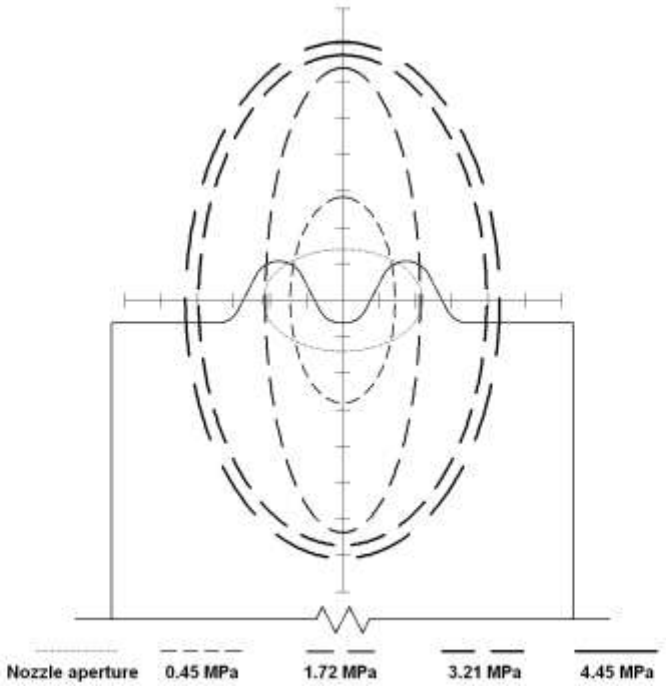

Figure 5.9: Horizontal elliptical nozzle and resultant vertical jet superimposed over the grinding zone to show approximate coverage area.

As discussed in previous chapters, the fluid distribution of the vertical elliptical jet allows the entire flow to impact the core of the profile, whereas the circular jet spreads the same

volume of cutting fluid across the entire grinding zone and beyond the edges, theoretically reducing the available fluid by up to 11% as illustrated in the plot of available fluid percentages in Figure 4.9 of the previous chapter. While not directly impacting the entirety of the grinding zone, the vertical elliptical jet takes advantage of the natural "sheeting" phenomenon of a jet impacting a surface with a low angle of incidence, thereby theoretically spreading 100% of the flow across the grinding zone.

5.2 Power Output

Section 5.2.1 discusses the type of cleaning and preparation required in order to effectively interpret power readings taken at the spindle during grinding. The products of this preparation yield results which are presented in Section 5.2.2 along with relevant discussion.

5.2.1 Power Output Data Manipulation

Energy consumed during the cutting process can be interpreted in numerous ways; average power, total power, specific energy, with respect to removal rate, or with respect to critical specific material removal rate. For the purposes of this research, the total consumed power and the average power were chosen to illustrate the performance of various jet and grinding parameters. Total consumed power will be defined as the total area under the power curve from the moment wheel engagement begins with the workpiece until the moment the wheel is completely disengaged. These points are illustrated schematically in Figure 5.10 as (a) and (d) for a sample power curve. The average power will be defined as the average of the power being used during the period of full wheel engagement in the workpiece. The limits of this range are shown as point (b) and (c).

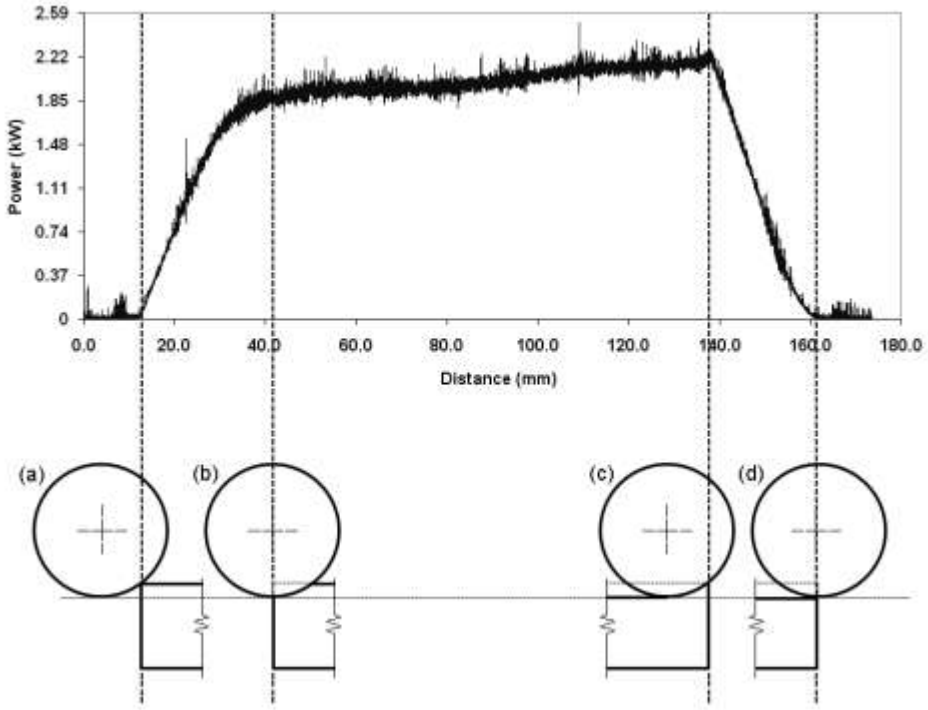

Figure 5.10: Locations of the grinding wheel with respect to critical points on a power trace.

Validation for using the total power consumed as a descriptor of power usage lies in the fact that resources are being spent. Only during the portion of the cutting process when the wheel is fully engaged and the maximum contact length is being utilized—that is, between points (b) and (c) in Figure 5.10—will a satisfactory surface finish be possible and predictable. However, resources are being consumed during all wheel-workpiece interaction. Apparent consumed resources include power and tool integrity, but workpiece material is being lost, the temperature of the grinding interface is rising, and finally, time is being spent.

Using an average cutting power as another descriptor will be useful in other respects, namely, finding the power limit for an acceptable surface finish in an effort to increase productivity. Productivity is defined simply as the amount of material removed with respect to time; a faster process is a more productive process. Increasing the feed rate is the simplest way to achieve higher productivity when increasing cut depth is not an option. The disadvantage of a higher feed rate is an increased risk of thermal damage or

wheel breakdown, results which can ruin the surface finish of a workpiece. These forms of damage can be seen in the cutting power curves, and therefore, can be avoided through parameter optimization: feed rate is increased to the maximum point above which workpiece burn or wheel breakdown is known to occur. Changing the jet parameters—such as pressure or flow rate—has the potential to allow for even higher feeds, as will be observed in the following sections.

5.2.2 Power Output Results

The real-time power traces as measured at the spindle for each of the three feed rates tested, four jet pressures, and three nozzle orientations are shown with respect to position on the workpiece in Figure 5.11 through Figure 5.13. Within each figure, data taken using a circular jet of fluid is denoted by a black trace, a vertical elliptical jet by a red trace, and a horizontal elliptical jet by a blue trace. The figures also illustrate power behavior as a result of increasing the jet pressure; specific pressure values can be seen circled in the groupings of the various power traces, as indicated appropriately on each figure.

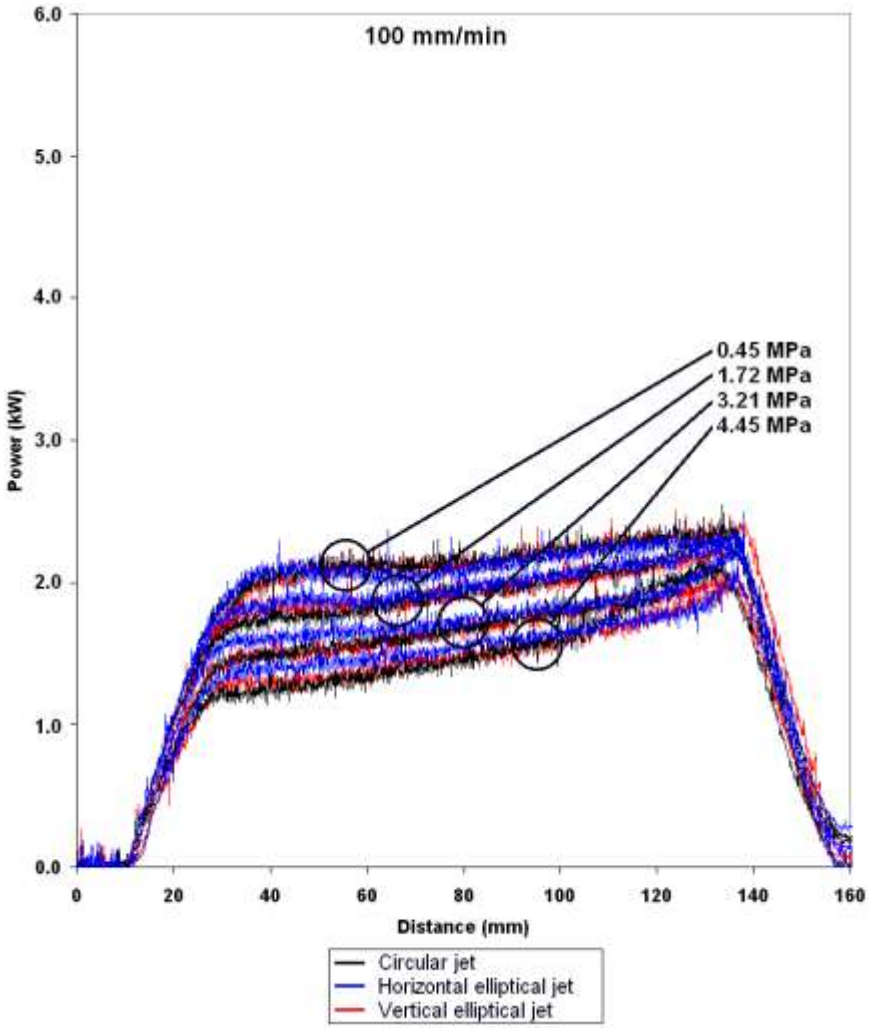

Figure 5.11: Summary of power consumption values for all experiments that used a feed rate of 100 mm/min.

The close proximity—discrepancy always within 7%—of elliptical and circular jet trials using the same jet pressure indicate that aperture shape has an insignificant effect on the overall power used during creep feed grinding at a feed rate of 100 mm/min, as seen in Figure 5.11. Changes in jet pressure, on the other hand, cause dramatic changes in the rate of power consumption, as denoted by the four distinct bands of grouped power curves. All the power curves have relatively low positive slopes, indicating a low rate of tool and workpiece wear is occurring; a standard phenomenon witnessed in creep feed grinding. These characteristics of the illustrated power curves imply that a satisfactory

surface finish and cutting efficiency are likely being achieved across this range of parameters.

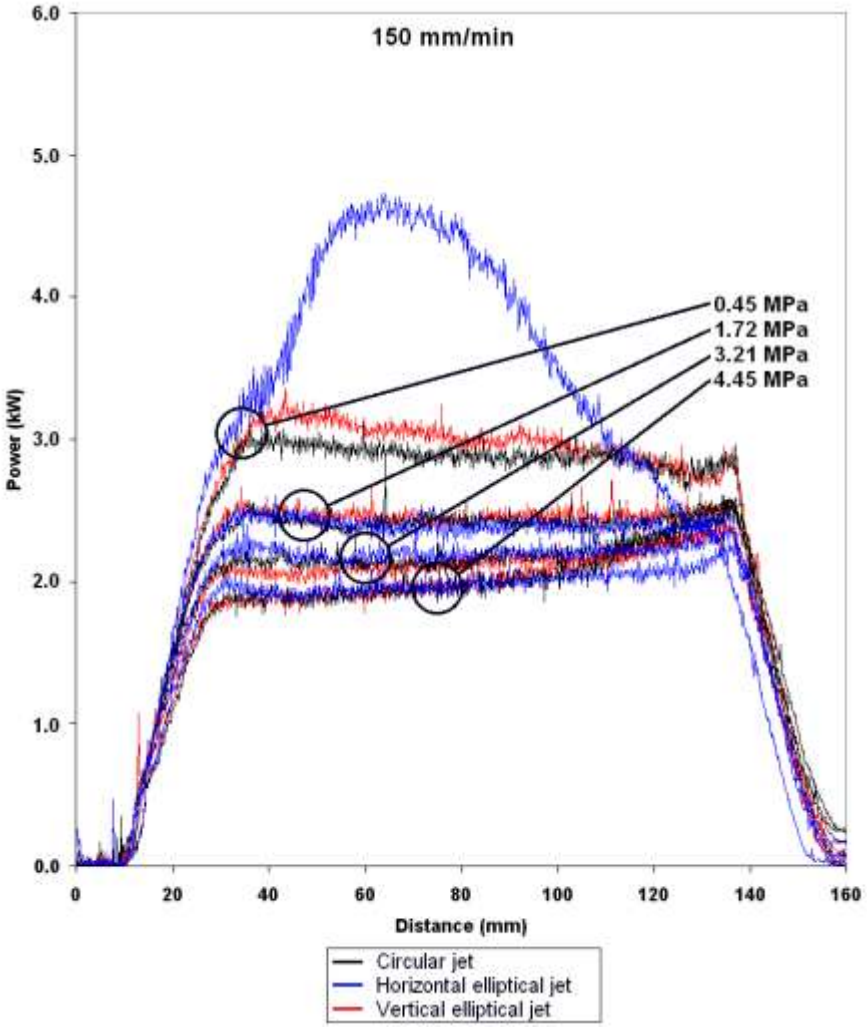

Figure 5.12: Summary of power consumption values for all experiments that used a feed rate of 150 mm/min.

Compared to those at 100 mm/min, a feed rate of 150 mm/min causes larger—but still relatively insignificant—discrepancies between consumed power levels at different jet pressures, as seen in Figure 5.12. The elliptical and circular jet curves are aligned with a maximum of 8% difference; an exception being a burn spike—a sudden spike in power resultant from a sudden increase in grinding forces and indicative of workpiece burn—occurring at the lowest jet pressure of 0.45 MPa. The total power consumed for these

trials is on average 110% that consumed at 100 mm/min. The power curves of the two higher jet pressures, 3.21 and 4.45 MPa, show slight positive slopes, indicative of normal creep feed grinding dynamics. The curves at a jet pressure of 1.72 MPa however, show slight negative slopes, indicative of wheel breakdown as a direct result of insufficient cutting fluid reaching the grinding zone. The lowest jet pressure of a horizontal elliptical jet, however, causes burn instantly and subsequent dramatic wheel breakdown. At this feed rate, a lower cutting efficiency and poorer quality surface finish can be expected.

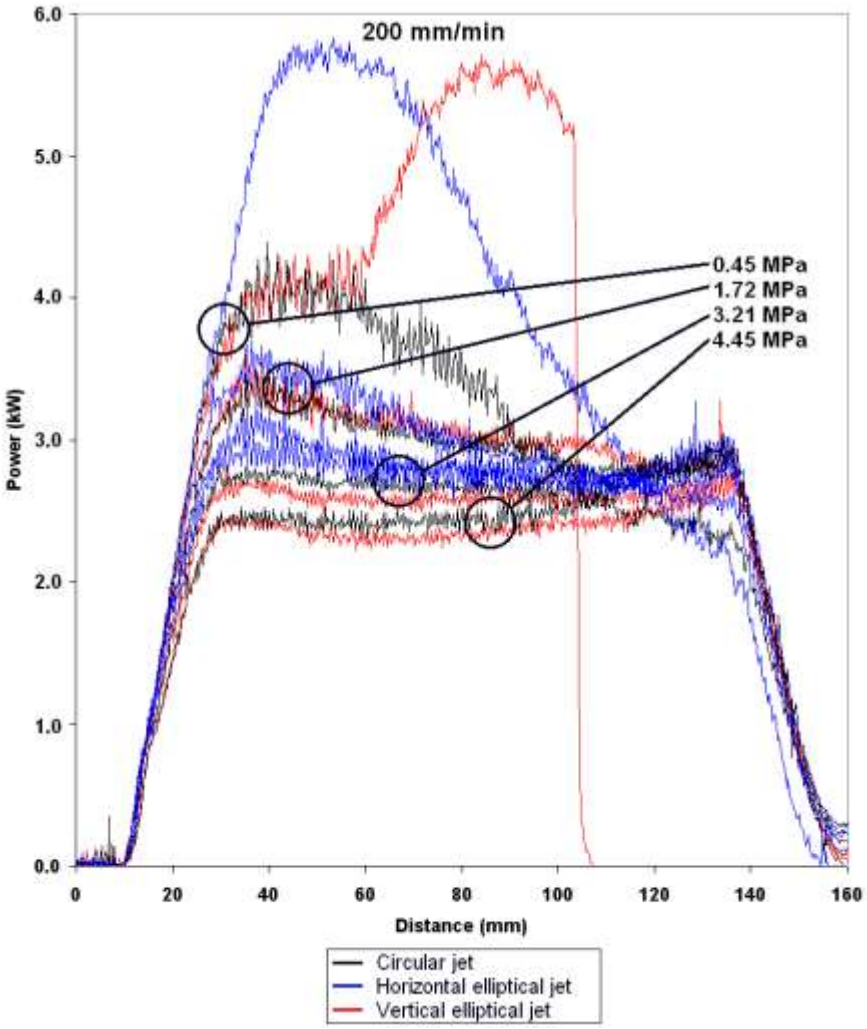

Figure 5.13: Summary of power consumption values for all experiments that used a feed rate of 200 mm/min.

The power behavior for all tests conducted using a feed of 200 mm/min is shown in Figure 5.13. The largest discrepancies between trials conducted at various jet pressures and with various jet orientations can be observed at this feed rate. For example, in the power traces for both elliptical nozzles at 0.45 MPa, large power spikes followed by steep declines indicate severe workpiece burn followed by wheel breakdown. This is in contrast to the power trace of the circular jet, which shows only wheel breakdown. Implications are that at extremely low jet pressures the circular nozzle is capable of delivering cutting fluid more appropriately to the areas of the profile in need of lubrication, while both elliptical nozzles prove insufficient. Indeed, Figure 5.12 can be used to corroborate this hypothesis. The circular jet and vertical jet at 0.45 MPa show only wheel breakdown, while the horizontal elliptical jet shows wheel breakdown preceded by an immediate burn spike. All jet pressures except 4.45 MPa show wheel breakdown at some point during the grind for this feed rate; therefore, the choice to use 200 mm/min risks shortening the life span of the grinding wheel in exchange for higher productivity.

To summarize the power behavior of each of these experimental trials, the following figure plots total consumed power against the jet pressure used for each; the feed rates are shown in separate graphs. Various jet orientations are indicated by black, blue and red lines for the circular, horizontal elliptical and vertical elliptical jets, respectively.

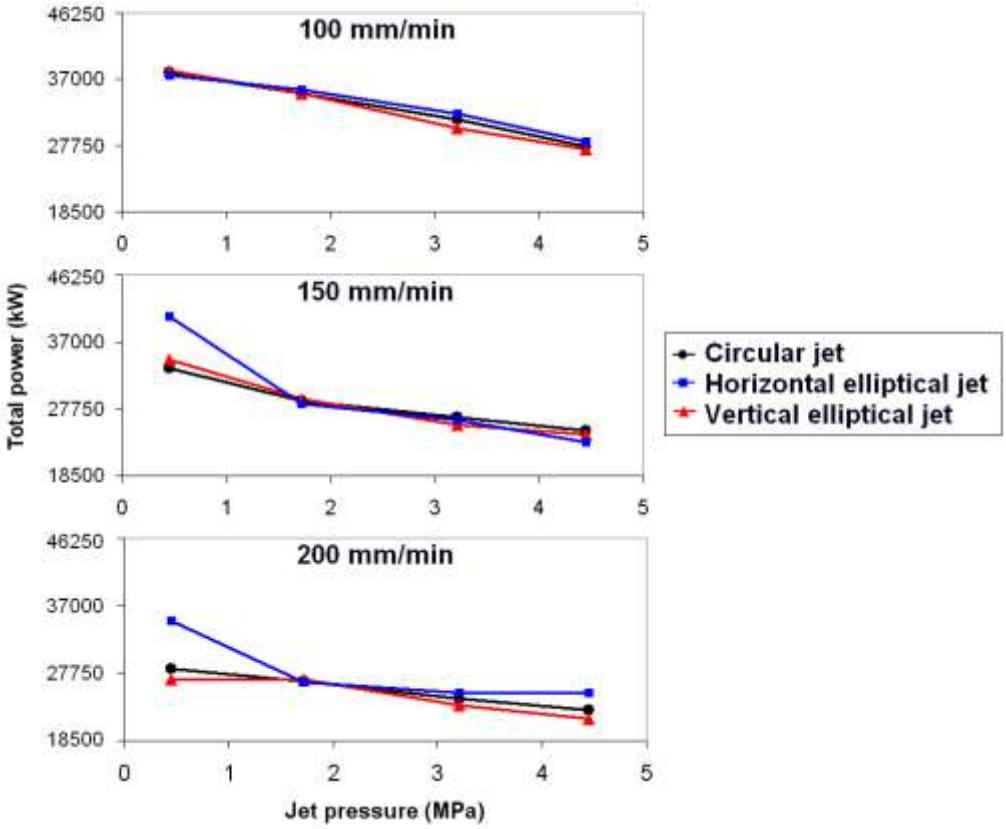

Figure 5.14: Summary of total consumed power values for all jet pressures, feed rates, and jet orientations, including trials where wheel breakdown occurred.

As with surface finish, there are outliers in this figure caused by wheel breakdown; removing these points leads to the data presented in Figure 5.15.

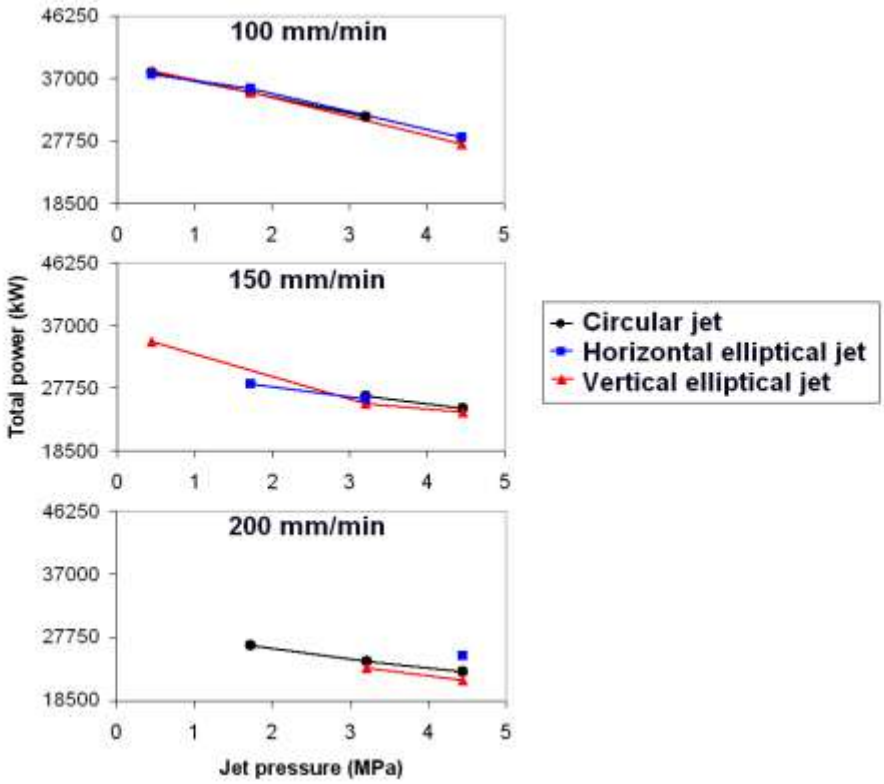

Figure 5.15: Summary of total consumed power values for all jet pressures, feed rates, and jet orientations, trials where wheel breakdown occurred removed.

Several trends are apparent from the summarized power data in Figure 5.14 and Figure 5.15. First, higher feeds cause more frequent wheel breakdown, with only the highest pressure jets capable of delivering sufficient cutting fluid. Second, all three jet orientations appear to cause similar power behavior; increasingly so for higher pressure. As jet pressure increases, all free jets regardless of initial shape begin to approach a circular cross-section to minimize the surface area exposed to mixing with the surrounding media, so this power behavior is understandable. Third, as the jet pressure increases, the total power consumed by the grinding wheel is reduced; a 25% reduction in total power consumed is observed from 100 mm/min to 200 mm/min. This ability to reduce power through coolant application is advantageous if cutting efficiency with respect to power used per unit of material removed is of importance to a part producer, however, it does not speak to the optimization of grinding parameters. To identify which feed rate and jet pressure allows maximum productivity without burn, the average power

being used during the cutting process must be analyzed. A summary of these average cutting powers is plotted in Figure 5.16, with the three feed rates broken into separate charts. Within each chart, average cutting power is plotted against the jet pressure, with various jet orientations denoted by different colors. A line at 3.5 kW represents the point at which burn spikes and wheel breakdown begin to occur.

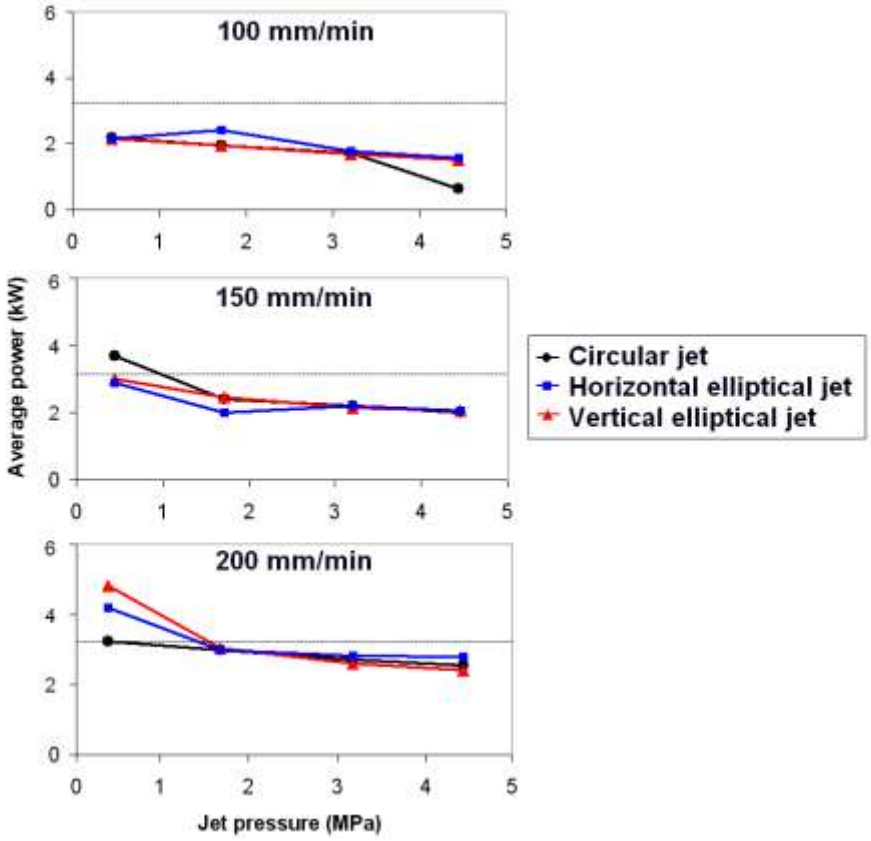

Figure 5.16: Summary of average cutting power values with 1.5 kW burn limit, includes trials where wheel breakdown occurred.

Removing the outliers caused by wheel breakdown yields the average power usage data plotted in Figure 5.17.

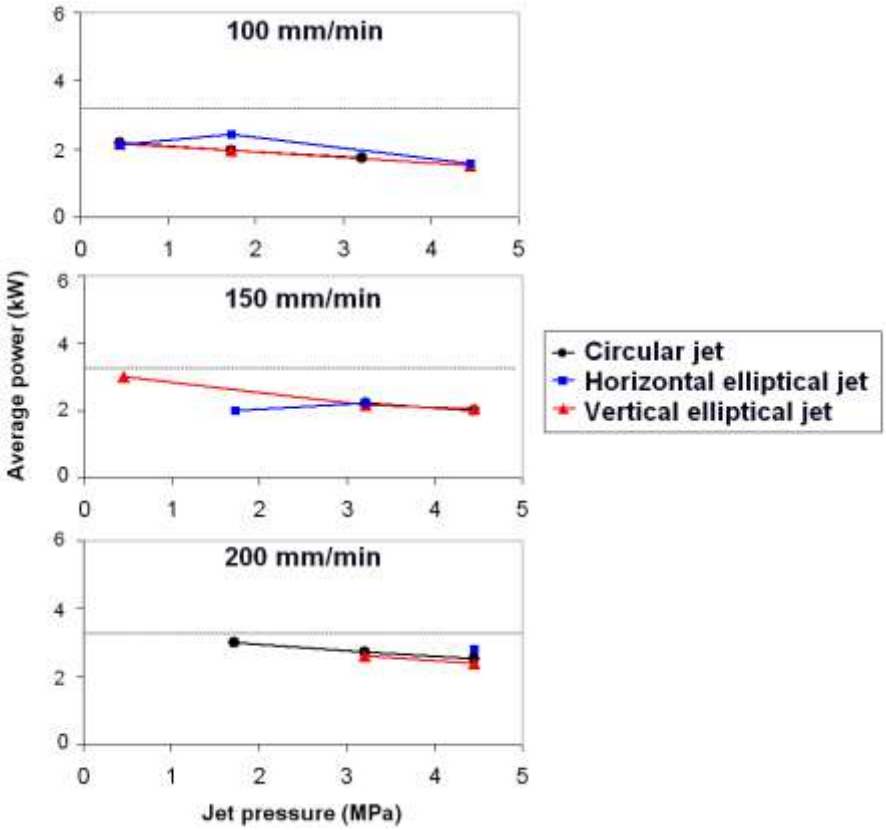

Figure 5.17: Summary of average cutting power with 1.5 kW burn limit, trials where wheel breakdown occurred removed.

As the feed rate is increased, so too is the average cutting power; roughly a 150% increase in average power accompanies doubling the feed rate. Towards the burn limit of 3.5 kW, behavior of the power becomes chaotic and unpredictable, as seen by the departure of several data points from the norm at the lowest jet pressure in the 150 and 200 mm/min plots. For the profile, depth of cut, and nozzle aperture area used in this research, optimized grinding parameters with an eye towards minimum required cutting fluid and maximum productivity would involve a jet pressure in excess of 2 MPa and a feed rate of at most 200 mm/min. Extrapolating further, increasing the feed rate beyond 200 mm/min could be possible given the steady negative trend of all average cutting powers, but the small slope suggests not much improvement is to be had. Additionally, the fact that 6 of the 12 experiments performed at 200 mm/min resulted in wheel breakdown suggests that higher feeds will not be able to produce satisfactory surface finishes with a single pass.

5.3 Grinding Forces

Cutting fluid is used in machining to perform three main tasks: to remove waste material from the cutting zone, to provide cooling, and to lubricate the region of tool-workpiece interaction. In addition to surface finish and power analysis, grinding force measurements were also gathered to gain further insight into the process. The total grinding force can be summarized by the formula:

$$F_{total} = F_{rub} + F_{plow} + F_{cut} \tag{5.4}$$

Where F_{rub}, F_{plow}, and F_{cut} are the three partitions of the total force F_{total} due to rubbing, plowing, and cutting, respectively. As the grinding wheel moves forward into the workpiece, material is removed in long, tapered chips, as illustrated by the shaded region in Figure 5.18. During the first part of chip formation, a large portion of the energy and grinding force is devoted to rubbing. As the depth increases, plowing surpasses rubbing. Finally, cutting begins to overtake both rubbing and plowing to become the dominant process. These stages are illustrated schematically in Figure 5.18 and are collectively known as the phenomenon of "size effect".

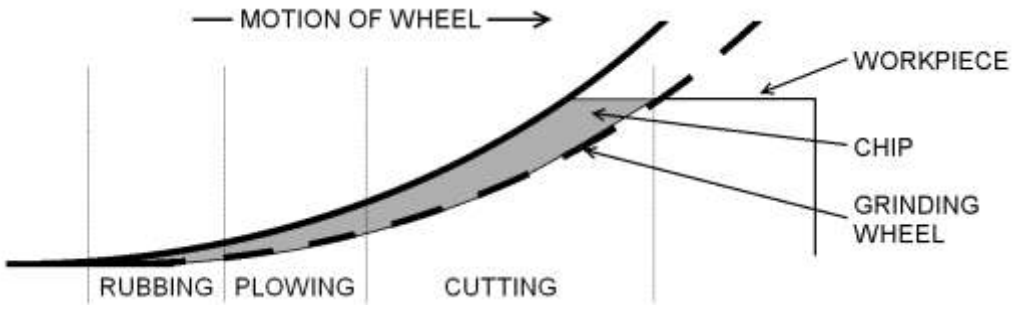

Figure 5.18: Cutting, plowing, and rubbing regions of chip formation.

As discussed briefly in Section 1.2.2 dealing with the cutting mechanics, the total grinding force can be broken into three measurable axial components: a normal force F_N represented orthogonally out of the surface of the workpiece, a tangential force F_T represented in the plane of workpiece in line with the feed, and a transverse force aligned with the direction of the grinding wheel spindle. These forces are summarized

schematically in Figure 1.7. The normal and tangential forces can be useful in deducing the relative proportions of rubbing, plowing, and cutting. Due to their defined orientations, the normal force can be associated with the surface finish of the workpiece and the tangential force with power consumption [Li *et al.* 2002]. In fact, grinding power is related proportionally to tangential force and wheel velocity by the equation:

$$Grinding\ power = F_T \times v \qquad (5.5)$$

Where v is the wheel surface velocity. Using the same section of workpiece as in the power data—that is, only during full wheel engagement—the average normal force and tangential values were calculated for each experiment where excessive wheel breakdown did not occur. Plotted against jet pressure for each of the tested feed rates and jet orientations, this data is provided in Figure 5.19 and Figure 5.20, respectively.

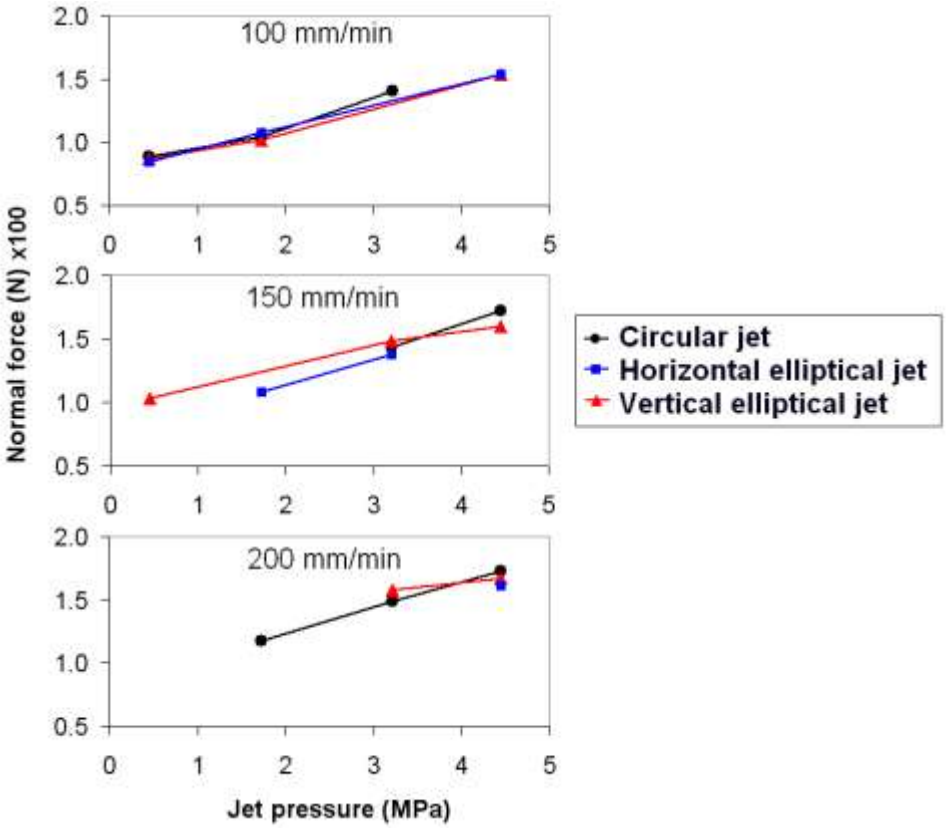

Figure 5.19: Summary of average normal force values in trials without wheel breakdown.

The apparent trend of increasing normal force with jet pressure can perhaps be partially attributed to the increasing fluid flow into the grinding zone. There is an approximate 70% increase in normal force from 0.45 to 4.45 MPa for all feed rates. As more fluid is forced through the same volume between the wheel and workpiece—all other parameters held constant—hydrodynamic pressure is likely increased. The secondary trend of an overall increase in normal force with feed rate is expected: higher feed means more work is being completed, and more work means more force is necessary.

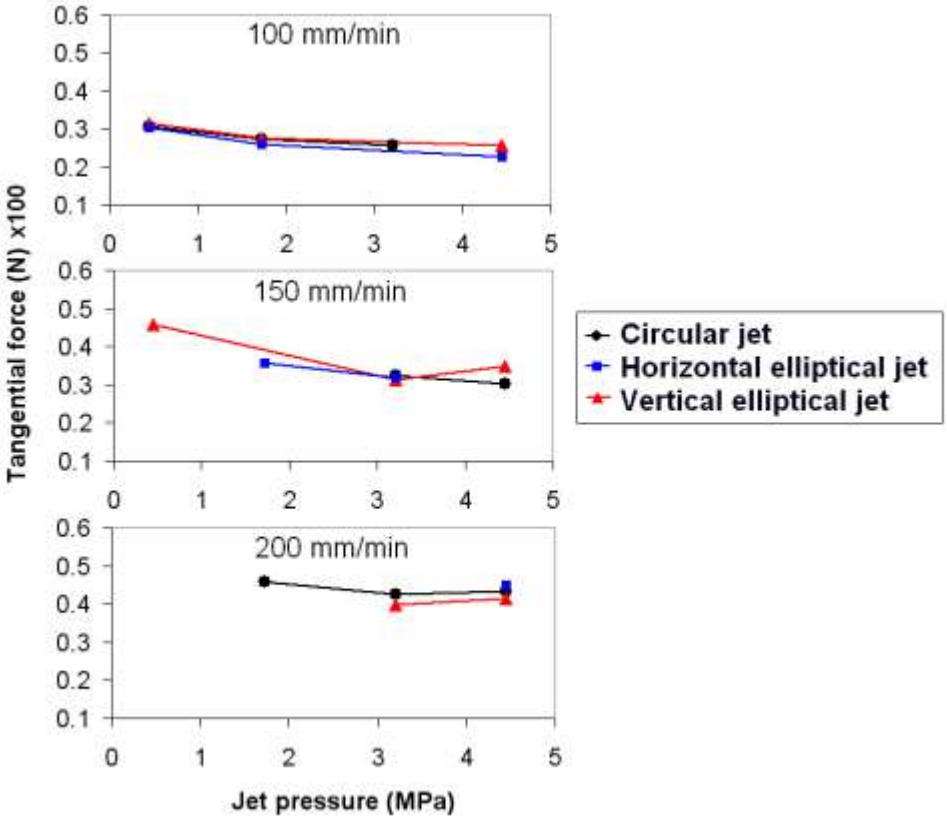

Figure 5.20: Summary of average tangential force values in trials without wheel breakdown.

Increasing jet pressure causes a 29% drop in tangential forces, corroborated by the power data to which the tangential force is directly associated; as defined by equation 5.5 and observed in the average power curves plotted in Figure 5.17. As with the normal force, increasing the feed rate causes an increase in tangential forces; the values at 100 mm/min are approximately 60% those at 200 mm/min. Again, this increase in force with feed is due to the increase in amount of work being done, and thereby the force required.

A combination of the normal and tangential forces yields a quantitative measure that can be used to imply characteristics of the cutting behavior. Because the force ratio μ is defined as F_T/F_N, a larger ratio indicates a more efficient cut with a larger proportion of the forces being directed to cutting as opposed to rubbing and plowing. As with the total grinding force, there are three components of the force ratio:

$$\mu_{total} = \mu_{rub} + \mu_{plow} + \mu_{cut} \tag{5.6}$$

Where the three components are due to rubbing, plowing, and cutting, respectively. This force ratio is plotted in Figure 5.21 for a sample workpiece representative of the force trends observed, superimposed over the observed normal and tangential forces. A feed rate of 150 mm/min and jet pressure of 3.21 MPa were used with the vertical elliptical jet for this trial.

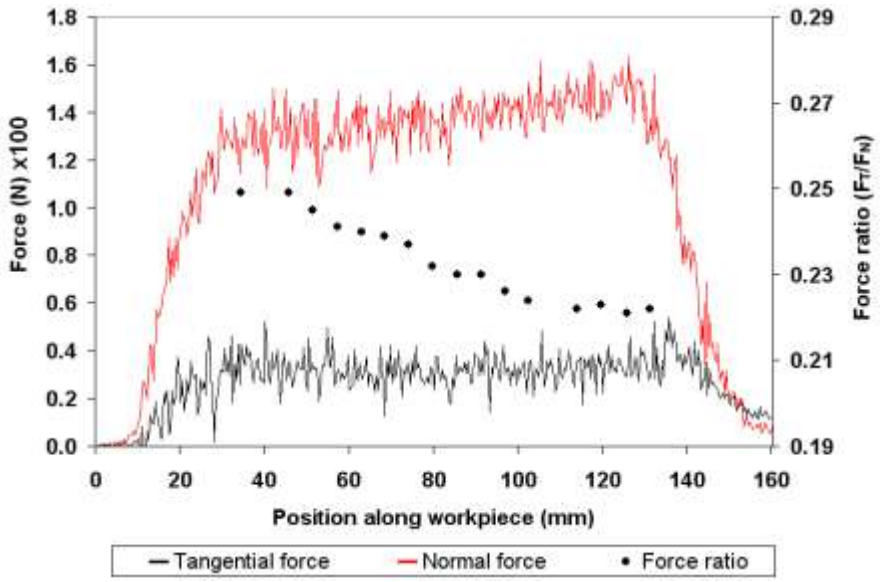

Figure 5.21: Tangential and normal forces overlaid with the force ratio for a sample workpiece; 150 mm/min feed at 3.21 MPa jet pressure.

An 11.8% drop in the force ratio during this grind was brought about by the increasing normal force over the length of the workpiece. Unacceptable wheel breakdown did not occur during this experimental trial: an average form error of 4 μm and R_a of 3.8 μm were

among the average results obtained. The increase in normal force over the length of the grind can be attributed to an increase in the proportion of abrasive grits engaging in rubbing as opposed to cutting—attritious wheel wear—as discussed in Section 1.2.2 and illustrated in Figure 5.22. The same chip is being formed as a result of an unchanged rake face on the abrasive grain, but a "wear-flat" causes an additional rubbing force, thus increasing the friction. The rubbing component of the force ratio can be seen as proportional to the area of wear-flats on the grinding wheel surface, while the plowing component is roughly constant throughout the grinding process [Malkin 1989].

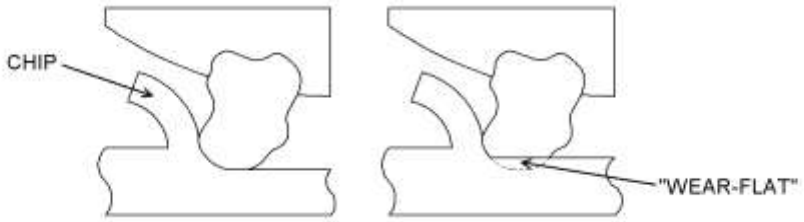

Figure 5.22: Attritious wearing of an abrasive grain.

This attritious wear results in a lower quality surface finish as the grind progresses, as evidenced by an R_a value of 2.8 μm at the start of full wheel engagement, followed by 3.3 μm near the midpoint, and 3.9 μm at the end. There was no significant rise in power during this grind, as seen in the steady tangential force.

The average force ratio for each experiment is summarized Figure 5.23 for the three tested feed rates plotted against the jet pressure used; within each figure the various jet orientations are separated by line color as indicated. Figure 5.23 includes only those trials where wheel breakdown did not occur.

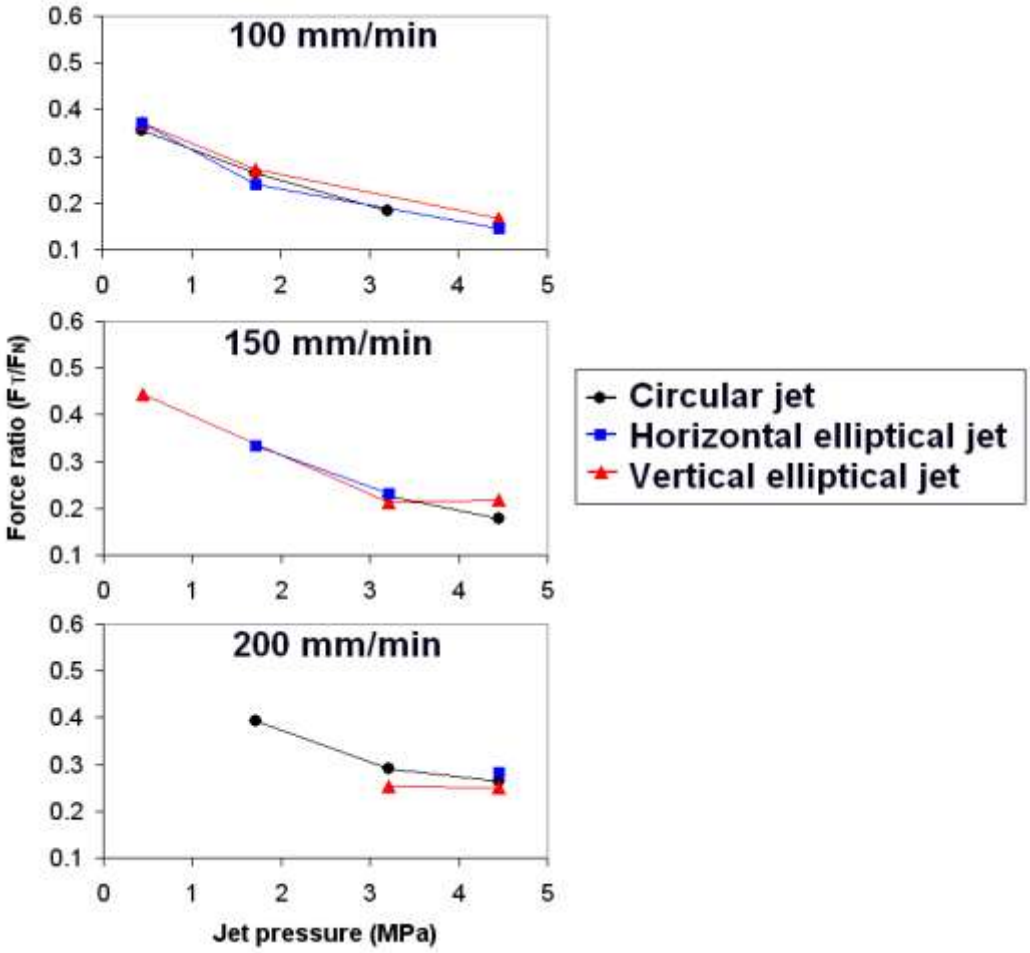

Figure 5.23: Summary of averaged force ratio, trials with wheel breakdown removed.

Several trends previously observed in force and surface finish analysis are visible within this data. For example, the average force ratio decreases with jet pressure, likely due in part to improved lubricity at the cutting zone. Also, the proximity of circular, horizontal elliptical, and vertical elliptical data points at each jet pressure indicates very little influence can be exerted over the grinding forces by manipulating the shape of the cutting fluid jet aperture. However, as shown previously, only the vertical elliptical jet was able to provide satisfactory lubrication at the lowest jet pressure for a feed rate of 150 mm/min. The circular jet was successful at a pressure of 1.72 MPa at the 200 mm/min feed, so the vertical elliptical jet and circular jet can be considered similar in performance quality, while the horizontal elliptical jet is inferior. Finally, increasing the feed rate raises the force ratio: ratio values at 100 mm/min are between 53 and 69% those at 200

mm/min. The size effect as discussed in Figure 5.18 is largely responsible for this tendency. As the feed increases, the depth each wheel grain is plunged forward into the workpiece increases. This causes the cutting component to increase respect to rubbing and plowing, thus yielding a more effective cut.

5.4 Summary

The following is a summary of trends and conclusions drawn from the research discussed in this chapter.

As the pressure of the coolant jet is raised, the performance of elliptical and circular jets—in terms of resultant surface roughness, power consumption, and grinding forces—increase in similarity. This trend is due to the fact that as pressure is increased all jets, regardless of initial shape, converge into a circular shape. A maximum difference of 10% total power consumed existed between elliptical and circular jets for all experimental trials except those at the highest feed rate with lowest jet pressure. This similarity in performance at high pressure is likely due to the fact that at low pressure, surface tension and cohesion of the coolant is sufficient to maintain the non-circular profile of the jet over a longer distance. At higher jet pressures, the surface roughness of the finished workpiece is improved. There are several causes of this trend. First, as observed by Hartlen *et al.* [2008], high pressure jets cleaned debris from the pores of the grinding wheel, leading to more efficient cutting. Second, when the jet velocity is much slower than the wheel, as is the case here with the jet pressure of 0.45 MPa—41.7% the speed of the wheel—power at the spindle is wasted accelerating the jet to the same velocity as the wheel, leading to higher power consumption and lower grinding overall efficiency. Finally, an increase in jet pressure lowers the force ratio, thus indicating an improvement in lubricity as a direct result of more effective cutting fluid application. In summary, raising the jet pressure decreases consumed power, raises the allowable feed rate, improves lubrication at the grinding zone, and improves the resultant workpiece surface finish.

Raising the feed rate has the largest influence on the grinding process and the resultant workpiece finish. The sensitivity of grinding to feed rate is inherent to the process of machining; material is being removed at the specified feed rate. Novel application of elliptical and circular jets has given a new dimension to this sensitivity. In the domain of lower pressure jets, the shape of the nozzle is critical, as seen in the results of surface finish analysis. If catered properly to the grinding profile cross-section and desired grinding parameters, an appropriately shaped aperture producing a low pressure jet can out-perform a circular nozzle in terms of surface quality.

A complete summary of the experimental work conducted can be found in Table 6 and Table 7 of the Appendix, broken down into surface finish and power-related, variables, respectively. Trials where excessive wheel breakdown occurred are noted in red.

CHAPTER 6 CONCLUSION

6.1 Research Summary

Historically, there has been little research attempted in the realm of complex internal nozzle contouring, likely due to the necessary advanced machining being cost prohibitive. In this research, several novel design parameters for low-divergence elliptical nozzles were investigated through the use of rapid-prototyped models and digital image analysis. Exit angle, arc length range, and aperture aspect ratio were the chosen geometric design parameters selected for study. The detailed internal contouring of each nozzle was generated by blending six unique fourth-order Bezier curves with user-specified characteristics. AutoCAD was used to create a three-dimensional model exported to a rapid-prototype fused deposition modeler. Feasibility testing proved that the ABS plastic could withstand pressures occasionally in excess of 4 MPa for the entire test period of approximately 10 machining hours.

Results of digital imaging experiments at various flow rates show that minor axis jet divergence can be reduced by increasing the minor axis exit angle while holding fixed the major axis exit angle. Minor axis jet divergence can similarly be decreased by increasing the major axis exit angle or arc length range. Furthermore, major axis jet divergence is seemingly not affected by exit angles or arc length range. As the aspect ratio of the aperture is enlarged, jet divergence in all directions increases.

Of the elliptical aperture nozzles tested in this research, the best elliptical nozzle—in terms of divergence angle and flow homogeneity—had a major axis exit angle of 40° and a minor axis exit angle of 80°, an arc length range of 0.00 mm, an area equivalent to a circle 6 mm in diameter, and an aperture aspect ratio of 1.56. At a flow rate of 33.3 LPM, the jet showed 0.9° of divergence in the minor axis of the ellipse and 0.4° in the major axis. Previous attempts to generate non-circular nozzles have resulted in divergent fans of greater than 10° in one axis [Murphy *et al.* 2007].

Application of this nozzle design to profiled creep-feed grinding led to the development of a similar nozzle with identical contours but an aperture area equivalent to a circle 3.5 mm in diameter. This nozzle was compared—through extensive grinding experiments—to a nozzle with a circular aperture 3.5 mm in diameter and a standard "coherent jet nozzle" design.

Investigation of grinding parameters including feed rate, jet pressure, nozzle aperture, and nozzle aperture orientation led to a collection of surface finish, power consumption, and grinding force data from which trends involving the proper setup for coolant application could be drawn. As the pressure of the coolant jet is raised, the performance of elliptical and circular jets—in terms of resultant surface roughness, power consumption, and grinding forces—increase in similarity. A maximum difference of 10% total power consumed existed between elliptical and circular jets for all experimental trials except those at a feed rate of 150 and 200 mm/min with a jet pressure of 0.45 MPa. Lower pressure allows a jet to maintain its shape over a longer distance, and therefore the higher quality surface finishes achieved by the horizontally oriented ellipse at low pressures implied a better coolant distribution. Finally, raising the jet pressure decreases power during cutting as a direct result of improved lubrication, thereby raising the allowable maximum feed rate and still being able to obtain a satisfactory surface finish.

A feed rate of 200 mm/min—the highest tested, was able to produce satisfactory surface roughness values between 3.09 and 3.48 μm depending on the aperture shape and orientation being used to project the cutting fluid, with the circular aperture performing best, followed by the horizontally oriented ellipse, and then the vertically oriented ellipse. The slowest feed rate, 100 mm/min, produced workpiece roughness values between 3.12 and 4.31 μm, with the horizontal elliptical aperture performing best, followed by the vertical ellipse and the circle.

6.2 Conclusions and Future Research

The trends in jet behavior observed during this research enable future development of elliptical jets with predictable angles of divergence in both the major and minor axes. If

unique or complex geometries are thereby desired, the novel fabrication method has also proven to be a feasible and cost-effective alternative to the traditional machining method. If non-circular apertures that yield low divergent jets are desired, the process of developing the internal contouring developed through this research will allow coherency rivaling that of a circular jet.

Additionally, an extensive study of creep-feed grinding parameters has shown conclusively that surface finish and power consumption are insensitive to nozzle shape, allowing for a greater freedom in nozzle selection provided that coherency is maintained. For profiles without extreme depth changes, a circular jet may prove to be simplest, most productive option to deliver cutting fluid. Initial hypotheses that elliptical jets would perform differently than the circular jet across a variety of comparable grinding and fluid parameters have proven less significant than expected; instead, more traditional grinding variables such as feed rate and jet pressure hold more influence over the resultant surface finish of a workpiece.

Further study in the area of profiled jets may prove valuable in the realm of surface grinding where small depths of cut require lower pressure cutting fluid jets—a domain where jet shape can be maintained and variously shaped apertures have the potential to perform differently.

APPENDIX

Figure A1: Summary of normal forces for all experiments at a feed rate of 100 mm/min.

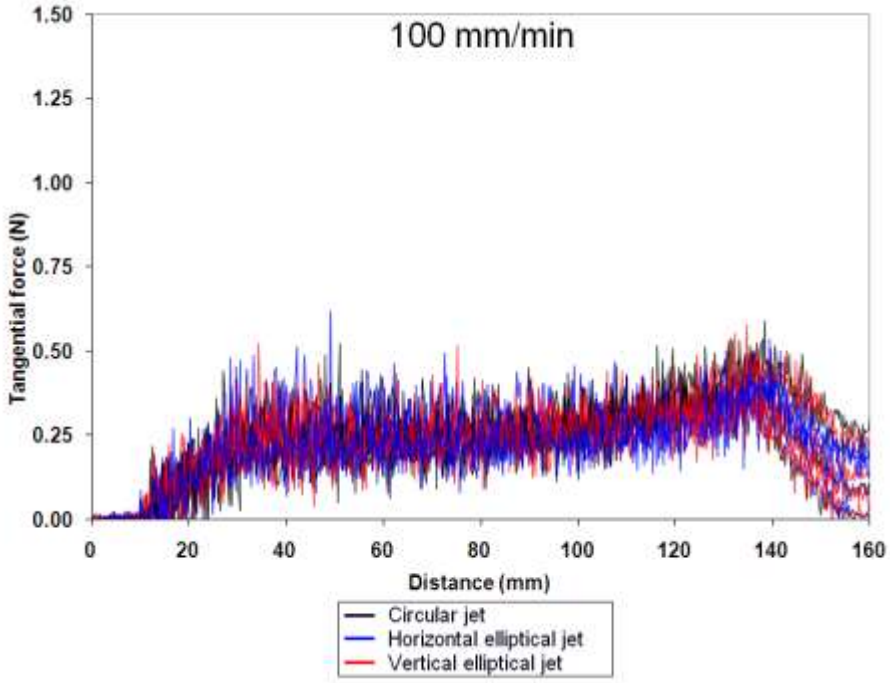

Figure A2: Summary of tangential forces for all experiments at a feed rate of 100 mm/min.

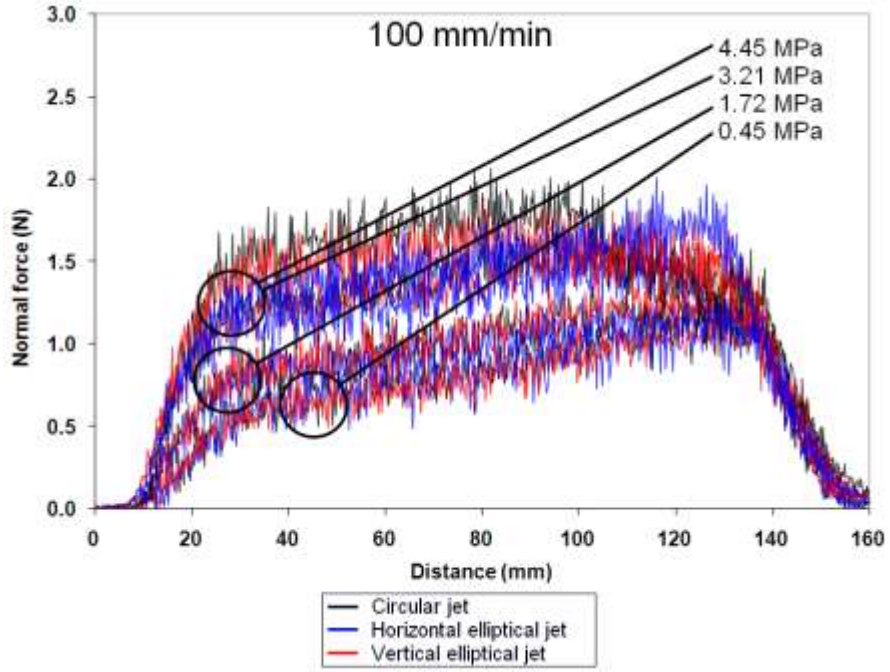

Figure A3: Summary of normal forces for all experiments at a feed rate of 150 mm/min.

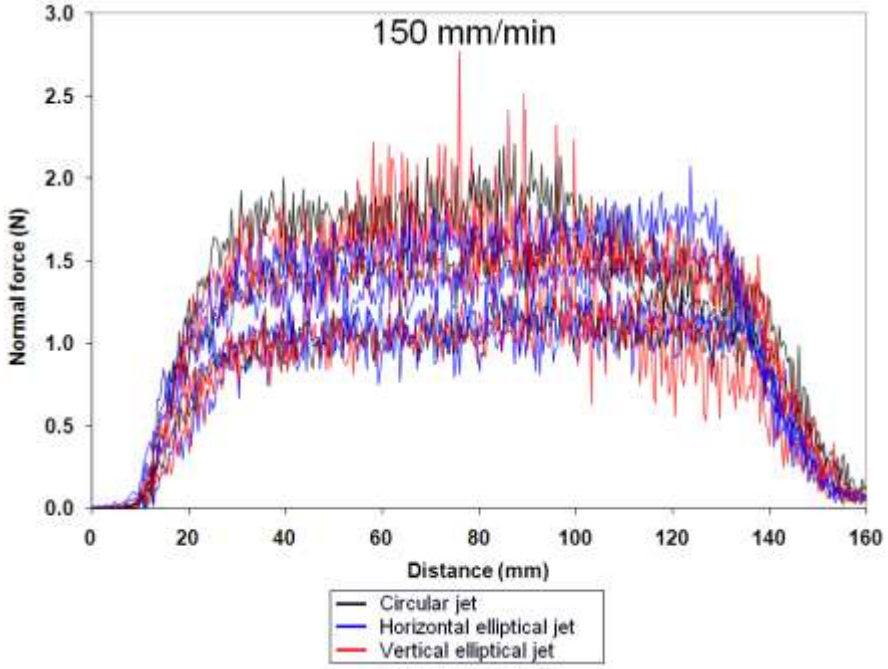

Figure A4: Summary of tangential forces for all experiments at a feed rate of 150 mm/min.

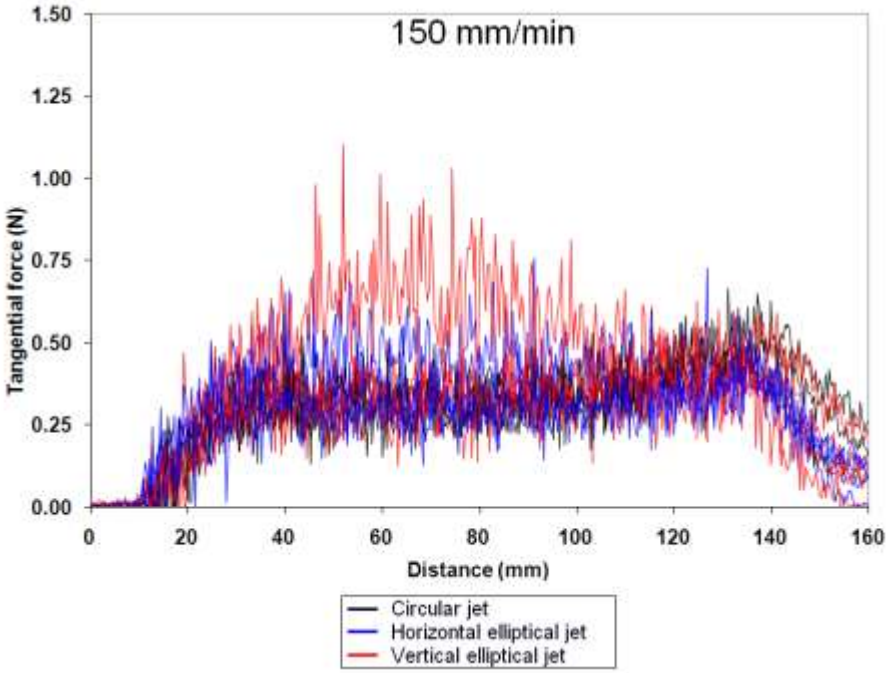

Figure A5: Summary of normal forces for all experiments at a feed rate of 200 mm/min.

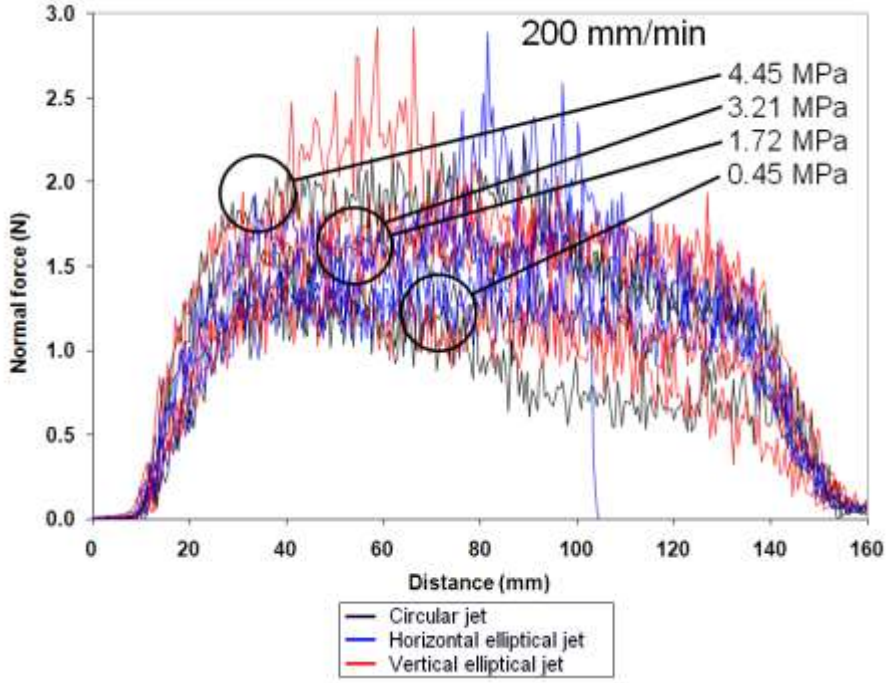

Figure A6: Summary of tangential forces for all experiments at a feed rate of 200 mm/min.

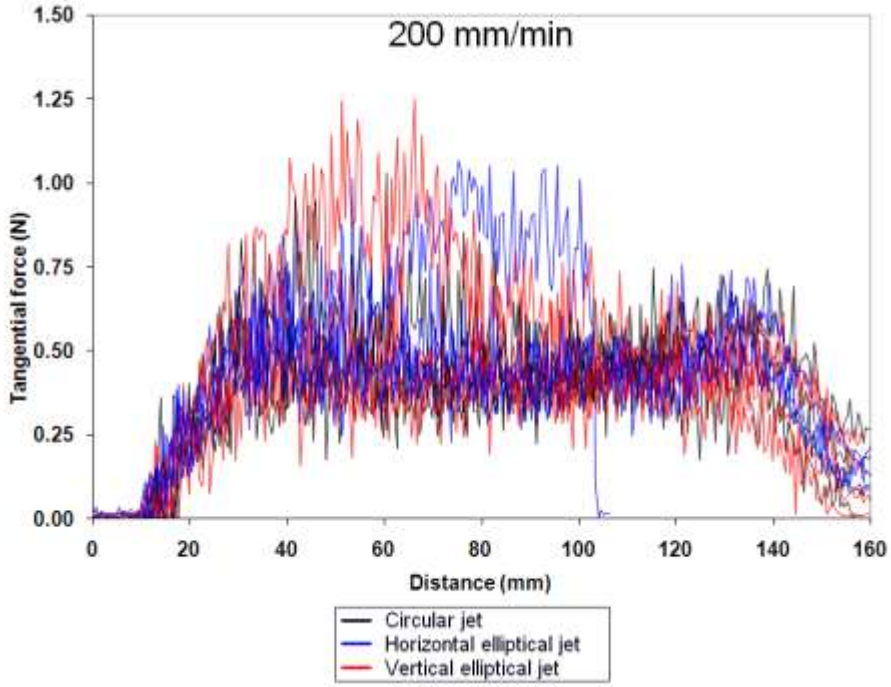

Table 6 – Surface Finish Summary Table

#	Feed rate (mm/min)	Jet pressure (MPa)	Ra (µm) @ 30 mm	Ra (µm) @ 80 mm	Ra (µm) @ 115 mm	Ra (µm) Average	Ra (µm) σ	Quality	Location of break down	Form error (mm) @ 30 mm	Form error (mm) @ 80 mm	Form error (mm) @ 115 mm	Form error (mm) Average	Form error (mm) σ
CIRCULAR JET														
1	100	0.45	3.15	3.37	3.22	0.36	0.11	Average	N/A	0.004	0.004	0.004	0.004	0.000
2	150	0.45	3.17	3.99	3.97	0.45	0.47	Average	Slopes	0.004	0.005	0.005	0.004	0.001
3	200	0.45	3.10	4.62	HIGH	0.55	1.08	Poor	Extremities	0.004	0.005	HIGH	0.004	0.001
4	100	1.72	2.83	3.63	3.35	0.27	0.40	Average	N/A	0.003	0.004	0.004	0.004	0.000
5	150	1.72	2.95	3.22	HIGH	0.34	0.19	Poor	Corners	0.004	0.004	HIGH	0.004	0.000
6	200	1.72	3.11	3.53	2.92	0.40	0.31	Average	N/A	0.003	0.004	0.004	0.004	0.000
7	100	3.21	3.38	3.18	3.42	0.19	0.13	Average	N/A	0.004	0.004	0.004	0.004	0.000
8	150	3.21	3.18	4.55	3.07	0.24	0.82	Average	Corners	0.004	0.005	0.004	0.004	0.000
9	200	3.21	2.81	3.14	3.77	0.30	0.48	Average	N/A	0.004	0.004	0.004	0.004	0.000
10	100	4.45	6.08	3.67	3.19	0.17	1.55	Average	Corners	0.005	0.004	0.004	0.004	0.001
11	150	4.45	2.86	3.30	2.97	0.19	0.23	Average	N/A	0.004	0.004	0.004	0.004	0.000
12	200	4.45	3.22	3.06	2.98	0.28	0.12	Average	N/A	0.004	0.004	0.004	0.004	0.000
HORIZONTAL ELLIPTICAL JET														
1	100	0.45	3.49	3.26	3.14	0.37	0.18	Average	N/A	0.004	0.004	0.004	0.004	0.000
2	150	0.45	2.88	3.18	2.96	0.45	0.16	Average	N/A	0.004	0.004	0.004	0.004	0.000
3	200	0.45	3.29	6.44	BURN	0.48	2.23	Average	Extremities	0.004	0.007	HIGH	0.005	0.002
4	100	1.72	2.78	3.30	3.19	0.28	0.28	Average	N/A	0.004	0.004	0.004	0.004	0.000
5	150	1.72	3.03	3.51	HIGH	0.33	0.34	Poor	Corners	0.004	0.004	HIGH	0.004	0.000
6	200	1.72	3.37	HIGH	4.79	0.41	1.01	Poor	Extremities	HIGH	0.011	0.005	0.008	0.004
7	100	3.21	2.82	7.15	2.97	0.18	2.46	Average	Corners	0.004	0.007	0.004	0.005	0.002
8	150	3.21	2.84	3.30	3.91	0.22	0.53	Average	N/A	0.004	0.004	0.004	0.004	0.000
9	200	3.21	2.64	3.49	3.14	0.26	0.43	Average	N/A	0.004	0.004	0.004	0.004	0.000
10	100	4.45	2.94	3.00	3.40	0.18	0.25	Average	N/A	0.004	0.004	0.004	0.004	0.000
11	150	4.45	3.23	3.25	3.77	0.23	0.31	Average	N/A	0.004	0.004	0.004	0.004	0.000
12	200	4.45	2.73	3.35	3.23	0.26	0.33	Average	N/A	0.003	0.004	0.004	0.004	0.000
VERTICAL ELLIPTICAL JET														
1	100	0.45	2.96	3.13	2.65	0.37	0.24	Average	N/A	0.004	0.004	0.004	0.004	0.000
2	150	0.45	3.37	8.83	BURN	0.43	3.86	Poor	Extremities	0.004	HIGH	HIGH	0.004	0.004
3	200	0.45	6.72	HIGH	BURN	0.47	0.00	Poor	Corners	HIGH	HIGH	HIGH	0.068	0.000
4	100	1.72	3.26	3.08	3.82	0.24	0.39	Average	N/A	0.004	0.004	0.005	0.004	0.000
5	150	1.72	3.21	3.52	2.83	0.33	0.35	Average	N/A	0.004	0.004	0.004	0.004	0.000
6	200	1.72	2.85	HIGH	HIGH	0.41	0.00	Poor	Corners	HIGH	HIGH	0.041	0.041	0.000
7	100	3.21	3.56	9.62	3.82	0.19	3.43	Average	Corners	0.004	0.010	0.005	0.006	0.003
8	150	3.21	4.31	3.65	3.46	0.23	0.44	Average	Extremities	0.004	0.004	0.004	0.004	0.000
9	200	3.21	2.65	2.76	6.11	0.33	1.96	Average	Extremities	0.003	0.004	0.006	0.004	0.002
10	100	4.45	3.80	3.77	3.11	0.15	0.39	Average	Extremities	0.005	0.005	0.004	0.004	0.000
11	150	4.45	2.78	2.76	9.02	0.19	3.61	Average	Corners	0.003	0.004	0.009	0.005	0.003
12	200	4.45	3.00	4.07	3.37	0.29	0.55	Average	N/A	0.003	0.004	0.004	0.003	0.000

Table 7 – Power Summary Table

#	Feed rate (mm/min)	Jet pressure (MPa)	Total Power (kW)	Average Power (kW)	MRR (m^3/s)	Cutting efficiency ($kW\text{-}s/m^3$)	Force Ratio (F_T/F_N)	Avg F_T (N)	Avg F_N (N)
CIRCULAR JET									
1	100	0.45	37950	2.01	33.89	1120	0.36	30.5	88.6
2	150	0.45	33350	3.40	50.84	656	0.44	43.9	99.4
3	200	0.45	28400	3.00	67.79	419	0.55	50.8	94.3
4	100	1.72	35000	1.81	33.89	1033	0.26	27.3	104.1
5	150	1.72	28950	2.22	50.84	569	0.33	35.2	107.0
6	200	1.72	26650	2.77	67.79	393	0.39	45.7	117.2
7	100	3.21	31350	1.60	33.89	925	0.18	25.6	140.5
8	150	3.21	26600	2.04	50.84	523	0.23	32.3	143.5
9	200	3.21	24250	2.52	67.79	358	0.29	42.6	149.0
10	100	4.45	27650	0.58	33.89	816	0.16	25.2	163.3
11	150	4.45	24800	1.85	50.84	488	0.22	30.3	172.1
12	200	4.45	22750	2.35	67.79	336	0.26	43.2	172.6
HORIZONTAL ELLIPTICAL JET									
1	100	0.45	38200	2.00	33.89	1127	0.37	31.5	87.0
2	150	0.45	34550	2.77	50.84	680	0.45	45.9	103.5
3	200	0.45	26950	4.45	67.79	398	0.36	71.8	159.3
4	100	1.72	35000	1.81	33.89	1033	0.27	27.5	101.8
5	150	1.72	29200	2.28	50.84	574	0.32	36.3	112.0
6	200	1.72	26950	2.82	67.79	398	0.40	47.9	120.8
7	100	3.21	30200	1.57	33.89	891	0.17	24.0	140.8
8	150	3.21	25500	1.99	50.84	502	0.21	31.4	148.1
9	200	3.21	23350	2.41	67.79	344	0.25	39.8	158.0
10	100	4.45	27250	1.41	33.89	804	0.17	25.8	153.5
11	150	4.45	24200	1.90	50.84	476	0.22	34.8	159.6
12	200	4.45	21550	2.22	67.79	318	0.25	41.5	167.1
VERTICAL ELLIPTICAL JET									
1	100	0.45	37600	1.98	33.89	1109	0.37	30.5	84.5
2	150	0.45	40600	2.67	50.84	799	0.42	66.5	152.2
3	200	0.45	34950	3.89	67.79	516	0.46	65.6	150.4
4	100	1.72	35600	2.25	50.84	700	0.24	25.8	108.0
5	150	1.72	28450	1.84	33.89	839	0.33	35.7	107.8
6	200	1.72	26550	2.77	67.79	392	0.40	45.1	112.2
7	100	3.21	32250	1.64	33.89	952	0.19	24.6	131.9
8	150	3.21	26150	2.04	50.84	514	0.23	31.8	137.3
9	200	3.21	25050	2.60	67.79	370	0.32	43.2	136.9
10	100	4.45	28350	1.46	33.89	837	0.15	22.5	153.8
11	150	4.45	23150	1.90	50.84	455	0.18	29.5	161.7
12	200	4.45	25050	2.59	67.79	370	0.28	44.9	161.0

REFERENCES

1. Alberdi, R., Sanchez, J., Pombo, I., Ortega, N., Izquierdo, B., Plaza, S., Barrenetxea, D., "Strategies for optimal use of fluids in grinding." *International Journal of Machine Tools & Manufacture* Vol. 51 (2011): 491-499.
2. Amini, G., Dolatabadi, A., "Axis-switching and breakup of low-speed elliptic liquid jets." *International Journal of Multiphase Flow* Vol. 42 (2012): 96-103.
3. Axinte, D., Chiffre, L.De, "Effectiveness and resolution of tests for evaluating the performance of cutting fluids in machining aerospace alloys." *CIRP Annals – Manufacturing Technology* Vol. 57 (2008): 129-132.
4. Azad, M., Quinn, W., Groulx, D., "Mixing in turbulent free jets issuing from isosceles triangular orifices with different apex angles." *Experimental Thermal and Fluid Science* Vol. 39 (2012): 237-251.
5. Banerjee, S., Ghosal, S., Dutta, T., "Development of a simple technique for improving the efficacy of fluid flow through the grinding zone." *Journal of Materials Processing Technology* Vol. 197 (2007): 306-313.
6. Brinksmeier, E., Heinzel, M., Wittmann, M., "Friction, cooling and lubrication in grinding." *CIRP Annals* Vol. 48 No. 2 (1999): 581-598.
7. Cai, R., Morgan, M., "Design of a user guidance manual for optimal coolant delivery in grinding." *International Journal of Advanced Manufacturing Technology* Vol. 38 (2008): 410-417.
8. Cameron, A., *An investigation into the effects of wheel-cleaning parameters on the creep-feed grinding process*. M.A.S.c. Dissertation, Dalhousie University, 2010.
9. Chang, C., "An application of lubrication theory to predict useful flow rate of coolants on grinding porous media." *Tribology International* Vol. 30, No. 8 (1997): 575-581.
10. Cui, C., Webster, J., "Experimental investigation of coolant jet design for creep feed grinding of gas turbine airfoils." *IGTI Journal of Turbomachinery* Vol. 9 (1994): 91-96.

11. Engineer, F., Guo, C., Malkin, S., "Experimental Measurement of Fluid Flow Through the Grinding Zone." *Journal of Engineering for Industry* Vol. 114 (1992): 61-66.
12. Ezugwu, E., "Key improvements in the machining of difficult-to-cut aerospace superalloys." *International Journal of Machine Tools & Manufacture* Vol. 45 (2005): 1353-1367.
13. Ghassemieh, E., Versteeg, H., Acar, M., "The effect of nozzle geometry on the flow characteristics of small water jets." *Journal of Mechanical Engineering Science* Vol. 220 (2006): 1739-1753.
14. Greaves, I., "Respiratory health of automobile workers exposed to metal working fluid aerosols." *American Journal of Industrial Medicine* Vol. 32 (1997): 450-459.
15. Gviniashvili, V., Webster, J., Rowe, W., "Fluid flow and pressure in the grinding wheel-workpiece interface." *Transactions of the ASME* Vol. 127 (2005): 198-205.
16. Gviniashvili, V., Woolley, N., Rowe, W., "Useful coolant flow rate in grinding." *International Journal of Machine Tools & Manufacture* Vol. 44 (2003): 629-636.
17. Hartlen, D., Bauer, R., Warkentin, A., "Comparison of conventional, coherent-jet, and high-pressure coolant delivery systems for profile grinding." *Transactions of the Canadian Society of Mechanical Engineers* Vol. 32, No. 1 (2008): 107-119.
18. Ho, C.-M., Gutmark, E., "Vortex induction and mass entrainment in a small-aspect-ratio elliptic jet." *Journal of Fluid Mechanics* Vol. 179 (1987): 383-405.
19. Hoyt, J., Taylor, J., "Effect of nozzle boundary layer on water jets discharging in air." *ASME Fluids Engineering Division* Vol. 31 (1985): 93-100.
20. Husain, H., Hussain, F., "Elliptic jets, Part 2: Dynamics of coherent structures: Pairing." *University of Houston Technical Report* (1992): 1-58.
21. Irani, R., Bauer, R., Warkentin, A., "A review of cutting fluid application in the grinding process." *International Journal of Machine Tools & Manufacture* Vol. 45 (2005): 1696-1705.
22. Irani, R., *Dual cutting fluid application in the grinding process*. M.A.S.c. Dissertation, Dalhousie University, 2006.

23. Iyogun, C., Birouk, M., "Effect of sudden expansion on entrainment and spreading rates of a jet issuing from asymmetric nozzles." *Journal of Flow, Turbulence, and Combustion* Vol. 82 (2009): 287-315.
24. Jeng, T., Tzeng, S., Liao, H., "Flow visualizations and heat transfer measurements for a rotating pin-fin heat sink with a circular impinging jet." *International Journal of Heat and Mass Transfer* Vol. 52 (2009): 2119-2131.
25. Jin, T., Stephenson, D., Rowe, W., "Estimation of the convection heat transfer coefficient of coolant within the grinding zone." *Journal of Engineering Manufacture* Vol. 217 (2003): 397-407.
26. Klocke, F., Baus, A., Beck. T., "Coolant induced forces in CBN high speed grinding with shoe nozzles." *Annals of the International Institution for Production Engineering Research* Vol. 49, No. 1 (2000): 241-244.
27. Li, Z., Lin, B., Xu, Y., Hu, J., "Experimental studies on grinding forces and force ratio of the unsteady-state grinding technique." *Journal of Materials Processing Technology* Vol. 129 (2002): 76-80.
28. Li, Z., *Improvement of waterjet and abrasive waterjet nozzle*. PhD Dissertation, New Jersey Institute of Technology, 1994.
29. Malkin, S., "Grinding technology: Theory and applications of machining with abrasives." Society of Manufacturing Engineers, Dearborn, Michigan (1989): 143-163.
30. McCarthy, M., Molloy, N., "Review of stability of liquid jets and the influence of nozzle design." *The Chemical Engineering Journal* Vol 7 (1974): 1-20.
31. Morgan, M., Baines-Jones, V., "On the coherent length of fluid nozzles in grinding." *Key Engineering Materials* Vol. 404 (2009): 61-67.
32. Murphy, B., Pottle, D., Rockwell, A., Ryan, K., *Coolant delivery system for creep-feed grinding*. MECH 4010 Design Project Report, Dalhousie University, 2007.
33. Nandy, A., Paul, S., "Effect of coolant pressure, nozzle diameter, impingement angle and spot distance in high pressure cooling with neat oil in turning Ti-6Al-4V." *Machining Science and Technology* Vol. 12 (2008): 445-473.

34. Nguyen, T., Zhang, L., "An assessment of the applicability of cold air and oil mist in surface grinding." *Journal of Materials Processing Technology* Vol. 140, No. 1-3 (2003): 224-230.
35. Nimomiya, S., Iwai, M., Uematsu, T., "Effect of the Floating Nozzle in Grinding of Mild Steels with Vitrified CBN Wheel." *Key Engineering Materials* Vol. 257 (2004): 315-320.
36. Quinn, W., "Experimental study of the near field and transition region of a free jet issuing from a sharp-edged elliptic orifice plate." *European Journal of Mechanics B/Fluids* Vol. 26 (2007): 583-614.
37. Quinn, W., "Influence of nozzle upstream shaping on turbulent jet flows from cruciform nozzles." *CANCAM: Eighth Canadian Congress of Applied Mechanics* Vol. 2 (1981): 585-586.
38. Quinn, W., "Turbulent mixing in a free jet issuing from a low aspect ratio contoured rectangular nozzle." *Aeronautical Journal* Vol. 99 (1995): 337-342.
39. Quinn, W., "Upstream nozzle shaping effects on near field flow in round turbulent free jets." *European Journal of Mechanics B/Fluids* Vol. 25 (2006): 279-301.
40. Quinn, W., Marsters, G., "Upstream influence on turbulent jet flows from cruciform nozzles." *Aeronautical Journal* Vol. 89 (1985): 55-58.
41. Quinn, W., Militzer, J., "Effects of nonparallel exit flow on round turbulent free jets." *International Journal of Heat and Fluid Flow* Vol. 10, No. 2 (1989): 139-145.
42. Ramesh, K., Huang, H., Yin, L., "Analytical and experimental investigation of coolant velocity in high speed grinding." *International Journal of Machine Tools & Manufacture* Vol. 44 (2004): 1070-1076.
43. Ramesh, K., Yeo S., Zhong, Z., Sim, K., "Coolant shoe development for high efficiency grinding." *Journal of Materials Processing Technology* Vol. 114 (2001): 240-245.
44. Rouse, H., Asle, M., Howe, J., Metzler, D., "Experimental Investigation of Fire Monitors and Nozzles." *117th ASCE Transactions* (1952).

45. Salmon, S., "Modern Grinding Process Technology." McGraw Hill Inc, New York (1992): 60-132.
46. Sedighi, M., Afshari, D., "Creep-feed grinding optimization by an integrated GA-NN system." *Journal of Intelligent Manufacturing* Vol. 21 (2010): 657-663.
47. Shaji, S., Radhakrishnan, V., "Investigations on the application of solid lubricants in grinding." *Journal of Engineering Manufacture* Vol. 216B (2001): 1325-1343.
48. Shen, C., Lin, B., Meng, F., "Structure optimization and application of conical convergence high-pressure jet nozzle." *Advanced Materials Research* Vol. 229 (2011): 1001-1006.
49. Skerlos, S., "Environmentally conscious disposal considerations in cutting fluid selection." *Proceedings of the ASME* Vol. 8 (1998): 397-403.
50. Steffen, J., *Application of a coherent jet coolant system in creep-feed grinding of Inconel 718*. M.A.S.c. Dissertation, Dalhousie University, 2004.
51. St-Pierre, B., Chatelain, J.F., Dufresne, L., "Development of a semi-empirical model based on CFD results for the prediction of coolant jet coherency for grinding application." *Transactions of the Canadian Society for Mechanical Engineering* Vol. 36, No. 2 (2012): 127-142.
52. Tawakoli, T., Hadad, M., Sadeghi, M., "Minimum quantity lubrication in grinding: effects of abrasive and coolant-lubricant types." *Journal of Cleaner Production* Vol. 19 (2011): 2088-2099.
53. Webster, J., "Coolant calculus: Directing cooling into the right place, at the right speed, in the right quantity." Cutting Tool Engineering Vol. 60, No. 2 (2008): 58-66.
54. Webster, J., "Improving surface integrity and economics of grinding by optimum coolant application, with consideration of abrasive tool and process regime." *Journal of Engineering Manufacture* Vol. 221 (2007): 1665-1675.
55. Webster, J., "Optimizing coolant application systems for high productivity grinding." *Abrasives Magazine*, October 1999, 34-41.
56. Webster, J., Cui, C., "Flow rate and jet velocity determination for design of a grinding cooling system." *Technical Papers Supplement of the 1st International*

Machining and Grinding Conference, Dearborne, Michigan, USA, Sept. 12-14., 1995.

57. Webster, J., Cui, C., Mindek, R., "Grinding fluid application system design." *CIRP Annals* Vol. 44 No. 1 (1995): 333-338.
58. Webster, J., Mindek, R., "Minimizing thermal damage of aerospace components using coolant nozzle and coolant system optimization." *Proceedings of the ASME Conference on Turbo Power* (1994): 97-104.
59. Wu, H., Lin, B., Cai, R., Morgan, M., "Measurement of the air boundary layer on the periphery of a rotating grinding wheel using LDA." *Journal of Physics: Conference Series* Vol. 76 (2007): 1-6.
60. Xu, H., Fu, Y. Sun, F., "Research on enhancing heat transfer in grinding contact zone with radial water jet impinging cooling." *Key Engineering Materials* Vol. 202-203 (2001): 53-56.
61. Yokogawa, M. Yokogawa, K., "Improving grinding performance of CBN wheels by dual-fluid cutting supply method." *International Journal of the Japan Society for Precision Engineering* Vol. 27 No. 1 (1992): 11-16.
62. Zeng, Y., New, T., Chng, T., "Flow behaviour of turbulent nozzle jets issuing from beveled collars." *Experimental Thermal and Fluid Science* Vol. 35 (2011): 15555-1564.